

# The PAU Survey: Measuring intrinsic galaxy alignments in deep wide fields as a function of colour, luminosity, stellar mass and redshift

D. Navarro-Gironés,<sup>1,2,3\*</sup> M. Crocce,<sup>1,2</sup> E. Gaztañaga,<sup>4,1,2</sup> A. Wittje,<sup>5</sup> M. Siudek,<sup>6,1</sup> H. Hoekstra,<sup>3</sup> H. Hildebrandt,<sup>5</sup> B. Joachimi,<sup>7</sup> R. Paviot,<sup>8</sup> C.M. Baugh,<sup>9,10</sup> J. Carretero,<sup>16,11</sup> R. Casas,<sup>1,2</sup> F. J. Castander,<sup>1,2</sup> M. Eriksen,<sup>12</sup> E. Fernandez,<sup>12</sup> P. Fosalba,<sup>1,2</sup> J. García-Bellido,<sup>13</sup> R. Miquel,<sup>12,14</sup> C. Padilla,<sup>12</sup> P. Renard,<sup>15</sup> E. Sánchez,<sup>16</sup> S. Serrano,<sup>17,1,2</sup> I. Sevilla-Noarbe,<sup>16</sup> P. Tallada-Crespi<sup>16,11</sup>

<sup>1</sup>Institute of Space Sciences (ICE, CSIC), Campus UAB, Carrer de Can Magrans, s/n, 08193 Barcelona, Spain

<sup>2</sup>Institut d'Estudis Espacials de Catalunya (IEEC), E-08860 Castelldefels (Barcelona), Spain

<sup>3</sup>Leiden Observatory, Leiden University, Einsteinweg 55, 2333 CC Leiden, the Netherlands

<sup>4</sup>Institute of Cosmology & Gravitation, University of Portsmouth, Dennis Sciama Building, Burnaby Road, Portsmouth PO1 3FX, UK

<sup>5</sup>Ruhr University Bochum, Faculty of Physics and Astronomy, Astronomical Institute (AIRUB), German Centre for Cosmological Lensing, 44780 Bochum, Germany

<sup>6</sup>Instituto de Astrofísica de Canarias (IAC), Departamento de Astrofísica, Universidad de La Laguna (ULL), 38200, La Laguna, Tenerife, Spain

<sup>7</sup>Department of Physics and Astronomy, University College London, Gower Street, London WC1E 6BT, UK

<sup>8</sup>Université Paris-Saclay, Université Paris Cité, CEA, CNRS, AIM, 91191, Gif-sur-Yvette, France

<sup>9</sup>Institute for Computational Cosmology, Department of Physics, Durham University, South Road, Durham DH1 3LE, UK.

<sup>10</sup>Institute for Data Science, Durham University, South Road, Durham DH1 3LE, UK

<sup>11</sup>Port d'Informació Científica (PIC), Campus UAB, C. Albareda s/n, 08193 Bellaterra (Barcelona), Spain.

<sup>12</sup>Institut de Física d'Altes Energies (IFAE), The Barcelona Institute of Science and Technology, Campus UAB, 08193 Bellaterra (Barcelona), Spain.

<sup>13</sup>Instituto de Física Teórica CSIC/UAM, Universidad Autónoma de Madrid, 28049 Madrid, Spain

<sup>14</sup>Institució Catalana de Recerca i Estudis Avançats (ICREA), 08010 Barcelona, Spain.

<sup>15</sup>Department of Astronomy, Tsinghua University, Beijing 100084, China

<sup>16</sup>Centro de Investigaciones Energéticas, Medioambientales y Tecnológicas (CIEMAT), Avenida Complutense 40, 28040 Madrid, Spain.

<sup>17</sup>Satlantis, University Science Park, Sede Bld 48940, Leioa-Bilbao, Spain

Accepted XXX. Received YYY; in original form ZZZ

## ABSTRACT

We present the measurements and constraints of intrinsic alignments (IA) in the Physics of the Accelerating Universe Survey (PAUS) deep wide fields, which include the W1 and W3 fields from the Canada-France-Hawaii Telescope Legacy Survey (CFHTLS) and the G09 field from the Kilo-Degree Survey (KiDS). Our analyses cover  $51\text{deg}^2$ , in the photometric redshift (photo- $z$ ) range  $0.1 < z_b < 1$  and a magnitude limit  $i_{\text{AB}} < 22$ . The precise photo- $z$ s and the luminosity coverage of PAUS enable robust IA measurements, which are key for setting informative priors for upcoming stage-IV surveys. For red galaxies, we detect an increase in IA amplitude with both luminosity and stellar mass, extending previous results towards fainter and less massive regimes. As a function of redshift, we observe strong IA signals at intermediate ( $z_b \sim 0.55$ ) and high ( $z_b \sim 0.75$ ) redshift bins. However, we find no significant trend of IA evolution with redshift after accounting for the varying luminosities across redshift bins, consistent with the literature. For blue galaxies, no significant IA signal is detected, with  $A_1 = 0.68^{+0.53}_{-0.51}$  when splitting only by galaxy colour, yielding some of the tightest constraints to date for the blue population and constraining a regime of very faint and low-mass galaxies.

**Key words:** cosmology: observations – large-scale structure of Universe – gravitational lensing: weak

## 1 INTRODUCTION

Weak gravitational lensing is a key cosmological probe that describes the small distortions that light experiences as it travels through the universe, due to its interaction with matter inhomogeneities in its path (Kilbinger 2015; Mandelbaum 2018). This phenomenon enables mapping the total mass distribution in the universe, comprising

both dark matter (DM) and luminous matter. However, a significant astrophysical systematic that affects the interpretation of weak gravitational lensing measurements are the intrinsic alignments (IA) of galaxies.

IA arises from the preferred orientation of galaxies due to local gravitational interactions with the surrounding large-scale structure (LSS). This phenomenon has gained relevance in the past decades (see Joachimi et al. 2015; Lamman et al. 2024 for an overview on this topic), as it not only provides valuable insights into the forma-

\* E-mail: david.navarro.girones@gmail.com

tion and evolution of galaxies (Conselice 2014), but also acts as a contaminant of weak gravitational lensing studies, by mimicking the lensing signal, usually with an opposite sign, thus reducing the overall amplitude of the observed gravitational lensing signal. In the era of precision cosmology and, especially, for stage-IV surveys, such as *Euclid* (Euclid Collaboration: Mellier et al. 2024), the Vera C. Rubin Observatory LSST (Ivezic et al. 2019) and the Nancy Grace Roman Space Telescope (Spergel et al. 2015), it is crucial to accurately model and measure IA, in order not to bias cosmological analyses.

The physical mechanisms that drive IA are thought to differ between galaxy types, motivating the commonly observed distinction between red and blue galaxies in IA studies. Red galaxies, which mainly correspond to elliptical, pressure-supported galaxies, are thought to be governed by the tidal alignment of their major axis with their host DM halo. In contrast, blue spiral galaxies, which correspond to rotationally-supported objects, are driven by their angular momentum, with the momentum axis aligned with that of the DM halo, generating quadratic alignments (Hirata & Seljak 2004). Related to this scheme, the Non-Linear Alignment (NLA) model (Bridle & King 2007), an extension of the Linear Alignment (LA) model (Catelan et al. 2001; Hirata & Seljak 2004) in which the linear matter spectrum is substituted by the non-linear one, enables the IA to be explained as a function of the tidal field, while the Tidal Alignment Tidal Torquing (TATT) model (Blazek et al. 2019) allows us to incorporate the tidal torquing effect into the equation. As a consequence, it is expected that the IA observed in elliptical galaxies can be better explained via the NLA model, while that in spiral galaxies follows more closely the TATT model. On smaller scales, a halo model (Schneider & Bridle 2010; Fortuna et al. 2021a) has been proposed, which is able to describe IA at scales comparable to those of DM halos. Finally, more complex models have been proposed, which include higher-order expansions of the tracers of IA (Vlah et al. 2020, 2021; Bakx et al. 2023; Maion et al. 2024). These models aim to describe IA more accurately in the weakly non-linear regime, at the expense of introducing additional parameters.

Observational studies of IA are also of extreme importance, since they allow us to quantify the signal for diverse galaxy samples. In particular, many studies have focused on the study of red and bright galaxy samples (Mandelbaum et al. 2006; Hirata et al. 2007; Okumura et al. 2009; Joachimi et al. 2011; Johnston et al. 2019, 2021a; Zhou et al. 2023; Hervás Peters et al. 2024; Georgiou et al. 2025), finding strong evidence of positive alignments. However, an open question is the IA of blue galaxies, where observations (Hirata et al. 2007; Mandelbaum et al. 2010; Johnston et al. 2019, 2021a; Georgiou et al. 2025) find IA amplitudes consistent with zero, while some simulations (e.g. Codis et al. 2015; Chisari et al. 2015; Samuroff et al. 2021) show some degree of alignment. For red galaxies, there is a consensus in the literature (Singh et al. 2015; Joachimi et al. 2011; Johnston et al. 2019; Fortuna et al. 2021b; Samuroff et al. 2023; Hervás Peters et al. 2024) for a dependence of IA on luminosity, which is usually described as a double power law, with more luminous galaxies exhibiting a stronger dependence than fainter ones. Recently, Fortuna et al. (2025) proposed that this double power law is the result of the double power law in the luminosity-to-halo mass relation. Finding that, in the range they explored, they can describe the dependence of IA on halo mass using a single power law, which would imply that the halo mass is the driving force of the IA amplitude, as already suggested in Piras et al. (2017). In terms of redshift evolution, no clear evolution has been found in the literature (Joachimi et al. 2011; Singh et al. 2015; Johnston et al. 2019; Fortuna et al. 2021b). However, the IA contribution appears stronger at low redshifts relative to the weak gravitational lensing signal, because the latter decreases

at low redshifts. While the majority of observations have focused on relatively bright samples, the IA impact for low-mass and low-luminosity objects, which constitute an important fraction of the cosmic galaxy population, remains underrepresented in IA studies, limiting our understanding of this effect.

Measurements of galaxy clustering (GC) and IA require precise knowledge of the distance to the objects being correlated and allow us to constrain the IA amplitude with the models described above. Even though spectroscopic redshifts (spec- $z$ s) allow us to obtain precise distances, obtaining them is expensive, since only a limited number of objects can be observed at once and the completeness of faint galaxy samples is lower than for photometric galaxy surveys. As an alternative to spec- $z$ s, photometric redshifts (photo- $z$ s) allow us to measure distances of objects with higher completeness, and of all objects with measured fluxes, at the expense of reducing the precision of the distance estimates. In that sense, the precision of the recovered distances strongly depends on the filters used, with most surveys relying on broad-band (BB) filters that reproduce the spectral energy distribution (SED) of galaxies at limited resolution and recover distance estimates with a  $\sim 5\%$  uncertainty at the mean redshift analysed in this work (e.g., Hildebrandt et al. 2012, 2021). The precision of photo- $z$ s can be further improved by increasing the number of bands and reducing their width, with so-called narrow-band (NB) surveys, such as the Physics of the Accelerating Universe Survey (PAUS; Benítez et al. 2009), ALHAMBRA (Moles et al. 2008), LAGER (Zheng et al. 2017) or mini-JPAS (Bonoli et al. 2021).

PAUS addresses the complexity of photo- $z$  estimation using 40 NBs, in combination with other BBs, which allow us to better reconstruct the SED of galaxies by improving the wavelength accuracy with which features, such as the 4000 Å break, can be recovered and to detect emission lines. This allows us to obtain an order of magnitude better photo- $z$ s than typical BB surveys for bright and low-redshift objects, where the fluxes of galaxies present high signal-to-noise ratios (SNRs) in the NBs (Navarro-Gironés et al. 2024). Additionally, the large number densities measured by PAUS enable the study of the weakly non-linear regime, covering the gap between limited areas and volumes provided by spectroscopic surveys and larger areas with lower redshift precision provided by photometric surveys. Hence, PAUS enables the study of highly dense intermediate areas, with state-of-the-art photo- $z$ s. Moreover, due to its precise redshift estimates, PAUS can focus on fainter objects than other stage-III surveys, such as the Dark Energy Survey (DES; Dark Energy Survey Collaboration et al. 2016), the Kilo-Degree Survey (KiDS; de Jong et al. 2013) and the Hyper Suprime-Cam (HSC; Aihara et al. 2018), which usually focus on the objects with better photo- $z$  estimates. This is of utmost importance for the upcoming stage-IV surveys, which will cover fainter magnitudes and will need a precise description of IAs in order not to bias their cosmological analyses.

Here, we focus on measuring and modelling the GC and the IA as a function of colour, luminosity, stellar mass and redshift using PAUS. For this purpose, we measure the 3-dimensional galaxy-galaxy and galaxy-shape correlation functions of close galaxies and project them along the line-of-sight (LOS). We model these measurements assuming a non-linear galaxy bias (Dekel & Lahav 1999) and the NLA models, for the GC and the IA, respectively. We provide IA amplitude fits for different galaxy samples, allowing us to extend our knowledge towards lower luminosities and masses.

This paper is structured as follows. In Section 2, we introduce the data used in this analysis. Next, in Section 3 and Section 4, we introduce the estimators we use to measure and model, respectively, the GC and IA correlation functions. Section 5 gives our results and

discussion. We end with our conclusions in Section 6. Throughout this paper, for consistency with previous work (Johnston et al. 2021a), we assume a flat  $\Lambda$ CDM cosmology, with  $\Omega_m = 0.25$ ,  $\Omega_b = 0.044$ ,  $h = 0.69$ ,  $n_s = 0.95$  and  $\sigma_8 = 0.8$ .

## 2 DATA

This section introduces PAUS and describes the photo-zs, the galaxy shapes and the colour separation employed for the measurement of galaxy IA in PAUS. It also includes a brief description of the MICE simulation, used in this work to validate some of our methods.

### 2.1 PAUS

PAUS is a photometric survey that was carried out at El Roque de Los Muchachos, in the Canary Islands. It used PAUCam (Padilla et al. 2019), a unique instrument that covers a  $\sim 1^\circ$  diameter field of view (FoV) and is equipped with a set of 40 NBs, ranging from  $4500\text{ \AA}$  to  $8500\text{ \AA}$ , in steps of  $100\text{ \AA}$ . PAUS complements its NB observations using BB data from the Canada-France-Hawaii Telescope Lensing Survey (CFHTLenS; Erben et al. 2013; Heymans et al. 2012; Hildebrandt et al. 2012) and KiDS (Kuijken et al. 2019). The principal targets PAUS has observed are the W1 and the W3 fields from the Canada-France-Hawaii Telescope Legacy Survey (CFHTLS; Cuillandre et al. 2012), the G09 field from KiDS and the COSMOS field (Scoville et al. 2007), with the latter mainly used for calibration and validation purposes. The total area covered by PAUS in these fields is  $\sim 51\text{ deg}^2$  (for objects with a minimum coverage of 30NB), with a number density of  $\sim 1.3 \times 10^4$  objects  $\text{deg}^{-2}$  down to  $i_{\text{AB}} < 22$ .

The PAU data management (PAUdm) team is responsible for the treatment of the data (Tonello et al. 2019). The data reduction involves NB image processing, where the photometric calibration and scattered-light correction are accounted for, and forced photometry is performed over a given reference catalogue to optimise the flux measurement. For a detailed description of both PAUS NB image photometry and photometric calibration, see Serrano et al. (2023) and Castander et al. (2024), respectively.

The large number of bands available in PAUS allows for the extraction of excellent photo-zs, with a precision that approaches that of spec-zs, as indicated in many PAUS works (Eriksen et al. 2019, 2020; Alarcon et al. 2021; Soo et al. 2021; Cabayol et al. 2023; Navarro-Gironés et al. 2024; Daza-Perilla et al. 2025). This, combined with its high number density of objects, makes PAUS a unique survey for many scientific studies, such as the analysis of galaxy properties using NBs (Tortorelli et al. 2021; Csizi et al. 2024), the determination of the mean mass of close galaxy pairs (Gonzalez et al. 2023), the study of the D4000 spectral break (Renard et al. 2022), the Ly- $\alpha$  intensity mapping (Renard et al. 2020) and a first study of the IA of galaxies (Johnston et al. 2021a), amongst others. In particular, PAUS covers a considerable fraction of the redshift and luminosity ranges of stage-IV surveys, allowing it to constrain IA for similar galaxy samples as those that will be used in their cosmological analyses.

### 2.2 Photo-z

Due to the large number of NBs used by PAUS, the resolution of the recovered SED is remarkable, with an average spectral resolution of  $R \sim 65$ . This allows us to estimate photo-zs with high precision compared to other BB photometric surveys, such as CFHTLenS or KiDS, with 5 and 9 BBs, respectively.

Here, we use the photo-z estimates presented in Navarro-Gironés

et al. (2024), who measured photo-zs for  $\sim 1.8$  million objects down to  $i_{\text{AB}} < 23$  in the W1, W3 and G09 fields. For a detailed description of the redshift estimation procedure, we refer the reader to that paper, but in the following lines we briefly summarise the important points for our IA analysis. The photo-zs are computed using a SED template-fitting algorithm named BCNz (Eriksen et al. 2019), which compares the observed fluxes in the PAUS NBs and BBs against SED templates. Then, it estimates a photo-z probability distribution for each object, where the mode of the distribution is taken as the point-like redshift estimate. Two different photo-z estimates are derived,  $z_{\text{b,BCNz}}$  and  $z_{\text{b,BCNzw}}$ , where the former is the direct result of BCNz and the latter is a weighted estimate between  $z_{\text{b,BCNz}}$  and  $z_{\text{b,BPZ}}$ , with  $z_{\text{b,BPZ}}$  the photo-zs derived by CFHTLenS (Hildebrandt et al. 2012) and KiDS (Hildebrandt et al. 2021) using BPZ (Benítez 2000), where only BB information is used.

The performance of  $z_{\text{b,BCNz}}$  decreases as the objects become fainter, due to the loss of SNR in the NBs. At  $i_{\text{AB}} > 22.5$ , the accuracies of  $z_{\text{b,BCNz}}$  and  $z_{\text{b,BPZ}}$  are similar, so the weighted estimate,  $z_{\text{b,BCNzw}}$ , benefits from the information gained by the different templates in both photo-z codes. Besides,  $z_{\text{b,BCNzw}}$  helps to break some degeneracies in the  $z_{\text{b}}$  vs.  $z_{\text{s}}$  scatter plot, as can be seen in Fig. 9 of Navarro-Gironés et al. (2024). As a consequence, in this work we use the weighted photo-z estimate,  $z_{\text{b,BCNzw}}$ . Additionally, in order to remove objects with low photo-z quality and potentially catastrophic outliers, we employ the  $Q_z$  parameter:

$$Q_z \equiv \frac{\chi_{\text{BCNz}}^2}{N_f - 3} \left( \frac{z_{\text{quant}}^{99} - z_{\text{quant}}^1}{\text{ODDS}} \right), \quad (1)$$

where  $\chi_{\text{BCNz}}^2$  is an estimate of the fit between the BCNz SED templates and the observed fluxes,  $N_f$  is the number of filters,  $z_{\text{quant}}^n$  is the  $n$ th percentile of the  $p(z)$  posterior distribution and ODDS is a parameter that measures the probability located around the peak of  $p(z)$ :

$$\text{ODDS} = \int_{z_{\text{b}} - \Delta z}^{z_{\text{b}} + \Delta z} dz p(z), \quad (2)$$

with  $\Delta z = 0.035$ . After analysing the  $Q_z$  distribution, which decreases exponentially with  $Q_z$ , we impose a cut at  $Q_z < 25$  to remove the 10% of objects with the highest values (and hence which are expected to have the poorest photometric redshifts).

Fig. 1 shows the photo-z accuracy in terms of  $\sigma_{68}(\Delta z)$ , outlier fraction and bias as a function of  $i_{\text{AB}}$  (triangles up) and  $z_{\text{b}}$  (triangles down), where  $\Delta z$  is defined as:

$$\Delta z = \frac{z_{\text{b}} - z_{\text{s}}}{1 + z_{\text{s}}}, \quad (3)$$

$\sigma_{68}(\Delta z) = (z_{\text{quant}}^{84.1} - z_{\text{quant}}^{15.9})/2$ , the outlier fraction is computed as the fraction of objects with  $|\Delta z| > 0.1$ <sup>1</sup> and the bias is determined by the median of  $(z_{\text{b}} - z_{\text{s}})$ .

The  $\sigma_{68}(\Delta z)$  ranges from  $\sim 0.003$  to  $\sim 0.04$  (0.03) as a function of  $i_{\text{AB}}$  ( $z_{\text{b}}$ ), with an increase towards faint and high-redshift objects. Similar behaviour is seen for the outlier fraction, although the faintest  $i_{\text{AB}}$  bins perform worse in this metric than their counterpart  $z_{\text{b}}$  bins. Finally, the bias is centred around 0 until  $i_{\text{AB}} \sim 21$  and  $z_{\text{b}} \sim 0.7$ , after which it begins to gradually deteriorate. The spec-zs that have been used for the validation of the photo-zs are the ones presented in Table 2 of Navarro-Gironés et al. (2024), which mainly correspond to the

<sup>1</sup> We use this value following Navarro-Gironés et al. 2024.

Sloan Digital Sky Survey (SDSS; [Ahumada et al. 2020](#)), the Galaxy And Mass Assembly (GAMA) survey ([Hopkins et al. 2013](#)), the VIMOS Public Extragalactic Redshift Survey (VIPERS; [Scoville et al. 2018](#)), DEEP2 ([Davis et al. 2003](#)) and KiDZ-COSMOS ([Wright et al. 2024](#)).

### 2.3 Galaxy shapes

Accurate galaxy shapes are crucial for any IA analysis. Here, we use the widely used Kaiser-Squires-Broadhurst (KSB) algorithm, described in [Kaiser et al. \(1995\)](#) and [Luppino & Kaiser \(1997\)](#), with corrections presented in [Hoekstra et al. \(1998\)](#), which returns an estimate of the shear. Noise in the data, as well as limitations of the approach, result in a multiplicative bias that can be quantified, and corrected for, using realistic image simulations, as discussed in [Hoekstra et al. \(2015\)](#). We refer the reader to those papers for a detailed description of this process. As a summary, below we describe the main aspects necessary to understand the shear calibration in our analysis.

The first step is to measure the central second moments of the galaxy images,  $I_{ij}$ , defined as:

$$I_{ij} = \frac{1}{I_0} \int d^2x x_i x_j W(x) f(x), \quad (4)$$

with  $I_0$  the weighted monopole moment,  $x_i$  the  $i$  coordinate of the galaxy image,  $f(x)$  the observed galaxy image and  $W(x)$  a weight function to reduce the sky noise. To choose the width of the weight function, we follow the same configuration used in [Johnston et al. \(2021a\)](#), that is, 1.75 times the observed half-light radius of the galaxy.

The shape can then be quantified by combining the weighted quadrupoles into the polarisation:

$$e_1 = \frac{I_{11} - I_{22}}{I_{11} + I_{22}} \quad \text{and} \quad e_2 = \frac{2I_{12}}{I_{11} + I_{22}}. \quad (5)$$

This is a biased estimator of the shear, because of the weight function, with an uncertainty  $\sigma_e$  that can be computed following [Hoekstra et al. \(2000\)](#). The shift in the polarisation,  $\delta e_\alpha$ , due to the shear,  $\gamma_\beta$ , is quantified by the shear polarisability,  $P_{\alpha\beta}^{\text{sh}}$ , defined so that:

$$\delta e_\alpha = P_{\alpha\beta}^{\text{sh}} \gamma_\beta, \quad (6)$$

where we have used the sum convention. Formally,  $P_{\alpha\beta}^{\text{sh}}$  is a tensor, but in practice the ensemble average is diagonal, with both elements having the same value, because of symmetry. [Kaiser et al. \(1995\)](#) showed how the shear polarisability can be determined from higher-order moments.

Accounting for the shear polarisability is, however, not sufficient, because the observed shapes are biased by noise in the data, and the blurring by the point spread function (PSF). If the PSF is anisotropic, it introduces correlations between the observed polarisations, potentially mimicking a lensing or IA signal. This needs to be corrected before applying the shear polarisability in eq. 6. As shown in [Kaiser et al. \(1995\)](#), the change in polarisation due to an anisotropic PSF can be expressed as:

$$\delta e_\alpha = P_{\alpha\beta}^{\text{sm}} p_\beta, \quad (7)$$

where  $P_{\alpha\beta}^{\text{sm}}$  is the smear polarisability, which captures the response of an object due to the convolution with an anisotropic PSF, and  $p_\beta$  is a measure of the PSF anisotropy. The latter can be measured by

using the observed polarisations and smear polarisabilities of stars:

$$p_\alpha = \frac{e_\alpha^*}{P_{\alpha\alpha}^{\text{sm}}}, \quad (8)$$

where the measurements of the stars use the same weight function as was used for a particular galaxy ([Hoekstra et al. 1998](#)).

Finally, to correct for the circularisation of the galaxy images due to their convolution with the PSF, the pre-seeing shear polarisability is computed following [Luppino & Kaiser \(1997\)](#):

$$P^\gamma = P^{\text{sh}} - \frac{P_{*}^{\text{sh}}}{P_{*}^{\text{sm}}} P^{\text{sm}}. \quad (9)$$

Even though  $P^\gamma$  is a 2x2 tensor, we assume it is diagonal, with both elements having the same value, because of symmetry. Moreover, individual estimates for  $P^\gamma$  are noisy, and small values increase the variance of the shear measurements. Therefore, we only select objects with  $P^\gamma > 0.1$ , and account for these selections in the image simulations.

Combining eq. 6, 7 and 9, we obtain the shear estimate:

$$\hat{e}_i = \frac{e_i - P_{ii}^{\text{sm}} p_i}{P^\gamma}. \quad (10)$$

We use the symbol  $\hat{e}$  here because we correlate ellipticities for IA studies. This is because the ellipticity, defined as  $(1 - q)/(1 + q)$ , with  $q$  the axis ratio, is an unbiased estimate of the shear, and thus can be compared directly to lensing signals.

Although eq. 10 provides good estimates, especially for large, bright galaxies, an incomplete correction for the PSF contamination might lead to residual multiplicative ( $\mu_i$ ) and additive biases ( $c_i$ ). Moreover, shape estimates involve ratios of noisy quantities, resulting in bias. These biases can be captured as ([Heymans et al. 2006](#); [Hoekstra et al. 2015](#)):

$$e_i = (1 + \mu_i) \hat{e}_i + c_i, \quad (11)$$

where we explicitly indicate that we aim to obtain unbiased ellipticity estimates.

In this paper, to study the IA signal, we correlate positions and shapes. As a consequence, residual additive bias has a minimal impact, because it tends to vanish in the ensemble average over many pairs of galaxies by symmetry. Therefore, following [Johnston et al. \(2021a\)](#), we assume that the correction from KSB is sufficient. As for the multiplicative bias, we follow the simulation setup described in [Hoekstra et al. \(2015\)](#) and used in [Johnston et al. \(2021a\)](#), and determine  $\mu = (\mu_1 + \mu_2)/2$  from simulated images. In particular, we capture how the bias depends on the size of the galaxy and its SNR. We refer interested readers to these papers for further details. We compute the mean multiplicative bias for each field and sample selection we study in Section 5, which include splits in red and blue galaxies, in luminosity, stellar mass and redshift.

It is important to note that we aim to perform IA measurements with a cut in  $i_{\text{AB}}$  magnitude. This poses the challenge that the CFHTLenS and the KiDS surveys use different bands to measure galaxy shapes, the  $i_{\text{AB}}$  band being the one employed by CFHTLenS and the  $r_{\text{AB}}$  that employed by KiDS. This leads to different completenesses in the galaxy shape estimation as a function of the limiting magnitude  $i_{\text{AB}}$  for both surveys. In the case of CFHTLenS, galaxy shape measurements down to  $i_{\text{AB}} = 22.5$  are available and complete. Nevertheless, for the KiDS sample, galaxy shape measurements with good quality are only complete down to  $i_{\text{AB}} = 22$ . For this reason, we perform measurements of IA for two scenarios. The baseline scenario is the measurement of the combined CFHTLenS (W1 and W3) and KiDS (G09) fields down to  $i_{\text{AB}} = 22$ . The second scenario

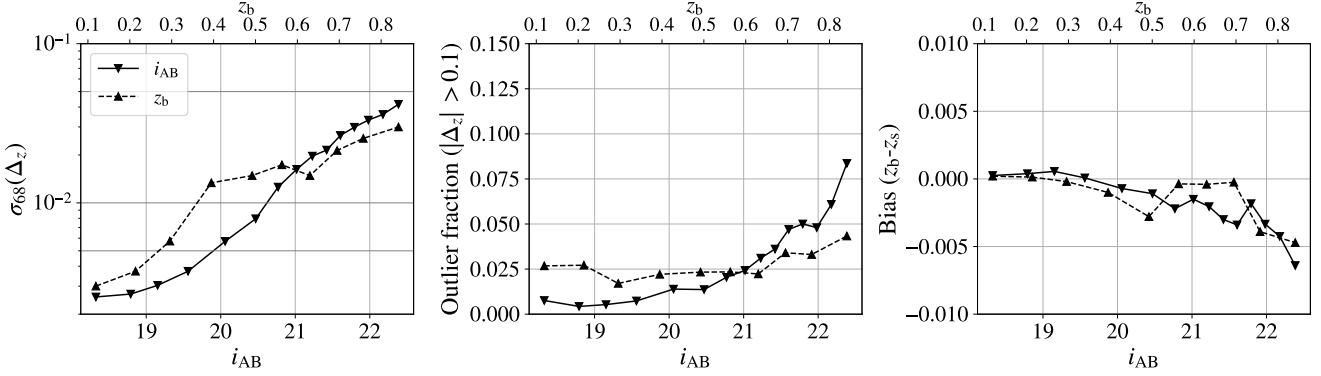


**Figure 1.**  $\sigma_{68}(\Delta_z)$  (left), outlier fraction (centre) and bias (right) as a function of  $i_{AB}$  (triangles down, bottom axis) and  $z_b$  (triangles up, top axis) for the photo-zs used in this analysis.

extends the measurements to deeper magnitudes ( $i_{AB} = 22.5$ ) but only using the CFHTLenS fields, and is presented in Appendix A.

## 2.4 Restframe magnitudes and colours

A common approach taken in the measurements of IA is to separate samples into red and blue galaxies. The reason for this is that galaxy colour and morphology tend to be closely related, with red galaxies mainly corresponding to ellipticals and passive types and blue galaxies to spirals and star-forming (active) galaxies (Strateva et al. 2001; Park & Choi 2005; Siudek et al. 2022).

This separation is performed using the PAUS physical properties derived by Siudek et al. (in prep.) and used in Navarro-Gironés et al. (2024), which were estimated by performing SED fitting with the Code Investigating GALaxy Emission (CIGALE; Boquien et al. 2019). This code takes into account the dust absorption affecting stellar emission in the UV and optical bands and its re-emission in the IR. As stated in Navarro-Gironés et al. (2024), CIGALE does not perform well for PAUS objects with low SNR in the NBs. This particularly impacts the estimation of the physical properties we use to separate between active and passive galaxies in this work. As a consequence, we use the physical properties estimated with BB-only fits, as they perform better in the separation. We also remove objects with a reduced  $\chi^2_{\nu, \text{CIGALE}} > 5$  (Masoura et al. 2018; Buat et al. 2021), which affects  $\sim 0.5\%$  of the objects, where  $\chi^2_{\nu, \text{CIGALE}}$  is related to the quality of the CIGALE fit.

We split our samples between active and passive populations using a  $\text{NUV}-r$  vs.  $r-K$  ( $\text{NUV}rK$  from now on) diagram, following Arnouts et al. (2013). There, the redshift range tested was  $0.2 \leq z \leq 1.3$ , which closely matches the redshift range we consider in this analysis, which is  $0.1 \leq z \leq 1$ . On the one hand, the  $\text{NUV}-r$  colour traces the specific star formation rate (sSFR), given the capability of the NUV and the  $r$  bands to track young and old populations, respectively (Salim et al. 2005). On the other hand, the  $r-K$  colour accounts for dust attenuation in active galaxies and helps to break degeneracies related to this effect in the  $\text{NUV}-r$  cut (Arnouts et al. 2013). The separation of active and passive galaxies following a  $\text{NUV}rK$  diagram is similar to the one performed in Williams et al. (2009) following a  $(U-V)$  vs.  $(V-J)$  diagram, which was also employed in the separation between active and passive galaxies in Navarro-Gironés et al. (2024) in order to study the performance of photo-zs as a function of colour. In this case, we opt for the  $\text{NUV}rK$  diagram, since it allows to expand the covered wavelength range analysed in the

separation. We note that the terms ‘‘active/blue’’ and ‘‘passive/red’’ are used interchangeably throughout the rest of this paper.

Following Davidzon et al. (2016), we use 2 cuts in the colour-colour space to separate between active and passive galaxies. In their case, they divide the  $\text{NUV}rK$  space in 3 regions: active (galaxies fulfilling eq. 12), green-valley (galaxies fulfilling eq. 13 but not eq. 12) and passive (the rest of the diagram):

$$\text{NUV}-r > 3.75 \quad \& \quad \text{NUV}-r > 1.37(r-K) + 3.2 \quad \& \quad r-K < 1.3, \quad (12)$$

$$\text{NUV}-r > 3.15 \quad \& \quad \text{NUV}-r > 1.37(r-K) + 2.6 \quad \& \quad r-K < 1.3. \quad (13)$$

However, in our case, we cannot aim to reach this level of precision when separating active and passive galaxies, since the absolute magnitudes computed by CIGALE are affected by the redshift uncertainty from the photo-zs, while Davidzon et al. (2016) use spec-zs. Nevertheless, given that the region located in the space defined by eq. 12 and 13 corresponds to galaxies which are reducing their sSFR, and may be in the transition between active and passive galaxies, we assign objects as active or passive so as to obtain a similar percentage of red and blue galaxies in all PAUS fields. In particular, we assign the W1 and W3 objects that lie in this intermediate colour-colour space as passive and the ones from G09 as active. This way, we find that the percentage of passive galaxies is 18.1% (16.0%), 23.8% (20.5%) and 19.5% (17.2%) for the W1, G09 and W3 fields, respectively, at  $i_{AB} = 22.0$  ( $i_{AB} = 22.5$ ). We note that the percentages of red/blue galaxies are still different between fields, specially for the CFHTLenS and KiDS samples, likely due to the different photometric systems.

To secure the separation between active and passive galaxies, we also use the  $T_{\text{BPZ}}$  parameter employed in CFHTLenS and KiDS. This parameter allows us to separate objects by their spectral type, and is obtained by performing SED fitting using the BPZ photo- $z$  algorithm. With this new parameter, we define red objects as those with  $T_{\text{BPZ}} \leq 1.5$  (Smit & Kuijken 2018) and blue for the rest. For red galaxies, the difference in the number of objects after applying  $T_{\text{BPZ}}$  does not change much. The agreement in the objects classified as red by both the  $\text{NUV}rK$  diagram and the  $T_{\text{BPZ}}$  parameter is 99.98%, 93.57% (94.63% at  $i_{AB} = 22.5$ ) and 99.98% of galaxies, for the W1, G09 and W3 fields, respectively. However, the case for blue galaxies

is different, with  $\sim 87\%$  ( $\sim 89\%$  at  $i_{\text{AB}} = 22.5$ ) of objects classified as blue by the NUV $rK$  cut and the  $T_{\text{BPZ}}$  criteria for all the fields.

Fig. 2 shows the NUV $rK$  diagram used to separate between red and blue galaxies for the W1, G09 and W3 fields (from left to right). As stated before, the position of the diagonal lines differ between fields, with eq. 12 delimiting the region for active galaxies in the W1 and W3 fields and eq. 13 delimiting it for the G09 field. It can be noted that there is a lack of objects just below the diagonal lines, which is produced by the additional cut performed in  $T_{\text{BPZ}}$ . Confirming our sample selection, we find that active galaxies have a larger sSFR (as computed by CIGALE) than passive ones, as indicated by the colour bar on these diagrams. The percentage of red objects after applying both the NUV $rK$  and the  $T_{\text{BPZ}}$  cuts is 20.6% (18.3%), 26.2% (25.0%) and 22.2% (19.7%) for the W1, G09 and W3 fields, respectively, at  $i_{\text{AB}} = 22.0$  ( $i_{\text{AB}} = 22.5$ ). In Appendix B, we show a comparison of the red and blue classification when employing alternative colour-magnitude cuts from the literature.

Fig. 3 shows the  $i_{\text{AB}}$  distribution for the dense sample (left), which refers to the full galaxy sample used to define the galaxy positions in the estimators of Section 3, the red galaxies with shapes (middle) and the blue galaxies with shapes (right) for the three wide fields under study. The observed magnitude distribution is very similar for each of the fields, for both the dense and the shape samples separated by colour. This is an indication that we are selecting similar galaxy populations throughout, which is an important aspect to take into account when combining the measurements of GC and IA from different fields, as we do in our results in Section 5. In this case, we show the shape samples down to  $i_{\text{AB}} = 22$  for conciseness. Nevertheless, the fainter shape samples of the CFHTLenS fields also have very similar  $i_{\text{AB}}$  distributions.

## 2.5 MICE

The Marenostrum Institut de Ciències de l’Espai Grand-Challenge (MICE-GC; Fosalba et al. 2015; Crocce et al. 2015; Fosalba et al. 2014; Carretero et al. 2014; Hoffmann et al. 2014) is an N-body simulation run using the public code GADGET-2 (Springel 2005). It contains  $4096^3$  DM particles in a comoving volume of  $(3 \text{ } h^{-1} \text{ Gpc})^3$  and assumes a flat  $\Lambda$ CDM cosmology with  $\Omega_m = 0.25$ ,  $\Omega_\Lambda = 0.75$ ,  $\Omega_b = 0.044$ ,  $n_s = 0.95$ ,  $\sigma_8 = 0.8$  and  $h = 0.7$ .

Galaxies are introduced by combining the halo occupation distribution (HOD; Jing et al. 1998; Seljak 2000; Scoccimarro et al. 2001) and subhalo abundance matching (SHAM) techniques (Vale & Ostriker 2004; Conroy et al. 2006; Trujillo-Gomez et al. 2011). The galaxy mock is calibrated to reproduce SDSS (York et al. 2000) colour distributions, luminosity function and GC.

IA are introduced in MICE-GC by assigning intrinsic shapes and orientations to the MICE simulation up to redshift  $z = 1.4$  (Hoffmann et al. 2022). This is done using a semi-analytic IA model, where the intrinsic shapes and orientations are assigned based on the galaxy colour and the galaxy type (central or satellite). In this model, red central galaxies have their 3-dimensional principal axes aligned with their host halo, while blue central galaxies have their minor axis aligned with the angular momentum of the host halo and their major axis randomly oriented in the perpendicular plane of the minor axis. In the case of satellite galaxies, their major axes are oriented towards the host halo and their minor axes are randomly oriented in the perpendicular plane of the major axis. These alignment configurations assume that red central galaxies are pressure-supported objects affected by the same tidal field as their host halo, while blue central galaxies are rotationally supported and do not present IA. Finally, both red and blue satellite galaxies are preferentially oriented towards

the centre of their host halo. The colour separation between red and blue galaxies in MICE is defined with a  $u - r = M_u - M_r > 0.94$  cut, where  $M_u$  and  $M_r$  correspond to the absolute rest-frame magnitudes in the CFHT- $u$  and Subaru- $r$  bands, respectively. The parameters of the semi-analytic IA model are calibrated against the COSMOS (Laigle et al. 2016; Griffith et al. 2012) and BOSS LOWZ (Singh & Mandelbaum 2016) surveys.

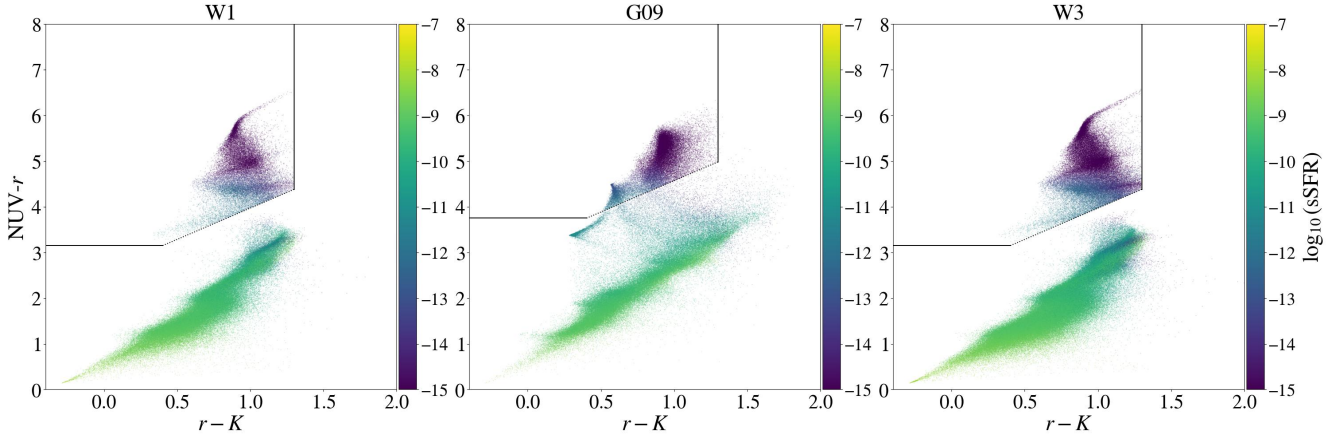
This galaxy mock is used to validate and perform some consistency checks. In particular, in Appendix C, we describe the generation of the random catalogues (see Section 3) necessary to perform the measurements and accurately obtain galaxy biases. Next, given that we analyse the data with photo- $z$ s, we show in Appendix D that we are able to obtain consistent galaxy biases and IA parameters when using photo- $z$ s or spec- $z$ s. Finally, in Appendix E, we study the errors (see Section 3) associated with the measurements and compare them with the ensemble covariance of MICE.

Our first goal is to construct a subsample of the MICE-GC, so that it resembles the PAUS wide fields. First, we cut the galaxy mock such that  $19 < i_{\text{AB}} < 22.5$  using the MICE synthetic observed magnitude in the COSMOS CFHT- $i$  band, which is the one that most closely resembles the CFHTLenS and KiDS  $i_{\text{AB}}$  magnitudes. We adopt the cut of the fainter samples ( $i_{\text{AB}} = 22.5$ ), instead of the brighter samples cut at  $i_{\text{AB}} = 22$ , since the validations we want to perform are dependent on the photo- $z$  quality, which worsens with fainter magnitudes. Thus, if we are able to validate our method for fainter magnitudes, the brighter case is also expected to work. Later, we introduce noise in the spec- $z$ s available in the MICE catalogue to generate PAUS-like photo- $z$ s in the simulation. For that, we use the galaxy mock designed by Wittje et al. (in prep.), which is created using the Flagship simulation (Euclid Collaboration: Castander et al. 2024). This galaxy mock generates objects with PAUS-like fluxes and computes the photo- $z$  using BCNz and BPZ. We combine both of these redshift estimates to obtain the weighted photo- $z$  presented in Navarro-Gironés et al. (2024) and inject them into the MICE simulation. To do so, we bin the galaxy mock presented in Wittje et al. (in prep.) into spec- $z$  bins of width  $\Delta z_s = 0.01$ . Then, for each bin of spec- $z$ s, we have a distribution of photo- $z$ s, which we use to sample and assign photo- $z$ s to the corresponding spec- $z$  bins in the MICE simulation.

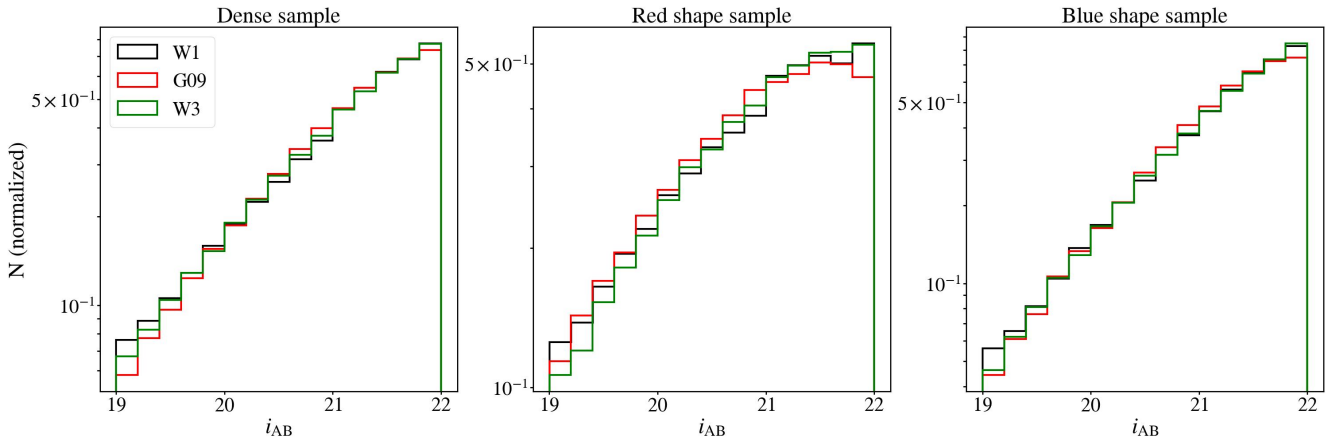
The upper panels of Fig. 4 show the distribution of photo- $z$  versus spec- $z$  for the MICE simulation (left) and for the PAUS objects in the W3 field that have spec- $z$ s (right). The resemblance of both distributions and, in particular, the spread along the diagonal line at large redshifts indicate the similarity between both photo- $z$  cases. This is further seen in the lower panels of Fig. 4, where we find comparable values between MICE and PAUS in terms of  $\sigma_{68}$  versus spec- $z$ .

Fig. 5 shows the comparison of the  $i_{\text{AB}}$  and  $z_b$  distributions between PAUS and the MICE mock, which shows that the redshift and magnitude distributions are very similar, indicating that the populations selected for PAUS and MICE agree and that the mock is suitable for performing validation and consistency checks.

In particular, when analysing the data, we perform measurements by combining the 3 PAUS wide fields. Thus, to have statistically significant results and ensure a realistic representation, we divide the full octant of MICE into 180 patches, such that we create 60 combinations of 3 patches with the same area as W1, G09 and W3. In this way, we can obtain 60 realisations in MICE of the GC and IA measurements, which we compare to the PAUS measurements.



**Figure 2.** Division in active and passive galaxies following a NUV $r$  $K$  diagram cut and a  $T_{\text{BPZ}}$  selection, coloured by the sSFR obtained with CIGALE, as indicated by the colour bar to the right of each panel. The top regions delimited by the black lines correspond to passive galaxies, while the complementary regions correspond to active galaxies.



**Figure 3.**  $i_{\text{AB}}$  distribution of the dense sample (left), the red galaxies with shapes (middle) and the blue galaxies with shapes (right) for each of the PAUS wide fields.

### 3 ESTIMATORS

We compute the 3-dimensional position-position correlation function using the Landy-Szalay estimator (Landy & Szalay 1993), binning in transverse and LOS separations,  $r_p$  and  $\Pi$ , respectively:

$$\xi_{\text{gg}}(r_p, \Pi) = \frac{DD - 2DR + RR}{RR}, \quad (14)$$

where  $D$  traces the galaxy positions of the dense samples and  $R$  corresponds to random samples that follow the angular and radial distributions of the dense samples. The random catalogues are set to be 50 times larger than the dense sample, in order to reduce shot noise. Even though we perform our IA analysis by separating the shape sample in red and blue galaxies, we measure the position-position correlation function without a division by colour, since we have checked that this reduces the errors in the IA measurements, given that the number of objects being correlated is larger.

The 3-dimensional galaxy position-intrinsic shear correlation function is a generalisation of the Landy-Szalay estimator for GC (Mandelbaum et al. 2006) and is defined as:

$$\xi_{\text{gp}}(r, \Pi) = \frac{S_+D - S_+R_D}{R_SR_D}, \quad (15)$$

with

$$S_+D = \sum_{i \neq j | r_p, \Pi} \varepsilon_+(j|i). \quad (16)$$

$S_+$  corresponds to the shape sample,  $D$  is the dense sample and  $R_S$  and  $R_D$  are the random catalogues that trace the shape and dense sample distributions, respectively. Here,  $\varepsilon_+ = \text{Re}(\varepsilon e^{2i\varphi})$ , where  $\varepsilon = \varepsilon_1 + i\varepsilon_2$  and  $\varphi$  is the polar angle connecting the pair of galaxies being correlated. As in the case of the position-position correlation function (eq. 14), only the shape sample is separated by galaxy colour. The expression in eq. 16 is the sum of the ellipticity components of galaxies  $i$  with respect to the galaxies in the dense sample  $j$ . Note that we do not normalise eq. 16 by the shear responsivity,  $\mathcal{R} \sim 1 - \sigma_{\varepsilon}^2$ , with  $\sigma_{\varepsilon}$  the shapes' sample dispersion. The reason for this is that the estimate we obtain in eq. 11 is an ellipticity, rather than a polarisation, and so it already accounts for the effect of the shear.

As indicated in Hoekstra et al. (2015), for each galaxy we weight the ellipticities in eq. 16 with  $w_i$ , defined as:

$$w_i = \frac{1}{\langle 0.25 \rangle^2 + \left( \frac{\sigma_{\varepsilon,i}}{P_i^{\gamma}} \right)^2}, \quad (17)$$

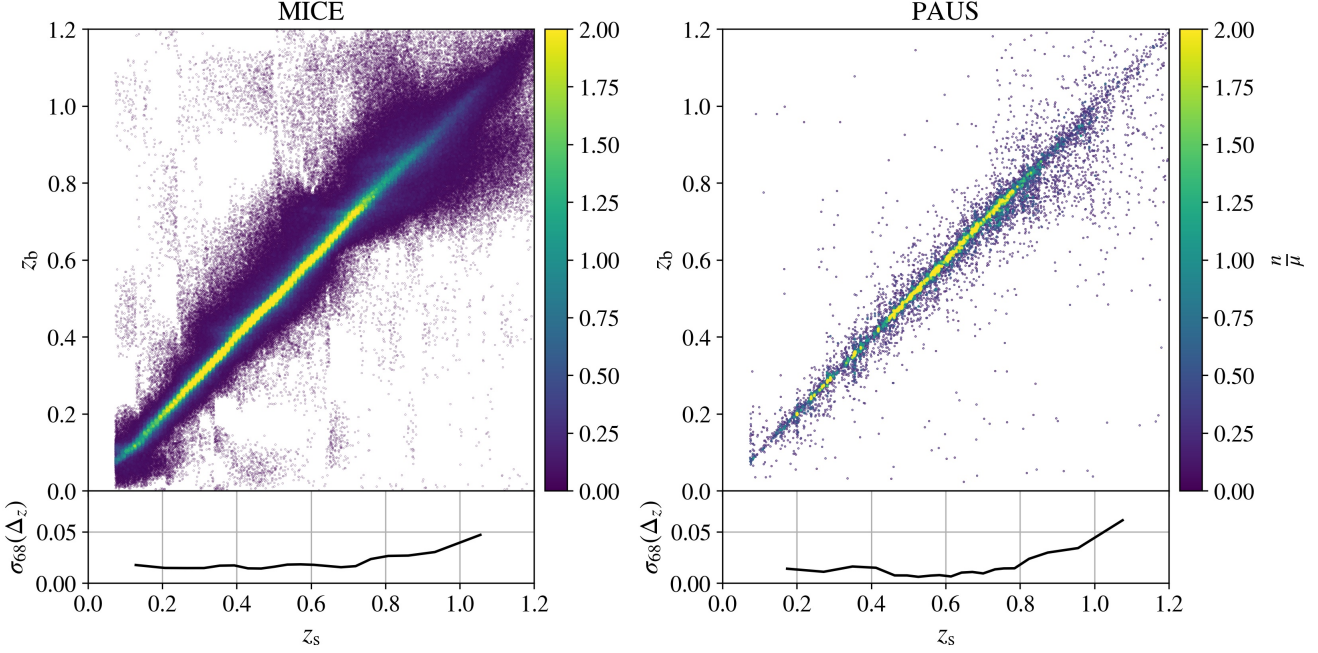


**Figure 4.** Top: Photo- $z$  vs. spec- $z$  of the galaxy mock catalogue from the MICE simulation (left) and of the objects from the PAUS W3 field that have spec- $z$ s (right), coloured by the number of objects in each pixel normalised by the median value. Bottom:  $\sigma_{68}(\Delta z)$  vs. spec- $z$  for the MICE simulation (left) and PAUS (right).

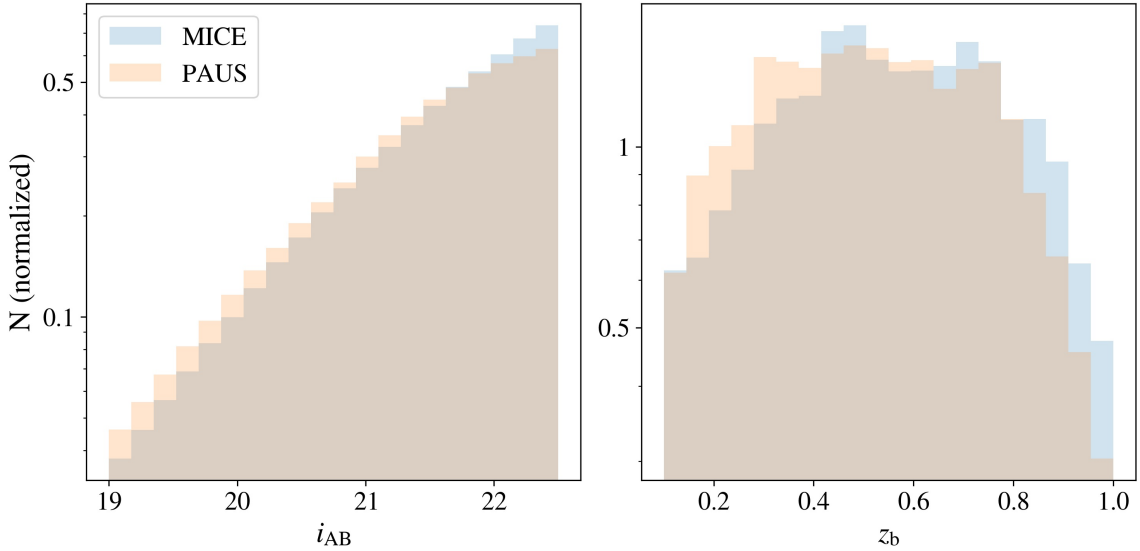


**Figure 5.** Comparison of the distribution of  $i_{AB}$  (left) and  $z_b$  (right) for the PAUS wide fields and the MICE galaxy mock, indicating the similarity of the galaxy populations for both cases. This enables the use of MICE in order to perform some consistency tests, detailed in Appendix C, D and E.

where 0.25 is the value we adopt for the intrinsic variance of the galaxy ellipticity (Hoekstra et al. 2000),  $\sigma_e$  is the uncertainty in the measurement of the polarisation (eq. 5),  $P^\gamma$  is the preseeing shear polarisability (eq. 9) and the subscript  $i$  refers to each galaxy in the shape sample.

An analogous estimator of eq. 15,  $\xi_{gx}$ , is defined by rotating the polarisations by 45°, with  $\varepsilon_x = \text{Im}(\varepsilon e^{2i\varphi})$ . A value different from 0 would imply a preferred direction of curl in the shape sample distribution. Thus, this quantity is usually used to check for systematics.

The 3-dimensional correlation functions defined in eq. 14 and eq. 15 are projected along the LOS, following:

$$w_{ab}(r_p) = \int_{-\Pi_{\max}}^{\Pi_{\max}} \xi_{ab}(r_p, \Pi) d\Pi, \quad (18)$$

where  $\Pi_{\max}$  is the maximum LOS separation and “ab” corresponds to either gg, gp or gx.

The correlation functions are measured using TreeCorr (Jarvis et al. 2004). We define 12 logarithmically-spaced bins in projected

separation ranging from 0.1-18  $h^{-1}$ Mpc, considering the size of the fields under study, and employ the radial binning devised by Johnston et al. (2021a), who defined eq. 19 to have positive and negative values:

$$|\Pi| = 0, 1, 2, 3, 5, 8, 13, 21, 34, 55, 89, 144, 233 h^{-1}\text{Mpc}, \quad (19)$$

such that  $\Pi_{\text{max}} = 233 h^{-1}\text{Mpc}$ . This expression accounts for the spread of galaxies in the radial direction caused by photo- $z$ , by enlarging the radial binning as the distance from the correlated object increases. This choice is justified further in Appendix D. The bin “slop” parameter from TreeCorr is set to 0 in our analysis.

The errors associated with our measurements are computed using the jackknife (JK) method (Norberg et al. 2009):

$$\text{Cov}_{\text{JK}} = \frac{N_{\text{JK}} - 1}{N_{\text{JK}}} \sum_{i=1}^{N_{\text{JK}}} (w_{\text{ab},i} - \bar{w}_{\text{ab}})(w_{\text{ab},i} - \bar{w}_{\text{ab}})^T, \quad (20)$$

where  $N_{\text{JK}}$  corresponds to the number of JK regions,  $w_{\text{ab},i}$  is the “ab” correlation function after removing the signal of the  $i$ -th JK region and  $\bar{w}_{\text{ab}}$  is the mean of all the JK regions.

We define  $N_{\text{JK}}$  so that each of our fields is divided into roughly equal area patches, corresponding to 4 angular regions in W1, 6 in G09 and 8 in W3. This number of angular JK regions was defined following Johnston et al. (2021a) for the W3 field, and adjusted to the W1 and G09 fields based on their area. Additionally, we also define regions by dividing the redshift range. This division in redshift depends on the case under study, since these have different redshift ranges. Table 2 includes the  $N_{\text{JK}}$  defined in each of our studies.

## 4 MODELLING

Here, we describe the modelling of the joint data vector  $w_{\text{gg}} \cup w_{\text{gp}}$  and the methodology we follow to constrain the galaxy bias and the IA parameters for the PAUS data. Sections 4.1 and 4.2 describe the galaxy power spectrum and the IA power spectrum that enter in our models, respectively. Next, we describe how we compute the projected spectroscopic and photometric correlation functions in Sections 4.3 and 4.4, respectively. Section 4.5 describes the contaminants introduced due to magnification and galaxy-galaxy lensing. Lastly, in Section 4.6 we discuss the likelihood analysis performed to constrain the galaxy bias and the IA parameters, including a description of the scale cuts and the priors.

To compute the various power spectra, we use PyCCL (Chisari et al. 2019) and FAST-PT (McEwen et al. 2016; Fang et al. 2017). The linear matter power spectrum is computed using CAMB (Lewis et al. 2000) and the non-linear matter power spectrum is computed with Halofit (Takahashi et al. 2012), both implemented in PyCCL.

### 4.1 Galaxy power spectrum

The relation between the matter and the galaxy distributions is encoded in the galaxy bias term(s). The simplest model one can use is given by a constant term (Kaiser 1984):

$$\delta_g = b_1 \delta_m, \quad (21)$$

where  $b_1$  is usually referred to as the linear galaxy bias. Although this model is very simplistic, it is known to work well on large scales (e.g. Euclid Collaboration: Castander et al. 2024). Nevertheless, at small scales, the non-linearities of the LSS need more sophisticated models.

Here, we express the galaxy overdensity field by expanding the density ( $\delta_m$ ) and the tidal ( $s_{ij}$ ) fields as (McDonald 2006; Baldauf et al. 2010; Saito et al. 2014):

$$\delta_g = b_1 \delta_m + \frac{1}{2} b_2 (\delta_m^2 - \langle \delta_m^2 \rangle) + \frac{1}{2} b_{s^2} (s^2 - \langle s^2 \rangle) + b_{3\text{nl}} \psi, \quad (22)$$

where  $s^2 = s_{ij} s^{ij}$  (assuming Einstein summation convention),  $\psi$  corresponds to the sum of third-order non-local terms with the same scaling (Saito et al. 2014),  $b_1$  is the linear galaxy bias (eq. 21),  $b_2$  the local quadratic bias,  $b_{s^2}$  the tidal quadratic bias and  $b_{3\text{nl}}$  the third-order non-local bias. One can express the galaxy-galaxy power spectrum from eq. 22 as (Krause et al. 2021):

$$\begin{aligned} P_{\text{gg}}(k) = & b_1^2 P_{\delta\delta}(k) + b_1 b_2 P_{b_1 b_2}(k) \\ & + b_1 b_{s^2} P_{b_1 s^2}(k) + b_1 b_{3\text{nl}} P_{b_1 b_{3\text{nl}}}(k) \\ & + \frac{1}{4} b_2^2 P_{b_2 b_2}(k) + \frac{1}{2} b_2 b_{s^2} P_{b_2 s^2}(k) + \frac{1}{4} b_{s^2}^2 P_{s^2 s^2}(k), \end{aligned} \quad (23)$$

where  $P_{\delta\delta}$  is the non-linear matter power spectrum and the power spectrum kernels ( $P_{b_1} P_{b_2}$ ,  $P_{b_1 s^2}$ , etc.), are defined in Saito et al. (2014). We also use the following co-evolution relations  $b_{s^2} = -4/7(b_1 - 1)$  and  $b_{3\text{nl}} = b_1 - 1$  (Saito et al. 2014; Pandey et al. 2020) to reduce the parameter space and alleviate model complexity.

The galaxy power spectrum that enters the modelling of  $w_{\text{gg}}$  is the one expressed in eq. 23. However, for the case of  $w_{\text{gp}}$ , the IA model we use assumes linear galaxy bias. Thus, the galaxy-intrinsic power spectrum that enters in  $w_{\text{gp}}$  is given by:

$$P_{\text{gI}}(k, z) = b_1 P_{\delta\text{I}}(k, z), \quad (24)$$

where  $P_{\delta\text{I}}$  is defined in Section 4.2. Nevertheless, we do not expect this to have much effect on the constraints of the galaxy bias parameters, since they are mainly constrained by  $w_{\text{gg}}$ , due to its higher SNR.

### 4.2 IA power spectrum

We model the IA following the NLA model, which is an extension of the LA model, with the linear matter power spectrum replaced by the non-linear matter power spectrum. The LA model works under the assumption that the host DM halo is tidally distorted by the gravitational field exerted by the surrounding LSS. The stellar content of the galaxy follows this distortion at the time of its formation and/or during its evolution, being tidally aligned with its host DM halo.

Following Hirata & Seljak (2004), the intrinsic shear of an object can be described as:

$$\gamma^I = -\frac{\bar{C}_1}{4\pi G} (\Delta_x^2 - \Delta_y^2, 2\Delta_x \Delta_y) S[\psi_P], \quad (25)$$

where  $\bar{C}_1 = 5 \times 10^{-14} M_{\odot}^{-1} h^{-2} \text{Mpc}^3$  is a normalisation constant, whose value was set by Brown et al. (2002) for low-redshift IA measurements in SuperCOSMOS (Hambly et al. 2001),  $G$  is the Newtonian gravitational constant,  $x$  and  $y$  are the Cartesian coordinates in the plane of the sky,  $S$  acts as a smoothing filter for  $\psi_P$ , which is the Newtonian potential at the time of galaxy formation, and  $\Delta$  is the comoving derivative.

The matter-intrinsic power spectrum for the NLA model is defined as:

$$P_{\delta\text{I}}(k, z) = C_1(z) P_{\delta\delta}(k, z), \quad (26)$$

where  $P_{\delta\delta}$  is the non-linear matter power spectrum and we define  $C_1$  following the implementation of PyCCL, such that:

$$C_1(z) = -\frac{A_1 \bar{C}_1 \rho_{\text{crit}} \Omega_m}{D(z)}, \quad (27)$$

where  $A_1$  is the IA amplitude,  $\rho_{\text{crit}}$  is the critical density,  $\Omega_m$  is the fractional matter density, and  $D(z)$  is the growth factor.

The TATT model, which is an extension of NLA that introduces a tidal torquing term, was also used to constrain the IA parameters, but there were strong degeneracies present in our TATT constraints, probably due to the low SNR in most of the cases under study, that made us decide to focus on the NLA model.

### 4.3 Correlation functions with spec- $z$

From the power spectra described in the previous sections, one can compute projected correlation functions along the LOS, like the ones presented in Section 3. If we assume Limber's approximation (Limber 1953), we can define these projected correlation functions using Hankel transforms, such that:

$$w_{\text{gg}}(r_p) = \int dz \mathcal{W}(z) \int \frac{dk_\perp k_\perp}{2\pi} J_0(k_\perp r_p) P_{\text{gg}}(k_\perp, z), \quad (28)$$

$$w_{\text{gp}}(r_p) = - \int dz \mathcal{W}(z) \int \frac{dk_\perp k_\perp}{2\pi} J_2(k_\perp r_p) P_{\text{gI}}(k_\perp, z), \quad (29)$$

where  $J_0$  and  $J_2$  are the 0th and 2nd-order Bessel functions of the first kind,  $k_\perp$  is the perpendicular wavelength and  $\mathcal{W}$  is the projection kernel defined in Mandelbaum et al. (2010):

$$\mathcal{W}(z) = \frac{n^i(z) n^j(z)}{\chi^2(z) d\chi/dz} \left[ \int dz \frac{n^i(z) n^j(z)}{\chi^2(z) d\chi/dz} \right]^{-1}, \quad (30)$$

with  $n^i$  the redshift distribution of the  $i$  sample and  $\chi(z)$  the comoving distance along the LOS at redshift  $z$ . In the case of eq. 28, the redshift distributions are those of the dense sample, so that  $n^i = n^j$ . Conversely, for eq. 29, two samples are used, the dense and shape samples. Note that the expressions in eq. 28 and eq. 29 are valid when we know the exact positions of the objects, that is, for the case of spec- $z$ s.

### 4.4 Correlation functions with photo- $z$

The modelling of projected correlation functions with photo- $z$  is more complex than when using spec- $z$ . The effect photo- $z$ s have on the correlation functions is to smear out the signal due to the scattering of galaxies along the LOS. The amplitude of this scattering depends on the precision of the photo- $z$ s. Even though PAUS photo- $z$ s have better precision than typical photo- $z$ s computed from BB surveys, the scatter is still not negligible. One approach to account for this scattering is to increase the range of the LOS integration, as we did in eq. 19, so that the scattered objects are brought back into the correlation. However, this is a subtle exercise, since one cannot arbitrarily increase this range given that uncorrelated objects might enter the correlation function and reduce the SNR. Here, we follow the procedure in Joachimi et al. (2011) and Samuroff et al. (2023) to implement the effect of photo- $z$  on the correlation functions.

For the case of the projected photometric GC correlation function,  $w_{\text{gg}}$ , the Limber integral of the galaxy power spectrum is defined as:

$$C_{\text{gg}}^{ij}(l | z_1, z_2) = \int_0^{\chi_{\text{hor}}} d\chi' \frac{p_n(\chi' | \chi(z_1)) p_n^j(\chi' | \chi(z_2))}{\chi'^2} P_{\text{gg}} \left( k = \frac{l + 0.5}{\chi'}, z(\chi') \right), \quad (31)$$

where  $\chi_{\text{hor}}$  is the comoving horizon distance and  $p_n(\chi' | \chi(z_1))$

quantifies the error distribution of the dense sample, which corresponds to the spec- $z$  distribution at the comoving distance  $\chi$  determined by the photo- $z$  value  $z_b = z_1$ . Here, the spec- $z$ s are the ones used in Navarro-Gironés et al. (2024) to quantify the accuracy of the photo- $z$ .

The expression in eq. 31 is transformed to angular space via:

$$\xi_{\text{gg}}^{ij}(\theta | z_1, z_2) = \frac{1}{2\pi} \int_0^\infty dl l J_0(l\theta) C_{\text{gg}}^{ij}(l | z_1, z_2). \quad (32)$$

Finally, as indicated in Joachimi et al. (2011), a change of coordinates is performed, such that  $z_m = (z_1 + z_2)/2$ ,  $r_p = \theta \chi(z_m)$  and  $\Pi = c(z_2 - z_1)/H(z_m)$ . With this, we can project the expression in eq. 32 along the LOS as:

$$w_{\text{gg}}^{ij}(r_p) = \int_{-\Pi_{\text{max}}}^{\Pi_{\text{max}}} d\Pi \int dz_m \mathcal{W}^{ij}(z_m) \xi_{\text{gg}}^{ij}(r_p, \Pi, z_m), \quad (33)$$

where now the redshift distributions entering  $\mathcal{W}(z)$  correspond to photo- $z$  distributions.

To cover the range of  $z_m$  and  $\Pi$  in eq. 33, we generate a 3-dimensional grid of  $\xi_{\text{gg}}^{ij}(r_p, \Pi, z_m)$ . This is done by selecting different  $\Pi$  and  $z_m$  values along our range of study, transforming them into  $z_1$  and  $z_2$  and performing the computations from eq. 31 and eq. 32. The  $\Pi$ -binning scheme is the same as the one employed in eq. 19.

The procedure for the computation of  $w_{\text{gp}}$  is very similar and is expressed in eq. 34–36. In this case, the error distributions in eq. 34 correspond to the dense ( $p_n^i$ ) and shape samples ( $p_e^j$ ):

$$C_{\text{gI}}^{ij}(l | z_1, z_2) = \int_0^{\chi_{\text{hor}}} d\chi' \frac{p_n^i(\chi' | \chi(z_1)) p_e^j(\chi' | \chi(z_2))}{\chi'^2} P_{\text{gI}} \left( k = \frac{l + 0.5}{\chi'}, z(\chi') \right), \quad (34)$$

$$\xi_{\text{gp}}^{ij}(\theta | z_1, z_2) = \frac{1}{2\pi} \int_0^\infty dl l J_2(l\theta) C_{\text{gI}}^{ij}(l | z_1, z_2), \quad (35)$$

$$w_{\text{gp}}^{ij}(r_p) = \int_{-\Pi_{\text{max}}}^{\Pi_{\text{max}}} d\Pi \int dz_m \mathcal{W}^{ij}(z_m) \xi_{\text{gp}}^{ij}(r_p, \Pi, z_m). \quad (36)$$

### 4.5 Contaminants to the correlation functions via magnification and galaxy-galaxy lensing

The quantities defined in eq. 33 and eq. 36 do not take into account other possible two-point correlation functions that act as contaminants to our quantities of interest. In particular, in the case of position-position correlation functions, magnification acts as a contaminant by modifying the galaxy number density. As a consequence, besides the term described in eq. 31, the magnification-magnification term (mm) and magnification-galaxy position terms (gm and mg) need to be taken into account. Thus, the terms contributing to the so-called source-source correlation function are:

$$C_{nn}^{ij}(l) = C_{\text{gg}}^{ij}(l) + C_{\text{gm}}^{ij}(l) + C_{\text{mg}}^{ij}(l) + C_{\text{mm}}^{ij}(l), \quad (37)$$

where  $C_{\text{gm}}^{ij} = C_{\text{mg}}^{ji}$ .

On the one hand, the galaxy-magnification contribution is defined

as:

$$C_{\text{gm}}^{ij}(l | z_1, z_2) = C_{\text{mg}}^{ji}(l | z_1, z_2) = 2(\alpha^j - 1) \int_0^{\chi_{\text{hor}}} d\chi' \frac{p_n(\chi' | \chi(z_1)) q_n^j(\chi' | \chi(z_2))}{\chi'^2} P_{g\delta} \left( k = \frac{l+0.5}{\chi'}, z(\chi') \right), \quad (38)$$

where  $q_x$  is the lensing weight function:

$$q_x(\chi) = \frac{3H_0^2 \Omega_m}{2c^2} \frac{\chi}{a(\chi)} \int_0^{\chi_{\text{hor}}} d\chi' p_x(\chi') \frac{\chi' - \chi}{\chi'}, \quad (39)$$

and we define the magnification bias  $\alpha$ , following the theory of magnification in magnitude-limited samples (Bartelmann & Schneider 2001; Joachimi & Bridle 2010; Fortuna et al. 2021b), to be proportional to the slope of the faint-end of the logarithmic galaxy count ( $\log n$ ) over a given magnitude range, in our case:

$$\alpha(i_{\text{AB}}) = 2.5 \frac{d \log [n(i_{\text{AB}})]}{d i_{\text{AB}}}. \quad (40)$$

Table 2 shows the  $\alpha(i_{\text{AB}})$  values for the different configurations studied in this analysis.

On the other hand, the magnification-magnification contribution is defined as:

$$C_{\text{mm}}^{ij}(l | z_1, z_2) = 4(\alpha^i - 1)(\alpha^j - 1) \int_0^{\chi_{\text{hor}}} d\chi' \frac{q_n^i(\chi' | \chi(z_1)) q_n^j(\chi' | \chi(z_2))}{\chi'^2} P_{\delta\delta} \left( k = \frac{l+0.5}{\chi'}, z(\chi') \right). \quad (41)$$

In the case of position-shape correlation functions, the sources of contamination are the magnification and the galaxy-galaxy lensing, which introduces a signal produced by the lensing of a background galaxy by a foreground galaxy. We can decompose all the terms contributing to the source-shape correlation function as:

$$C_{ne}^{ij}(l) = C_{\text{gl}}^{ij}(l) + C_{\text{gG}}^{ij}(l) + C_{\text{mI}}^{ij}(l) + C_{\text{mG}}^{ij}(l). \quad (42)$$

The contribution from the galaxy-shear is defined via:

$$C_{\text{gG}}^{ij}(l | z_1, z_2) = \int_0^{\chi_{\text{hor}}} d\chi' \frac{p_n(\chi' | \chi(z_1)) q_e^j(\chi' | \chi(z_2))}{\chi'^2} P_{g\delta} \left( k = \frac{l+0.5}{\chi'}, z(\chi') \right), \quad (43)$$

while the contribution from the magnification-shear is:

$$C_{\text{mG}}^{ij}(l | z_1, z_2) = 2(\alpha^i - 1) \int_0^{\chi_{\text{hor}}} d\chi' \frac{q_n^i(\chi' | \chi(z_1)) q_e^j(\chi' | \chi(z_2))}{\chi'^2} P_{\delta\delta} \left( k = \frac{l+0.5}{\chi'}, z(\chi') \right). \quad (44)$$

Finally, the contribution from the magnification-intrinsic shear is given by:

$$C_{\text{mI}}^{ij}(l | z_1, z_2) = 2(\alpha^i - 1) \int_0^{\chi_{\text{hor}}} d\chi' \frac{p_n(\chi' | \chi(z_1)) q_e^j(\chi' | \chi(z_2))}{\chi'^2} P_{\delta\delta} \left( k = \frac{l+0.5}{\chi'}, z(\chi') \right). \quad (45)$$

Thus, when constraining the GC and IA parameters, all the terms expressed in eq. 37 and eq. 42 are taken into account. The effects of the contaminants in our analyses can be found in Appendix F.

#### 4.6 Likelihood analysis

With the theoretical predictions (Sections 4.4 and 4.5) and the measurements (Section 3) of our observables, we carry out a likelihood analysis to constrain the galaxy bias and the IA parameters. The likelihood ( $L$ ) of a data vector ( $D$ ) with respect to a given model ( $M$ ) evaluated at the set of parameters ( $\theta$ ), given a certain covariance matrix ( $C$ ), can be expressed as:

$$-2 \ln L(\theta) = \chi_{\text{fit}}^2 = \sum_{i=1}^n \sum_{j=1}^n [D_i - M_i(\theta)]^T C_{ij}^{-1} [D_j - M_j(\theta)], \quad (46)$$

where  $n$  is the number of data points and  $\chi_{\text{fit}}^2$  is the goodness of the fit.

However, given the limited area used for this analysis, we are restricted to a few JK regions for each of the configurations we study. This leads to an also limited resolution in the covariance matrix, which is proportional to (Gaztañaga & Scoccimarro 2005):

$$\Delta \bar{C} \sim \sqrt{\frac{2}{N_{\text{JK}}}}, \quad (47)$$

where  $\bar{C}_{ij} = C_{ij} / \sqrt{\sigma_{C,i} \sigma_{C,j}}$  is the correlation matrix, with  $\sigma_{C,i}$  the square root of the diagonal of  $C$  evaluated at position  $i$ . As a consequence, the smaller the number of JK regions, the more noise in  $\bar{C}$  might appear, which can lead to instabilities when computing the inverse of the covariance matrix in eq. 46. To solve this problem, we perform a singular value decomposition (SVD) of the normalised covariance matrix:

$$\bar{C}_{ij} = (U_{ik})^T D_{kl} V_{lj}, \quad (48)$$

where  $D_{ij} = \lambda_i^2 \delta_{ij}$  is a diagonal matrix with  $\lambda_i^2$  values in the diagonal, which correspond to the singular values of the decomposition, and  $U_{ij}$  and  $V_{ij}$  are orthogonal matrices that decompose  $\bar{C}$  into  $D_{ij}$ . The singular values represent the independent number of modes in the covariance matrix, and values too close to zero may cause noise in  $\bar{C}$ . When computing the inverse covariance in eq. 46, we keep the dominant singular values by setting the condition:

$$\lambda_i^2 > \sqrt{\frac{2}{N_{\text{JK}}}}, \quad (49)$$

which corresponds to the resolution limit specified in eq. 47. Thus, the  $\chi_{\text{fit}}^2$  in eq. 46 in the case of applying a SVD is redefined as:

$$\chi_{\text{fit,SVD}}^2 = \sum_{i=1}^n \sum_{j=1}^n \bar{\Delta}_i^T \bar{C}_{\text{SVD},ij}^{-1} \bar{\Delta}_j, \quad (50)$$

where  $\bar{C}_{\text{SVD}}^{-1}$  is the inverse of the normalised covariance matrix after performing SVD, and we have defined the difference  $\bar{\Delta}_i \equiv D_i - M_i(\theta)$  and its normalisation as  $\bar{\Delta}_i = \Delta_i / \sigma_{C,i}$ . We further define the reduced  $\chi_{\text{fit,SVD}}^2$  as:

$$\chi_{\nu, \text{fit,SVD}}^2 = \frac{\chi_{\text{fit,SVD}}^2}{N_{\text{d.o.f.}}}, \quad (51)$$

where  $N_{\text{d.o.f.}}$  corresponds to the number of degrees of freedom, which we define as the number of points after performing the SVD minus 3, the number of fitted parameters ( $b_1$ ,  $b_2$  and  $A_1$ ).

In order to sample the posterior distribution, we employ `emcee` (Foreman-Mackey et al. 2013), a python implementation of Goodman and Weare's Affine Invariant Markov chain Monte Carlo (MCMC)

**Table 1.** Priors for the galaxy bias and the NLA model.  $\mathcal{U}$  is a uniform prior, with  $\mathcal{U}(\min, \max)$ , while  $\mathcal{N}$  represents a Gaussian with  $\mathcal{N}(\mu, \sigma)$ .

Parameter	Prior
$b_1$	$\mathcal{U}(0, 2)$
$b_2$	$\mathcal{N}(0, 0.5)$
$A_1$	$\mathcal{U}(-12, 12)$

ensemble sampler (Goodman & Weare 2010). We use the integrated autocorrelation time ( $\tau_f$ ) to quantify the Monte Carlo error. The idea behind this quantity is that the samples of the chain are not independent, and one has to estimate the effective number of independent samples. This number can be quantified as  $N/\tau_f$ , with  $N$  the total number of sampled points. From this, a convergence criterion can be established, where we impose that  $N/\tau_f > 100$  and that  $\tau_f$  changes by less than 1% every 100 iterations. Besides this convergence criterion, we set the maximum number of iterations to 10000 per ‘‘walker’’, with a total of 32 ‘‘walkers’’. However, in all the cases analysed in this study, the convergence is reached before the maximum number of iterations. Finally, when plotting the results from the chain, we set the emcee ‘‘thin’’ parameter to  $\tau_f/2$  to select independent points. We note that all these specifications may vary depending on the case under study, and that we follow the recommendations set by the available documentation from emcee<sup>2</sup>. As a consistency test, we ran some of our chains using Nautilus (Lange 2023), which is a nested sampler, and found the same constraints.

Table 1 shows the priors used for  $b_1$ ,  $b_2$  and  $A_1$  when fitting the joint  $w_{gg} \cup w_{gp}$  data vector. In the case of  $b_1$  and  $A_1$ , we set similar flat priors as those described in Samuroff et al. (2023). The differences are that the  $b_1$  prior is reduced from [0, 3] to [0, 2], since our samples usually present a galaxy bias closer to  $b_1 \sim 1$ , while the  $A_1$  prior is increased from [-8, 8] to [-12, 12], to account for more extreme  $A_1$  values. For the 2nd-order galaxy bias,  $b_2$ , we set a Gaussian prior with a mean of 0 and standard deviation of 0.5.

The scale cuts in our combined data vectors are fixed to  $r_{p,\min} = 2.0 h^{-1}\text{Mpc}$  for  $w_{gg}$ , which is typically the minimum separation we can reach with the non-linear galaxy bias model presented in Section 4.1. For the case of  $w_{gp}$ , we tried different options, which are reviewed in more detail in Appendix G, but decided to use the same  $r_{p,\min} = 2.0 h^{-1}\text{Mpc}$  as in  $w_{gg}$  for the main constraints in this paper. Note that this is a different approach from what is commonly used in the literature for the NLA model, where they usually set  $r_{p,\min} = 6.0 h^{-1}\text{Mpc}$ , such as in Samuroff et al. (2023), Johnston et al. (2019) and Fortuna et al. (2021b), amongst others. Nevertheless, this scale cut is more justified by the limitation in modelling the  $w_{gg}$  estimator, which is estimated from linear galaxy bias in these previous works, rather than by a limitation of the NLA model itself. This is proven in Paviot et al. (in prep.), where they include an analysis of the dependence on the scale cuts when using linear and non-linear galaxy bias in the Flagship simulation. Additionally, given the reduced number of data points for the PAUS measurements, a scale cut of  $r_{p,\min} = 2.0 h^{-1}\text{Mpc}$  is preferable over a scale cut of  $r_{p,\min} = 6.0 h^{-1}\text{Mpc}$ , since it increases the available points to fit in our data vector, from 3 to 5, respectively. Finally, we do not set a  $r_{p,\max}$  value in the modelling, so that we include the maximum projected separation that we can measure in the PAUS wide fields, since it remains within a range that can be reliably modelled.

<sup>2</sup> <https://emcee.readthedocs.io/en/stable/>

## 5 RESULTS

The results we obtain from the GC and IA measurements are shown in this section. Each of the measurements is complemented by the modelled signal fitted to it, following the methodology presented in Sections 4.4–4.6. The results we present here correspond to the brighter sample (W1+G09+W3 with  $i_{AB} < 22$ ), while the comparison of  $A_1$  as a function of colour, luminosity, stellar mass and redshift, for both the brighter and fainter samples (W1+W3 with  $i_{AB} < 22.5$ ), is deferred to Appendix A.

To study the dependence of IA on physical properties, we split our measurements by colour, defining a red and a blue shape sample. Furthermore, together with the colour split, we study different scenarios where we separate the sample in 3 equipopulated luminosity, stellar mass or redshift bins. As a consequence of these divisions, we obtain a total of 20 different scenarios, for which we measure and model the photometric GC and the IA. Note that we first split the objects of the shape sample by colour and, later, by equipopulated bins, so as to obtain the same number of objects in each shape subsample. This may result in slightly different boundaries in the luminosity, stellar mass and redshift bins for red and blue objects. As for the dense samples, we also split them in luminosity, stellar mass and redshift bins, to account for their different redshift ranges. However, we do not separate them by colour, as this results in higher SNR. This does not represent a problem, since the purpose of measuring the GC here is to obtain the galaxy bias of the dense sample, which is required in the  $w_{gp}$  estimator (eq. 36). Even though the dense samples are not separated by colour, the slightly different luminosity, stellar mass and redshift ranges for red and blue shape samples may cause the dense subsamples of both cases to differ, although, in general, the vast majority of objects coincide.

Table 2 summarises some of the properties of the 20 different configurations by showing the number of objects in the dense ( $N_D$ ) and the shape ( $N_S$ ) samples, the number of JK regions, the mean luminosity, stellar mass and redshift, the precision of the photo- $z$  as a function of  $\sigma_{68}(\Delta z)$  (eq. 3), the  $\alpha$  parameter (eq. 40) and the reduced  $\chi^2$  of SNR ( $\chi^2_{\nu, \text{SNR}}$ ) for the  $w_{gp}$  and  $w_{gx}$  estimates, defined below.

The number of objects in the dense samples is affected by the different luminosity, stellar mass and redshift ranges defined for red and blue shape samples. Thus,  $N_D$  varies for red and blue shape galaxies across luminosity, stellar mass and redshift bins. As for  $N_S$ , it is lower for red than for blue objects, as seen in Fig. 2. Hence, we expect larger error bars in the measurements of red objects.

The number of angular JK regions is the sum of the angular regions of the three fields, which corresponds to 18 angular JK regions, as discussed in Section 3. In the case where we only perform the analysis as a function of colour, this is complemented by 3 cuts in equipopulated redshift bins, defining JK regions in the radial direction as well, which results in a total of 54 JK regions. Given that the IA signal does depend on the redshift, the definition of JK regions in the radial direction might affect the covariance matrix, since the different regions might not be independent but conserve some evolution with redshift. This is reviewed in Appendix E, where we find that the JK errors are consistent with the ensemble covariance matrix. The same redshift bins used to define JK regions in the colour-based division are also employed to define our samples divided by redshift. Thus, each of these cases have 18 JK regions. Finally, in the case where we split our samples either by luminosity or stellar mass bins, we need to define new radial binnings for the JK regions. The reason for this is that each luminosity and stellar mass bin exhibits a different redshift distribution, making it impossible to define the same equipopulated

redshift bins. In this case, we decide to divide the redshift space for each scenario in 2 equipopulated redshift bins, accounting for 36 JK regions in each case.

The  $\sigma_{68}(\Delta z)$  is also shown for each configuration. As expected, in the case of the samples divided by redshift bins, the sample with the higher redshift cut presents a lower photo- $z$  precision. In the case of the luminosity and stellar mass bins, we note that they are closely related with redshift, with the lower bins presenting lower redshift means. Nevertheless, this does not necessarily translate into worse  $\sigma_{68}(\Delta z)$  values, as these properties are also linked to apparent magnitude, so that fainter objects correspond to lower luminosity and stellar mass bins. As photo- $z$  precision also depends on the apparent magnitude, with fainter objects having less precise photo- $z$ , this counteracts the relation between luminosity or stellar mass and mean redshift. In that sense, for the case of red objects, the photo- $z$  precision increases as we move towards higher luminosity and stellar mass bins, while in the case of blue objects, the photo- $z$  precision is quite stable.

We define the reduced  $\chi^2$  of SNR ( $\chi^2_{\nu, \text{SNR}}$ ) for the  $w_{\text{gp}}$  and  $w_{\text{gx}}$  estimates as:

$$\chi^2_{\nu, \text{SNR}} = \frac{\sum_{i=1}^n \sum_{j=1}^n \bar{D}_i^T \bar{C}_{\text{SVD}, ij}^{-1} \bar{D}_j}{N_{\text{d.o.f.}} - 1}, \quad (52)$$

where  $\bar{D}_i = D_i / \sigma_{C,i}$  is the normalised data vector ( $D_i$ ) over the square root of the diagonal covariance matrix ( $\sigma_{C,i}$ ), and  $N_{\text{d.o.f.}}$  is the number of degrees of freedom after performing the SVD (see Section 4.6). The  $\chi^2$  employed in this equation is similar to that presented in eq. 50, but this time the model is replaced by the null value, in order to check for detection of IA signal or systematics. Furthermore, no scale cuts are applied in this case, since we are also interested in the IA signal at small scales. It is important to note that this test helps to identify the detection of signal ( $w_{\text{gp}}$ ) or systematics ( $w_{\text{gx}}$ ), but it is not a conclusive test. The reason for this is that, in some cases, especially for the systematics, the value of  $\chi^2_{\nu, \text{SNR}}$  increases because of uncorrelated points in  $w_{\text{gx}}$ . Thus, to confirm detection of IA or systematics, the signal has to be correlated for different projected separations. Otherwise, we risk misinterpreting noise in the measurements as signal or systematics. However, this test is useful for identifying non-detections, in the sense that a low value of  $\chi^2_{\nu, \text{SNR}}$  indicates correlations consistent with 0. Regarding the high values of  $\chi^2_{\nu, \text{SNR}}$  in  $w_{\text{gx}}$  in Table 2, we also measured  $\chi^2_{\nu, \text{SNR}}$  for  $w_{\text{gx}}$  in the MICE simulation and found that, for the area analysed in this work, some of the values were large for some PAUS-like triplets, but they decreased and became consistent with 0 for larger areas. This supports the idea that finding large values of  $\chi^2_{\nu, \text{SNR}}$  in  $w_{\text{gx}}$  for PAUS is not unexpected in some cases.

Based on the values of  $\chi^2_{\nu, \text{SNR}}$  for  $w_{\text{gp}}$ , we find a mild detection of IA for red objects and no detection for blue galaxies when we only split the sample by colour. The separations by luminosity and by stellar mass bins show an increase of  $\chi^2_{\nu, \text{SNR}}$  as we move towards brighter and more massive red galaxies, whereas no IA signal is observed for blue objects. Finally, the split in redshift bins for red galaxies shows no IA detection for the lowest redshift bin, while a clear IA signal is seen for the intermediate and highest bins. For blue galaxies, there is again no IA detection, except for the intermediate redshift bin, where a mild detection of IA seems to be present, although further analyses may be needed for confirmation. As for the values of  $\chi^2_{\nu, \text{SNR}}$  for  $w_{\text{gx}}$ , in general they indicate that we are not affected by systematics. We have analysed the cases where  $\chi^2_{\nu, \text{SNR}} > 2$  for  $w_{\text{gx}}$  (which we do not show here for conciseness), and found that they are driven by uncorrelated points.

## 5.1 Division by colour

Fig. 6 shows the GC (left) and the IA (right) measurements as black dots, in terms of  $w_{\text{gg}}$  and  $w_{\text{gp}}$ , respectively, with error bars corresponding to the square root of the diagonal of the JK covariance. The GC measurements correspond to the dense sample, while the IA ones to the red (top) and blue (bottom) shape samples. These measurements are accompanied by shaded areas, which represent the 68% best fit model to the measurements. The dashed vertical lines show the  $r_p = 2 \text{ h}^{-1} \text{Mpc}$  scale cut below which we do not fit the model. We find a clear signal of IA for red galaxies, while there is alignment consistent with 0 for blue ones, as seen from the values of  $w_{\text{gp}} \chi^2_{\nu, \text{SNR}}$  in Table 2. These findings are in line with those from previous analyses by Johnston et al. (2021a), who only studied the W3 field.

Fig. 7 shows the  $1\sigma$  and  $2\sigma$  contour plots for the galaxy bias parameters,  $b_1$  and  $b_2$ , and for the IA amplitude,  $A_1$ , for red and blue galaxies. In terms of the  $A_1$  parameter, its amplitude peaks above 2 for the red sample, with  $A_1 = 2.78^{+0.83}_{-0.82}$ , while for the blue sample it is consistent with 0, as was also seen in Fig. 6, with  $A_1 = 0.68^{+0.53}_{-0.51}$ . As discussed in Appendix G, the  $w_{\text{gg}} \cup w_{\text{gp}}$  fits for blue galaxies can be pushed towards smaller scales without an increase in  $\chi^2_{\nu, \text{fit}, \text{SVD}}$ , yielding narrower constraints in  $A_1$ . In particular, we obtain a value of  $A_1 = 0.53^{+0.32}_{-0.31}$  when setting  $r_{p, \text{min}} = 1.0 \text{ h}^{-1} \text{Mpc}$  in  $w_{\text{gp}}$ . In the case of the  $b_1$  and  $b_2$  terms, since we are not splitting the dense sample by colour, we obtain very similar values for both red and blue galaxies. The differences we observe might come from the fact that the SNR of the  $w_{\text{gp}}$  estimator is different for red and blue galaxies, given that there are 3–4 times more blue than red objects. So, even though the constraining power of the galaxy bias parameters mostly comes from  $w_{\text{gg}}$  (given its higher SNR with respect to  $w_{\text{gp}}$ ), the  $w_{\text{gp}}$  estimator also affects the constraints through eq. 36. Note that the galaxy bias parameter that eq. 36 constrains is  $b_1$ , since  $P_{\text{gl}}(k, z) = b_1 P_{\delta\text{I}}(k, z)$  (eq. 24). However, as an indirect consequence, the  $b_2$  term might be affected through  $w_{\text{gg}}$  by the change in  $b_1$ . This effect will be slightly different depending on the number of objects in the shape sample. Another consideration that might affect the difference between the galaxy bias parameters for red and blue galaxies is related with the term  $p_e(\chi' \mid \chi(z_i))$  in eq. 34, which accounts for the error distribution associated to modelling correlation functions with photo- $z$ . Ideally, the effect of this term should not depend on colour, luminosity, stellar mass or redshift. However, since it involves knowledge of spec- $z$ s and the availability of these does depend on these properties, the constraining power on  $b_1$  and  $b_2$  may also be affected by this factor.

## 5.2 Division by colour, luminosity and stellar mass

In this section, we analyse the GC and IA signals by first splitting the samples by colour and luminosity bins. The luminosity is computed from the apparent  $r_{\text{AB}}$ -band magnitude from CFHTLenS, in the case of the W1 and W3 fields, and from KiDS, in the case of the G09 field. First, we compute the absolute magnitude from:

$$M_r = m_r - 5 \log_{10}(D_L / 10\text{pc}) + 2.5 \log_{10} \frac{\phi_{r,z}}{\phi_{r,z=0}}, \quad (53)$$

where  $M_r$  and  $m_r$  correspond to the absolute and apparent magnitudes of the  $r_{\text{AB}}$ -band, respectively.  $D_L$  is the luminosity distance and the last term corresponds to the  $k$ -correction, with  $\phi_{r,z}$  and  $\phi_{r,z=0}$  being the flux of the galaxy in the  $r$ -band at redshift  $z$  (the redshift at which the object is located) and  $z = 0$ , respectively. The

**Table 2.** Number of objects in the dense ( $N_D$ ) and shape ( $N_S$ ) samples, number of JK regions ( $N_{JK}$ ), mean luminosity, mean stellar mass, mean redshift,  $\sigma_{68}$ , magnification bias and  $\chi^2_{\nu, \text{SNR}}$  for red and blue galaxies for the IA cases studied in this paper.

Sample	All	Lum. bin 1	Lum. bin 2	Lum. bin 3	$M_\star$ bin 1	$M_\star$ bin 2	$M_\star$ bin 3	$z$ bin 1	$z$ bin 2	$z$ bin 3
$N_D$ red	460914	162321	98180	186320	307905	84652	64358	213232	117675	130007
$N_D$ blue	460914	154322	167494	127300	113610	125747	218398	133762	159292	167860
$N_S$ red	82269	27355	25719	25611	27301	26222	26942	27284	27440	27545
$N_S$ blue	279336	91929	89094	90457	92075	92214	93257	91975	93510	93851
$N_{JK}$	54	36	36	36	36	36	36	18	18	18
$\log_{10} <L/L_0>$ red	-0.59	-0.91	-0.58	-0.27	-0.86	-0.57	-0.34	-0.71	-0.59	-0.48
$\log_{10} <L/L_0>$ blue	-0.58	-1.15	-0.51	-0.1	-1.09	-0.49	-0.18	-1.06	-0.5	-0.2
$\log_{10} <M_\star/M_\odot>$ red	10.62	10.25	10.68	10.98	10.17	10.66	11.04	10.35	10.63	10.88
$\log_{10} <M_\star/M_\odot>$ blue	9.88	9.19	9.97	10.47	9.1	9.93	10.59	9.29	9.97	10.37
$\langle z \rangle$ red	0.55	0.48	0.59	0.63	0.43	0.57	0.67	0.36	0.55	0.75
$\langle z \rangle$ blue	0.48	0.28	0.51	0.68	0.31	0.5	0.64	0.25	0.46	0.73
$\sigma_{68}$ red	0.008	0.026	0.014	0.005	0.018	0.013	0.006	0.005	0.006	0.014
$\sigma_{68}$ blue	0.014	0.016	0.02	0.013	0.017	0.014	0.013	0.005	0.015	0.017
$\alpha(i_{AB})$ red	0.93	1.28	0.9	0.68	1.15	0.63	0.42	0.63	0.82	1.65
$\alpha(i_{AB})$ blue	0.93	1.3	0.9	0.6	1.48	1.06	0.62	0.62	0.72	1.46
$w_{gp} \chi^2_{\nu, \text{SNR}}$ red	2.25	2.08	3.00	3.62	1.50	2.00	3.13	0.65	6.85	3.31
$w_{gp} \chi^2_{\nu, \text{SNR}}$ blue	0.56	0.81	1.55	0.71	0.91	1.09	0.55	0.68	2.78	1.68
$w_{gx} \chi^2_{\nu, \text{SNR}}$ red	1.06	1.49	1.84	0.97	2.21	1.28	0.61	0.31	0.83	0.78
$w_{gx} \chi^2_{\nu, \text{SNR}}$ blue	2.80	2.09	2.02	0.65	0.87	0.59	0.79	0.92	0.54	1.63

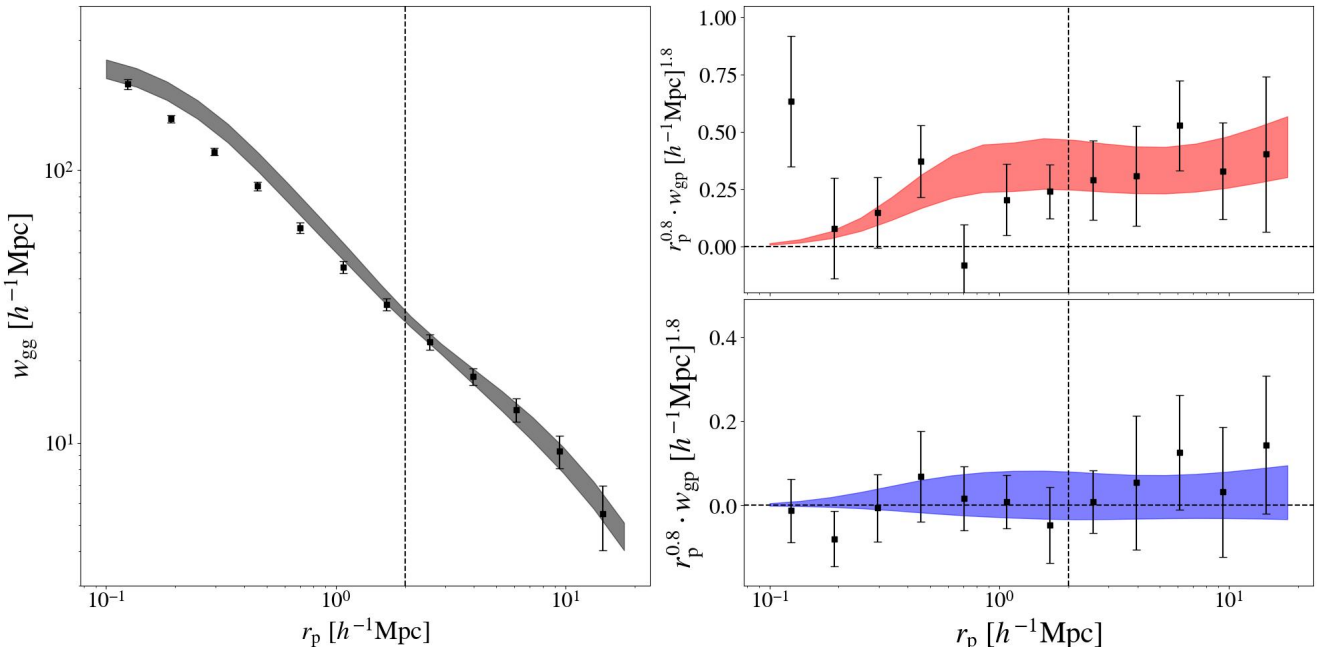


**Figure 6.** GC (left,  $w_{gg}$ ) and IA (right,  $w_{gp}$ ) measurements. The shaded areas show the  $1\sigma$  uncertainty in the best fit using the non-linear galaxy bias and the NLA models. The dashed vertical lines indicate the scale cuts. The GC measurements correspond to the dense sample, while the IA ones to the red (top) and blue (bottom) shape samples.

$k$ -correction is computed using the BCNz code (Eriksen et al. 2019), which outputs the flux of each galaxy for the redshift range  $z = [0, 2]$ .

A caveat in the computation of the absolute magnitude is the fact that we are using the  $r_{AB}$ -band magnitude from different surveys, which may lead to differences in the number counts for the fields under study. This was the case for Fig. 3 from Navarro-Gironés et al. (2024), where there was the need to add an offset to the  $i_{AB}$  magnitude from KiDS in order to match that of CFHTLenS. A similar scenario happens in this situation, where we need to add an offset of

+0.4 in the  $r_{AB}$  absolute magnitude of the KiDS field to match the distribution of the CFHTLenS fields. Moreover, it is worth noting that we do not account for the evolution of the stellar population with redshift in the computation of eq. 53, usually referred to as “e-correction” (Poggianti 1997). As a result, we do not correct for the passive evolution that red galaxies undergo over time, which causes galaxies of a given mass to appear brighter at higher redshifts. This justifies the need to study the IA dependence as a function of stellar mass, as will be done in Sec. 5.2.

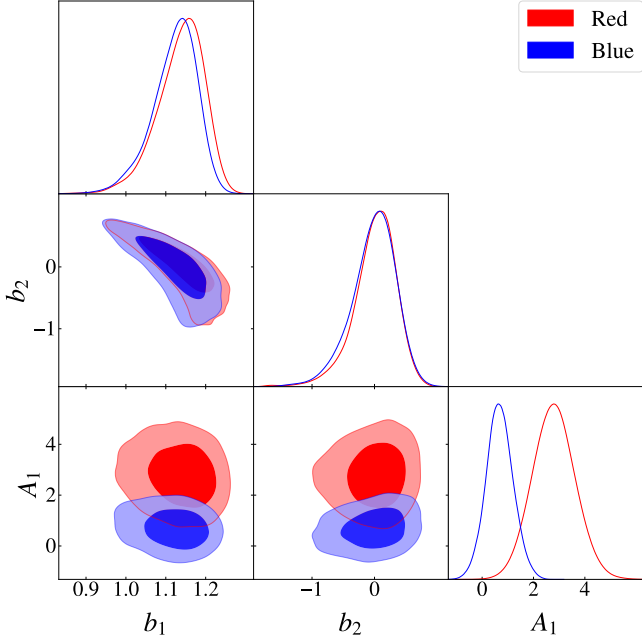


**Figure 7.**  $1\sigma$  and  $2\sigma$  contour plots for the galaxy bias,  $b_1$  and  $b_2$ , and the IA,  $A_1$ , parameters for red and blue galaxies.

Once the absolute magnitude is computed through eq. 53, we compute the normalised luminosity with respect to the absolute magnitude  $M_{r,0} = -22$ , in order to compare with the literature, so that:

$$M_r - M_{r,0} = -2.5 \log_{10} \frac{L_r}{L_0}. \quad (54)$$

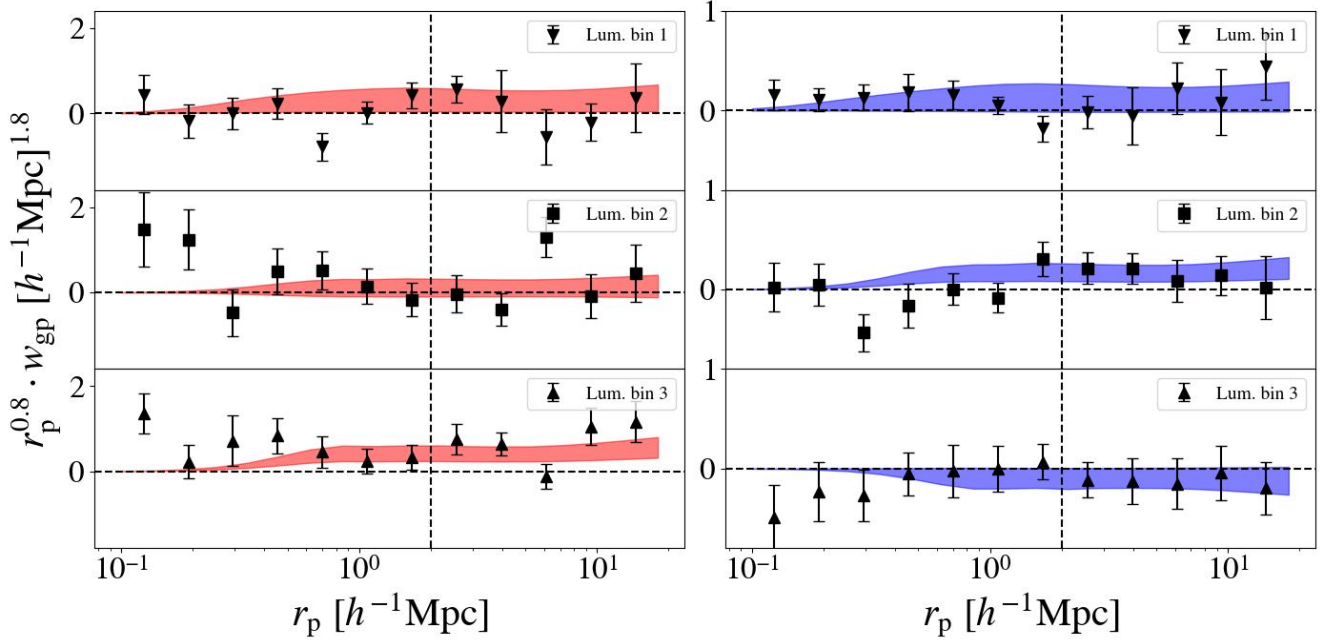
We generate three equipopulated luminosity bins, after splitting by colour, which generate samples with means of  $\log_{10}(L_r/L_0) \sim -0.91(-1.15)$ ,  $\log_{10}(L_r/L_0) \sim -0.58(-0.51)$  and  $\log_{10}(L_r/L_0) \sim -0.27(-0.1)$  for the red (blue) samples. We refer to these luminosity bins as luminosity bin 1, 2 and 3, respectively.

Fig. 8 shows the  $w_{gp}$  measurements and modelling, including the division into three luminosity bins. We focus here on the IA measurements, instead of also showing the GC measurements, as in Fig. 6. However, we note that the GC shows lower values for luminosity bin 1, corresponding to the faintest objects, than for bins 2 and 3, which present similar GC values, with slightly lower values for luminosity bin 3. On the left-hand side plot, the evolution of the IA measurements as a function of luminosity for red objects is indicated by upside down triangles, squares and face up triangles for the luminosity bins 1, 2 and 3, respectively. The same configuration, but for blue galaxies, is shown on the right-hand side plot. As in the case of Fig. 6, the dashed vertical lines at  $r_p = 2 h^{-1}$ Mpc indicate the minimum separation we include in the modelling of our measurements. The shaded areas show the best fit model to the data, together with its  $1\sigma$  uncertainty. In the case of the IA measurements for red objects, the signal is consistent with 0 for the two faintest luminosity bins, whereas a positive alignment is observed for luminosity bin 3. This is in agreement with the  $\chi^2_{\nu, \text{SNR}}$  in Table 2, with a higher  $\chi^2_{\nu, \text{SNR}}$  in luminosity bin 2 than in luminosity bin 1 explained by the higher variance of the former. In the case of blue galaxies, the alignment is consistent with 0 for luminosity bin 1, although for the majority of the  $r_p$  separations there is a small trend of positive alignment. Luminosity bin 2 is also consistent with 0 for most scales, although there

is a hint of positive alignment at  $r_p > 2 h^{-1}$ Mpc, as indicated by the blue line that corresponds to the modelling. Finally, for the brightest luminosity bin, luminosity bin 3, there is a trend of negative alignment for most scales, although the upper limits of the measurements are also consistent with 0.

The dependence of  $A_1$  as a function of luminosity is shown in Fig. 9. For the PAUS results (squares), the IA amplitude of luminosity bin 1 for red objects is centred at  $A_1 \sim 2$ , while at  $A_1 \sim 1$  for blue galaxies. For the case of the intermediate luminosity bin, the  $A_1$  amplitude is centred on  $A_1 \sim 1$  for the red sample, although consistent with 0, and at  $A_1 \sim 1 - 2$  for the blue one. Finally, for the brightest luminosity bin, there is a clear IA amplitude for red objects, centred on  $A_1 \sim 4$ , with the alignment being in agreement with 0 for blue galaxies. Together with the PAUS results, we include constraints from previous analyses. These constraints correspond to studies analysing the IA-luminosity evolution and come from LOWZ (Singh et al. 2015), MegaZ LRG+SDSS (Joachimi et al. 2011), red and blue GAMA+SDSS (Johnston et al. 2019), KiDS-1000 (Fortuna et al. 2021b), DES Y3 RML (redMaGiC low-z, Samuroff et al. 2023), DES Y3 RMH (redMaGiC high-z, Samuroff et al. 2023), DES Y3-eBOSS LRGs, DES Y3-CMASS, UNIONS-eBOSS LRGs and UNIONS-CMASS (the last four coming from Hervas Peters et al. 2024). We note that the DES Y3-eBOSS LRGs and DES Y3-CMASS results used here are taken from Hervas Peters et al. 2024, rather than Samuroff et al. 2023, because the latter omits the mixed term of the clustering power spectrum and galaxy shape noise in its covariance matrix. As indicated in Hervas Peters et al. 2024, this term becomes dominant at  $r_p \gtrsim 29 h^{-1}$ Mpc, and its omission leads to potential biases and an underestimation of the error bars in the fits from Samuroff et al. 2023. We also note that the fits of all these previous analyses take as minimum  $r_p$  scales larger than  $6 h^{-1}$ Mpc, in contrast to our choice of  $2 h^{-1}$ Mpc. These previous fits indicate an  $A_1 - L$  relation based on a broken power law, where the slope for  $\log_{10}(L/L_0) < -0.2$  is shallower than above it. This is indicated by the dotted blue line for low luminosities (which is fitted with the GAMA+SDSS results) and the solid purple line for high luminosities (fitted with the MegaZ LRG+SDSS measurements). This double power law is thought to be driven by the relation between luminosity-to-halo-mass relation, which is also described by a double power law. This was discussed in Fortuna et al. (2025), where a single power law relation was found between IA amplitude and halo mass. We do not try to fit a power law to our data for two reasons. First, the number of data points is reduced, with 3 luminosity bins, so that the power law one can obtain would not be well constrained. Second, for some points, the error bars are quite large, making a power law fit difficult. Thus, we opt for comparing our measurements with the literature. However, we note that the samples used in the literature correspond to red galaxies and vary in some physical properties with respect to the PAUS samples, so that it is expected that there are differences in the  $A_1 - L$  relation they follow.

One of the most important goals from the study of IA with PAUS is to extend the  $A_1 - L$  relation towards fainter objects. In this regard, the two fainter luminosity bins we use lie in the luminosity range dominated by the GAMA+SDSS power law (dotted blue line), even extending the luminosity range with respect to previous measurements down to  $\log_{10}(L/L_0) \sim -0.9$  for red objects and down to  $\log_{10}(L/L_0) \sim -1.15$  for blue ones. Conversely, the brighter luminosity bin lies at the intersection between the broken power law from previous studies. For the case of red galaxies, the lowest luminosity bin agrees with the power law from the GAMA+SDSS measurements, while the intermediate luminosity bin agrees more with the power law from the MegaZ LRG+SDSS measurements. Neverthe-



**Figure 8.** IA measurements in terms of  $w_{gp}$  for the three luminosity bins, for red (left) and blue (right) objects. The shaded areas show the  $1\sigma$  uncertainty in the best fit using the NLA model. The dashed vertical lines indicate the scale cuts.

less, both power laws are less than  $1\sigma$  away from the intermediate luminosity bin constraint. As for the highest luminosity bin, the PAUS measurements agree with those from previous measurements. Even though we also include the measurements of blue galaxies in this plot, we do not expect them to follow the power laws from previous literature, since those were computed for red populations. In addition to the  $A_1$  fits for blue galaxies, we show in Fig. 9 their weighted mean, with its  $1\sigma$  uncertainty, as a shaded blue band, where we find  $A_1 = 1.26^{+0.57}_{-0.57}$ , which is consistent with 0 at  $\sim 2\sigma$ .

In order to complement the IA dependence as a function of luminosity, we also study the IA dependence as a function of stellar mass, where the latter is derived from CIGALE. As in the case of the luminosity, we divide the stellar mass range in 3 equipopulated bins, with means of  $\log_{10}(M_\star/M_\odot) \sim 10.17(9.1)$ ,  $\log_{10}(M_\star/M_\odot) \sim 10.66(9.93)$  and  $\log_{10}(M_\star/M_\odot) \sim 11.04(10.59)$  for red (blue) galaxies. While the literature has mainly focused on the dependence of IA on halo mass (Joachimi et al. 2013; van Uitert & Joachimi 2017; Piras et al. 2017; Xia et al. 2017; Fortuna et al. 2025), finding that IA increases with it, this property is not available in our dataset. Instead, since stellar mass is available and is correlated with halo mass (Moster et al. 2013; Behroozi et al. 2013), and also depends on galaxy properties linked to IA, such as morphology and formation history, we choose to analyse the dependence of IA on stellar mass. In that sense, there exist studies of the dependence of IA on stellar mass in hydrodynamical simulations (Chisari et al. 2015; Hilbert et al. 2017; Bate et al. 2020; Shi et al. 2021) that, in general, also show increasing alignments with mass, while observational studies still remain scarce.

As for the relation between luminosity and stellar mass, it is usually described by the stellar mass-to-light ratio ( $M_\star/L$ ), so that brighter galaxies usually present higher stellar mass-to-light ratios than fainter ones. Nevertheless, this ratio is dependent on diverse properties, such as colour, luminosity and observed wavelength (Bell & de Jong 2001; Kauffmann et al. 2003; Bell et al. 2003). Moreover, as previously discussed, the passive evolution that red galaxies undergo is not ac-

counted for in the determination of the absolute magnitude (eq. 53) and, thus, the IA luminosity dependence does not account for the difference in luminosity of similar stellar mass galaxies at different redshifts. As a consequence, even though stellar mass and luminosity are strongly correlated, there is still some scatter between both quantities, which justifies the analysis of the IA dependence with stellar mass, providing additional insight into the luminosity dependence.

The left-hand side of Fig. 10 shows the luminosity versus the stellar mass of the PAUS wide fields for red objects<sup>3</sup>, showing a clear relation between both quantities, albeit with some scatter. The dashed vertical lines indicate the stellar mass values used to define the equipopulated  $M_\star$  bins, while the horizontal dashed lines indicate the luminosity values that define the equipopulated luminosity bins. A general trend indicates that the luminosity increases with stellar mass, as expected. Nevertheless, the division we perform assigns different luminosity bins to a single  $M_\star$  bin and vice versa. Thus, if the IA alignment is driven by mass, a cleaner relation is expected when splitting by stellar mass, rather than by luminosity. We also include on the left-hand side of Fig. 10 the luminous and dense samples used in Fortuna et al. (2021b) for comparison with our samples, where the stellar mass estimates are extracted from Fortuna et al. (2025). These correspond to one of the faintest samples used to study IA in the literature so far, and we can see that PAUS enables us to even reach fainter and less massive objects. The right-hand side of Fig. 10 shows the evolution of IA as a function of stellar mass, where we observe that the IA amplitude for the red samples increases with mass. Conversely, in comparison with Fig. 9, the evolution as a function of stellar mass is more clear, as opposed to the luminosity division, where we saw a decrease in the IA amplitude for the intermediate luminosity bin. As for the blue objects, we are able to reach very

<sup>3</sup> The scatter for the case of blue objects is larger, as expected from spiral galaxies (Bell & de Jong 2001), but not shown here for conciseness, since the conclusions do not change.

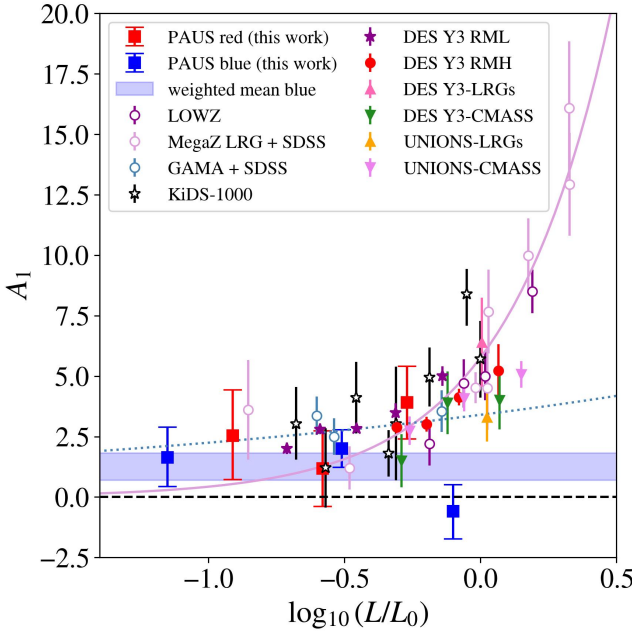


**Figure 9.** The dependence of  $A_1$  on luminosity for PAUS red and blue galaxies (red and blue squares, respectively). The shaded blue band shows the weighted mean of the blue fits, accompanied by its  $1\sigma$  uncertainty. Previous results from the literature are also shown: LOWZ (dark purple circles, Singh et al. 2015), MegaZ LRG+SDSS (light purple circles, Joachimi et al. 2011), GAMA+SDSS (blue circles, Johnston et al. 2019), KiDS-1000 (black stars, Fortuna et al. 2021b), DES Y3 RML (which stands for redMaGiC low- $z$ , purple stars, Samuroff et al. 2023), DES Y3 RMH (redMaGiC high- $z$ , red circles, Samuroff et al. 2023), and DES Y3-eBOSS LRGs (pink triangle up), DES Y3-CMASS (green triangle down), UNIONS-eBOSS LRGs (orange triangle up) and UNIONS-CMASS (violet triangle down) from Hervas Peters et al. (2024). The dotted blue line shows a power law from fitting the GAMA+SDSS results (low luminosity), while the solid purple line indicates a fit to the MegaZ LRG+SDSS results (high luminosity). Figure adapted and extended to include the PAUS measurements from Samuroff et al. (2023).

low-mass galaxies, down to  $\log_{10}(M_\star/M_\odot) \sim 9$ . As in Fig. 9, we include the weighted mean for blue galaxies as a shaded blue band, finding  $A_1 = 1.06^{+0.71}_{-0.71}$ , being consistent with 0 by less than  $2\sigma$ .

Most galaxies in our study fall within the luminosity range  $L_r < 3.2 \times 10^{10} L_\odot h^{-2}$  ( $\log_{10}(L/L_0) \lesssim -0.15$ ), which corresponds to the break in the double power law relation between IA and luminosity found by Fortuna et al. (2021b). Consequently, within this luminosity range, the relationship between luminosity and halo mass could be described by a single power law, as shown in Fig. 3 of Fortuna et al. (2025). However, due to the complex relationship between stellar mass, halo mass and luminosity, extrapolating our results to stellar mass at higher luminosities is not straightforward. To verify whether the observed trends hold for more luminous galaxies beyond  $L_r \sim 3.2 \times 10^{10} L_\odot h^{-2}$ , we incorporate the dense and luminous samples from Fortuna et al. (2021b), also shown on the right-hand side plot of Fig. 10. We then fit a power law between  $A_1$  and halo mass, using the  $A_1$  values from the Fortuna et al. (2021b) samples and the halo masses from Fortuna et al. (2025), such that:

$$A_1(M_h) = A_{M_h} \left( \frac{M_h}{M_{h,0}} \right)^{\beta_{M_h}}, \quad (55)$$

where  $M_h$  is the halo mass,  $M_{h,0} = 10^{13.2} h^{-1} M_\odot$  is the pivot

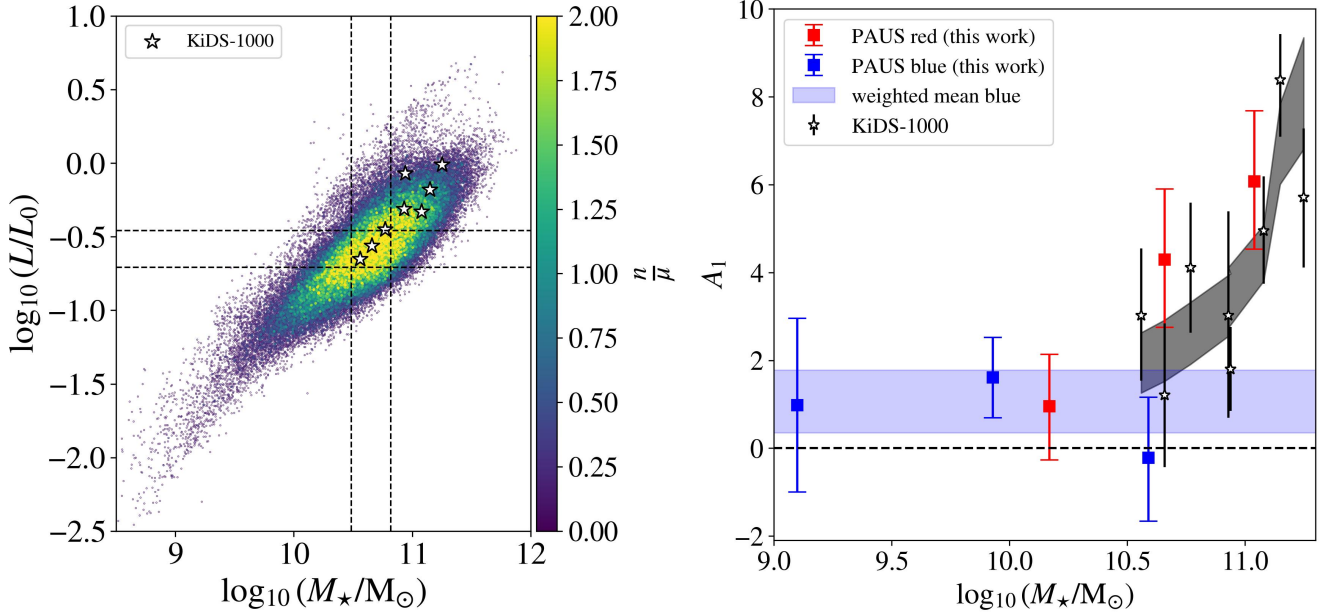
mass and we obtain  $A_{M_h} = 5.79^{+0.69}_{-0.69}$  and  $\beta_{M_h} = 0.65^{+0.20}_{-0.20}$ . Since Fortuna et al. (2025) provide a mapping between stellar mass and halo mass, we can express the power law in terms of stellar mass. This is shown in Fig. 10 as a black shaded area, encompassing the  $1\sigma$  uncertainty of the power law fit. Notably, this fit successfully describes the two most massive PAUS bins. Finally, we also compared our  $A_1$  fits as a function of stellar mass with the power law derived in Fortuna et al. (2025), which includes the samples from Fortuna et al. (2021b) but also from more massive objects (Singh et al. 2015; Joachimi et al. 2011; van Uitert & Joachimi 2017). In this case, the match with our fits is not that good, with the power law predicting less IA than our  $A_1$  fits. However, the range of masses used for that power law is quite broad and the error bars become very small, making the comparison more difficult when including less massive objects. We leave the derivation of halo masses for PAUS for future work, so that a more realistic comparison with the power law as a function of halo mass can be performed and we can reach the lowest stellar mass bin we defined.

### 5.3 Division by colour and redshift

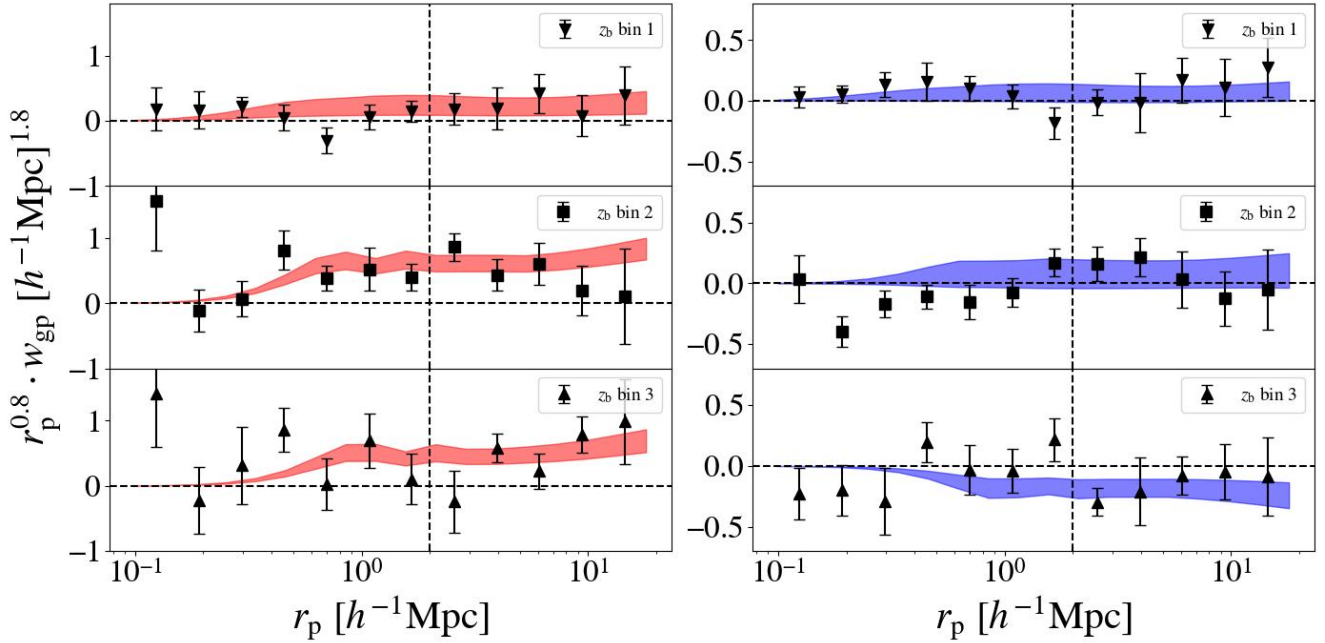
We now analyse the results obtained when splitting the samples by colour and redshift. We generate three equipopulated redshift bins, approximately covering the redshift range  $z_b \sim [0.1, 0.4]$ ,  $z_b \sim [0.4, 0.6]$  and  $z_b \sim [0.6, 1.0]$ , with means of  $z_b \sim 0.36(0.25)$ ,  $z_b \sim 0.55(0.46)$  and  $z_b \sim 0.75(0.73)$  for red (blue) galaxies. We refer to these redshift bins as  $z_b$  bin 1,  $z_b$  bin 2 and  $z_b$  bin 3, respectively.

Fig. 11 shows the  $w_{gp}$  measurements and modelling for red and blue objects for the different redshift bins. The distribution is the same as in Fig. 8. Even though not shown in the figure, a general trend indicating an increase of GC signal with redshift is observed. This behaviour is expected, since high-redshift samples tend to have higher GC than lower redshift samples for a fixed apparent magnitude, as the galaxies are intrinsically brighter at higher redshift, although this is partially counteracted by the passive evolution of galaxies. In the case of the IA measurements for red objects, the lower limits of the  $w_{gp}$  measurements for the lowest redshift bin are consistent with 0 in most of the  $r_p$  bins, in accordance to Table 2, with a subtle preference towards positive alignment for the central values of the measurements. For  $z_b$  bin 2 and  $z_b$  bin 3, there is a stronger positive alignment, which is similar between both redshift bins 2 and 3 for  $r_p > 2 h^{-1} \text{Mpc}$ . Nevertheless, for  $z_b$  bin 2, the values at scales lower than  $r_p = 2 h^{-1} \text{Mpc}$  are higher than for  $z_b$  bin 3, which explains the higher  $\chi^2_{\nu, \text{SNR}}$  seen in Table 2 for  $z_b$  bin 2. In the case of the blue samples, the  $w_{gp}$  measurement for the lowest redshift bin is consistent with 0 at all  $r_p$  separations. For  $z_b$  bin 2, the alignment is also consistent with 0 at  $r_p > 2 h^{-1} \text{Mpc}$ , but with higher variance than in the lower redshift bin case. Nevertheless, for  $r_p < 2 h^{-1} \text{Mpc}$ , there seems to be a consistent preference towards negative IA, although very weak, which may explain the high  $\chi^2_{\nu, \text{SNR}}$  observed in Table 2 for that case. Finally, for  $z_b$  bin 3, at  $r_p > 2 h^{-1} \text{Mpc}$  the signal slightly prefers negative IA, with the top error bars in most cases still being consistent with 0. In the case of the signal at  $r_p < 2 h^{-1} \text{Mpc}$ , the hint of negative alignment seen in the  $z_b$  bin 2 case is almost diluted.

The evolution of  $A_1$  as a function of redshift is shown in Fig. 12 for the PAUS red and blue objects (red and blue squares, respectively). In magnitude-limited samples, as it is the case for PAUS, low-redshift objects exhibit lower mean luminosities than high-redshift ones. As a result, it is not straightforward to determine whether the observed evolution of IA amplitudes across redshift-split subsets is driven by



**Figure 10.** (Left): Luminosity versus stellar mass coloured by the number of objects in each pixel normalised by the median value. (Right): The dependence of  $A_1$  as a function of stellar mass for PAUS red and blue galaxies (red and blue squares, respectively). The shaded blue band shows the weighted mean of the blue fits, accompanied by its  $1\sigma$  uncertainty. The black shading indicates the power law fit, with a  $1\sigma$  uncertainty, obtained from the values in [Fortuna et al. \(2021b\)](#), using the halo masses from [Fortuna et al. \(2025\)](#). In both plots, the stars indicate the points included in [Fortuna et al. \(2021b\)](#).



**Figure 11.** IA measurements in terms of  $w_{gp}$  for the three redshift bins, for red (left) and blue (right) objects. The shaded areas show the  $1\sigma$  uncertainty in the best fit using the non-linear galaxy bias and the NLA models. The dashed vertical lines show the minimum  $r_p$  used in the modelling.

differences in mean redshift or mean luminosity. Thus, if the luminosity is not accounted for when studying the evolution of IA with redshift, we expect lower IA amplitudes for low-redshift samples. One approach to deal with this is to define a subsample within a narrow luminosity range, to later split it in redshift bins. Nevertheless, this method reduces the overall number of objects analysed. Here, we opt to implement a different technique, which consists on multiplying

the  $A_1$  fits, obtained from the redshift bins defined in this section, by the inverse of the power law that describes the IA dependence with luminosity. With this approach, we take into account the different mean luminosities of each redshift bin and expect to remove, at first order, the luminosity dependence. Since the mean luminosities of the redshift bins we define are closer to the luminosity range covered by [Johnston et al. 2019](#), rather than that of [Joachimi et al. 2011](#), we use

the power law index from the former, with  $\alpha = 0.18$ . We consider that value when multiplying our  $A_1$  fits by the inverse of the power law, for both red and blue galaxies<sup>4</sup>, as it can be seen on the y-label of Fig. 12. After accounting for the luminosity variation, we do not find a clear dependence of IA with redshift, although it is true that we find more alignment for the two higher redshift bins in red galaxies. Nevertheless, the weighted mean of the  $A_1$  fits from red objects, depicted as a red shaded band with its  $1\sigma$  uncertainty, shows that our fits are well described by a constant value of  $A_1(L/L_0)^{-0.18} = 5.56^{+0.89}_{-0.89}$  by less than  $2\sigma$ . A similar trend is observed for blue galaxies, where we find an IA signal consistent with 0, as indicated by the blue shaded band, with  $A_1(L/L_0)^{-0.18} = 0.12^{+0.67}_{-0.67}$ . Together with the PAUS results, we include fits from the literature coming from Johnston et al. 2019 (Samples G:  $z < 0.26$  red and blue from Table B.1) and Fortuna et al. 2021b (Samples Z1 and Z2 from Table 1), which are in agreement with the shaded bands derived for the PAUS red objects, and lie in a similar luminosity range, so that we employ  $\alpha = 0.18$  when multiplying by the inverse of the luminosity power law. We also include the fits from Samuroff et al. 2023 (DES Y3 RML, DES Y3 RMH, DES Y3-CMASS and DES Y3-LRGs from Fig. E1), which are in general consistent with the fits from Johnston et al. 2019 and Fortuna et al. 2021b, but not necessarily with the red shaded band. These discrepancies likely arise from differences in the red galaxy classification, with respect to PAUS, of both redMaGiC (Rozo et al. 2016) and CMASS (Reid et al. 2016), especially in the latter, which includes bluer and fainter objects than redMaGiC. Also, as discussed in Section 5.2, the error bars from the Samuroff et al. 2023 fits are underestimated, so we would expect a better agreement with the red shaded band derived from PAUS if the error bars were revised. The luminosity range of these Samuroff et al. 2023 fits is diverse and we either employ  $\alpha = 0.18$  or  $\alpha = 1.13$  (the power law index derived from Joachimi et al. 2011) depending on the luminosity value of each sample. Finally, we include the results from MegaZ LRG+SDSS (Joachimi et al. 2011, Table 3) and LOWZ (Singh et al. 2015, Table 2), which are in agreement with the red shaded band from the PAUS results and which correspond to high-luminosity samples, for which we consider  $\alpha = 1.13$  when accounting for the IA luminosity evolution.

Table 3 summarises the  $A_1$ ,  $b_1$ <sup>5</sup> and  $\chi^2_{\nu, \text{fit}, \text{SVD}}$  (eq. 51) for the different scenarios studied, where  $\chi^2_{\nu, \text{fit}, \text{SVD}}$  is obtained from the joint fit of  $w_{\text{gg}}$  and  $w_{\text{gp}}$ . Note that the  $\chi^2_{\nu, \text{fit}, \text{SVD}}$  varies from values below and above 1, with 1 being the expected value for a  $\chi^2_{\nu}$  if the fit of a data vector to a model is correctly performed. Nevertheless, checking the  $\chi^2_{\nu}$  values from previous literature analyses, such as the ones included in Fig. 9 and Fig. 12, we find  $\chi^2_{\nu, \text{fit}, \text{SVD}}$  values within the range of these previous studies. We also find similar values of  $\chi^2_{\nu, \text{fit}, \text{SVD}}$  for the MICE fits, indicating that it is unlikely that there is a problem with the PAUS data when performing the fits. An explanation on why  $\chi^2_{\nu}$  values below and above 1 may be acceptable can be found in Andrae et al. (2010), where they analyse the effect of priors and non-linear models on the computation of  $\chi^2_{\nu}$  and on the number of degrees of freedom. Also, in some cases, the  $\chi^2_{\nu, \text{fit}, \text{SVD}} > 1$  since there is some noise and outlier points in the measurements that increase the values. Finally, in general, the  $\chi^2_{\nu, \text{fit}, \text{SVD}}$  values for

<sup>4</sup> For blue galaxies, we do not expect the same evolution of  $A_1$  with luminosity as for red galaxies. However, to homogenise the comparison, we also multiply by the inverse power law the  $A_1$  values from blue galaxies.

<sup>5</sup> The  $b_2$  values are consistent with 0 for all cases and are not shown in the Table.

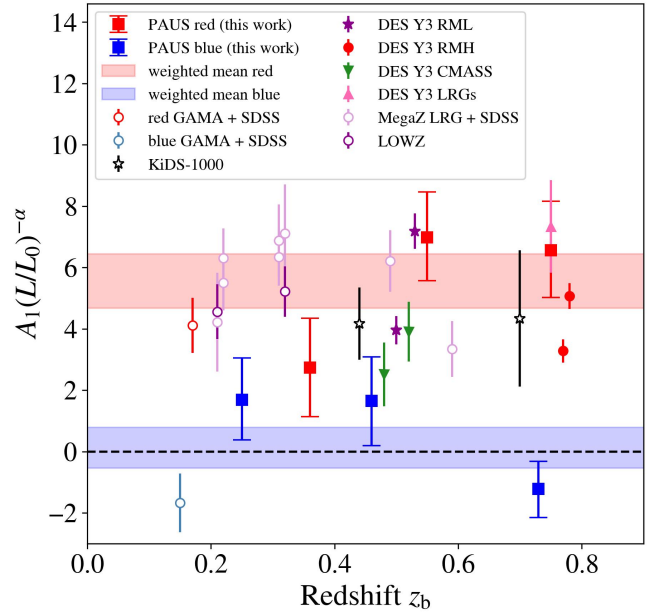


**Figure 12.** The dependence of  $A_1$  on redshift for PAUS red and blue galaxies (red and blue squares, respectively), after accounting for the luminosity evolution across redshift bins. The shaded red and blue bands show the weighted mean of the  $A_1$  fits for red and blue objects, respectively, including their  $1\sigma$  error. Previous results from the literature are also shown: GAMA+SDSS (red and blue circles, Johnston et al. 2019), KiDS-1000 (black stars, Fortuna et al. 2021b), DES Y3 RML (purple stars), DES Y3 RMH (red circles), DES Y3-CMASS (green triangle down) and DES Y3-LRGs (pink triangle up) from Samuroff et al. 2023, MegaZ LRG+SDSS (pink circles, Joachimi et al. 2011) and LOWZ (violet circles, Singh et al. 2015). The power law index  $\alpha$  depends on the luminosity of a given sample. For PAUS, GAMA+SDSS and KiDS-1000,  $\alpha = 0.18$ ; for DES Y3 RML, DES Y3 RMH and DES Y3-CMASS,  $\alpha$  is either 0.18 or 1.13; and for DES Y3-LRGs, MegaZ LRG+SDSS and LOWZ,  $\alpha = 1.13$ .

blue galaxies are  $\chi^2_{\nu, \text{fit}, \text{SVD}} < 1$  since the IA signal is close to 0, so that the signal is easier to model.

## 6 CONCLUSIONS

The intrinsic alignments (IA) of galaxies remain a major systematic in the era of precision cosmology, mimicking the weak gravitational lensing signal and biasing cosmological analyses. Therefore, it is of utmost importance to characterise IA for different kinds of galaxy populations, in order to be able to correct for them.

In this paper, we measure the photometric GC and IA signals from the PAUS wide fields in the redshift range  $0.1 < z_b < 1.0$ , down to  $i_{\text{AB}} < 22$ , and approximately covering  $\sim 400000$  objects with galaxy shapes. We analyse the GC and IA by performing sample divisions based on colour, luminosity, stellar mass and redshift.

The GC and IA signals are measured by projecting 3-dimensional correlation functions, employing the PAUS photo- $z$  estimated in Navarro-Gironés et al. (2024) and the galaxy shapes extracted from the KiDS and CFHTLenS external catalogues, and calibrated to account for the PSF and the multiplicative bias. The colour separation between red (passive) and blue (active) galaxies is defined by combining a  $\text{NUV}rK$  diagram, which traces the sSFR and dust attenuation, and a spectral type parameter from the KiDS and CFHTLenS catalogues.

**Table 3.**  $A_1$ ,  $b_1$  and  $\chi^2_{\nu, \text{fit}, \text{SVD}}$  for red and blue galaxies for the IA cases studied in this paper.

Sample	$A_1$ red	$A_1$ blue	$b_1$ red	$b_1$ blue	$\chi^2_{\nu, \text{fit}, \text{SVD}}$ red	$\chi^2_{\nu, \text{fit}, \text{SVD}}$ blue
All	$2.78^{+0.83}_{-0.82}$	$0.68^{+0.53}_{-0.51}$	$1.14^{+0.05}_{-0.07}$	$1.13^{+0.05}_{-0.06}$	0.30	0.25
Lum. bin 1	$2.54^{+1.90}_{-1.82}$	$1.64^{+1.24}_{-1.21}$	$1.00^{+0.08}_{-0.10}$	$1.01^{+0.08}_{-0.10}$	1.05	1.03
Lum. bin 2	$1.18^{+1.55}_{-1.57}$	$2.00^{+0.78}_{-0.78}$	$1.27^{+0.08}_{-0.09}$	$1.28^{+0.05}_{-0.06}$	3.44	0.31
Lum. bin 3	$3.91^{+1.50}_{-1.50}$	$-0.59^{+1.10}_{-1.14}$	$1.28^{+0.05}_{-0.06}$	$1.33^{+0.05}_{-0.06}$	3.01	0.14
$M_{\star}$ bin 1	$0.95^{+1.19}_{-1.21}$	$0.98^{+1.98}_{-1.98}$	$1.12^{+0.05}_{-0.07}$	$0.85^{+0.12}_{-0.17}$	0.29	1.00
$M_{\star}$ bin 2	$4.30^{+1.61}_{-1.55}$	$1.61^{+0.91}_{-0.91}$	$1.43^{+0.06}_{-0.07}$	$1.26^{+0.05}_{-0.06}$	0.82	0.39
$M_{\star}$ bin 3	$6.07^{+1.61}_{-1.54}$	$-0.22^{+1.38}_{-1.44}$	$1.78^{+0.07}_{-0.08}$	$1.46^{+0.06}_{-0.06}$	0.28	0.26
$z$ bin 1	$2.04^{+1.20}_{-1.20}$	$1.09^{+0.88}_{-0.84}$	$1.01^{+0.08}_{-0.10}$	$0.97^{+0.10}_{-0.13}$	0.30	0.54
$z$ bin 2	$5.47^{+1.16}_{-1.10}$	$1.35^{+1.16}_{-1.19}$	$1.17^{+0.10}_{-0.12}$	$1.14^{+0.08}_{-0.10}$	1.61	0.74
$z$ bin 3	$5.38^{+1.31}_{-1.26}$	$-1.11^{+0.82}_{-0.86}$	$1.38^{+0.08}_{-0.08}$	$1.39^{+0.08}_{-0.09}$	1.96	0.77

We model the GC and IA signals in order to obtain constraints on the galaxy bias and IA parameters. For that, we use correlation functions that account for signal dilution due to the lower precision of photo- $z$ , while also incorporating contaminant terms from magnification and shear.

We include consistency tests to ensure that both our measurements and constraints are robust. For this purpose, we employ the MICE simulation, generating a galaxy mock that both resembles the galaxy populations obtained in PAUS and reproduces the PAUS-like photo- $z$ . The consistency tests involve validating the random catalogues used in the measurements, checking that the use of photo- $z$ , instead of spec- $z$ , does not bias our constraints, and assessing that the error estimation in our PAUS measurements is robust.

The analysis is performed for three scenarios. First, for a colour-based division analysis, we measure IA for red galaxies and find IA amplitudes consistent with  $A_1 = 2.78^{+0.83}_{-0.82}$ , while, for blue galaxies, we observe a null IA signal, with  $A_1 = 0.68^{+0.53}_{-0.51}$ .

Second, besides the colour split, we bin by luminosity and stellar mass, defining three equipopulated regions in both parameters. Our results extend the  $A_1$  dependence towards lower luminosities and lower mass objects, with respect to the literature, while still being consistent with previous work at higher luminosities and masses. For the case of the luminosity dependence, for red galaxies, there is an overall trend of IA increase with it, although there is a decrease of IA amplitude in the intermediate luminosity bin. For the case of the stellar mass dependence, for red galaxies, we see a clearer increase of IA with mass. For blue galaxies, IA are consistent with 0 for both luminosity and stellar mass dependence.

Finally, in addition to the colour-based division, we split the sample into three equipopulated redshift bins. Red galaxies show slight alignment in the lowest redshift bin, while the intermediate and highest redshift bins yield a similar IA amplitude of  $A_1 \sim 5$ . However, variations in IA with redshift are affected by differences in the luminosity distributions across redshift bins, which we try to correct by applying a luminosity-dependent scaling to the IA fits, based on the inverse of the assumed power law relation. After applying this correction, the dependence with redshift for red objects is compatible with a constant value. For blue galaxies, measurements generally show no signal.

The results presented in this work help constrain an unexplored regime dominated by low-luminosity and low-mass galaxies. As upcoming stage-IV surveys will observe fainter and less massive galaxies than stage-III surveys, it is essential to accurately constrain IA for these relevant galaxy populations. PAUS enables this by providing informative IA priors, ensuring unbiased cosmological analyses.

## ACKNOWLEDGEMENTS

The authors would like to thank Benjamin Camacho, Fabian Hervas Peters, Harry Johnston, Simon Samuroff, Kai Hoffmann, Jonathan Blazek, Elizabeth Gonzalez, Diego García Lambas and Martin Kilbinger for useful conversations about this project.

DNG, MC and EG acknowledge support from the Spanish Ministerio de Ciencia e Innovacion (MICINN), project PID2021-128989NB. DNG and H. Hoekstra acknowledge support from the European Research Council (ERC) under the European Union's Horizon 2020 research and innovation program with Grant agreement No. 101053992. MS acknowledges support by the State Research Agency of the Spanish Ministry of Science and Innovation under the grants 'Galaxy Evolution with Artificial Intelligence' (PGC2018-100852-A-I00) and 'BASALT' (PID2021-126838NB-I00) and the Polish National Agency for Academic Exchange (Bekker grant BPN/BEK/2021/1/00298/DEC/1). This work was partially supported by the European Union's Horizon 2020 Research and Innovation program under the Maria Skłodowska-Curie grant agreement (No. 754510). H. Hildebrandt is supported by a DFG Heisenberg grant (Hi 1495/5-1), the DFG Collaborative Research Center SFB1491, an ERC Consolidator Grant (No. 770935), and the DLR project 50QE2305. BJ acknowledges support by the ERC-selected UKRI Frontier Research Grant EP/Y03015X/1. ME acknowledges funding by MCIN with funding from European Union NextGenerationEU (PRTR-C17.II) and by Generalitat de Catalunya. JC acknowledges support from the grant PID2021-123012NA-C44 funded by MCIN/AEI/ 10.13039/501100011033 and by "ERDF A way of making Europe". FJC acknowledges support from the Spanish Plan Nacional project PID2022-141079NB-C31. CP acknowledges support from the Spanish Plan Nacional project PID2022-141079NB-C32. PR acknowledges the support by the Tsinghua Shui Mu Scholarship, the funding of the National Key R&D Program of China (grant no. 2023YFA1605600), the science research grants from the China Manned Space Project with No. CMS-CSST2021-A05 and the Tsinghua University Initiative Scientific Research Program (No. 20223080023). The PAU Survey is partially supported by MINECO under grants CSD2007-00060, AYA2015-71825, ESP2017-89838, PGC2018-094773, PGC2018-102021, PID2019-111317GB, SEV-2016-0588, SEV-2016-0597, MDM-2015-0509 and Juan de la Cierva fellowship and LACEGAL and EWC Marie Skłodowska-Curie grant No 101086388 and no.776247 with ERDF funds from the EU Horizon 2020 Programme, some of which include ERDF funds from the European Union. IEEC and IFAE are partially funded by the CERCA and Beatriu de Pinos program of the Generalitat de Catalunya. Funding for PAUS has also been provided by Durham

University (via the ERC StG DEGAS-259586), ETH Zurich, Leiden University (via ERC StG ADULT-279396 and Netherlands Organisation for Scientific Research (NWO) Vici grant 639.043.512), University College London and from the European Union's Horizon 2020 research and innovation programme under the grant agreement No 776247 EWC. The PAU data center is hosted by the Port d'Informatió Científica (PIC), maintained through a collaboration of CIEMAT and IFAE, with additional support from Universitat Autònoma de Barcelona and ERDF. The authors acknowledge the PIC services department team for their support and fruitful discussions.

## DATA AVAILABILITY

The PAUS wide field catalogue can be accessed via [CosmoHub](#) (Tallada et al. 2020; Carretero et al. 2017), through this link: <https://cosmohub.pic.es/catalogs/319>. Access to the PAUS public data, including the raw and the reduced images, can be found at <https://pausurvey.org/public-data-release/>. The authors will share other data products, such as correlation functions or GC and IA parameter constraints, upon reasonable requests.

## REFERENCES

Ahumada R., et al., 2020, *ApJS*, 249, 3

Aihara H., et al., 2018, *PASJ*, 70, S4

Alarcon A., et al., 2021, *MNRAS*, 501, 6103

Andrae R., Schulze-Hartung T., Melchior P., 2010, Dos and don'ts of reduced chi-squared ([arXiv:1012.3754](https://arxiv.org/abs/1012.3754)), <https://arxiv.org/abs/1012.3754>

Arnouts S., et al., 2013, *A&A*, 558, A67

Bakx T., Kurita T., Chisari N. E., Vlah Z., Schmidt F., 2023, *JCAP*, 2023, 005

Baldauf T., Smith R. E., Seljak U. c. v., Mandelbaum R., 2010, *Phys. Rev. D*, 81, 063531

Bartelmann M., Schneider P., 2001, *Physics Reports*, 340, 291

Bate J., Chisari N. E., Codis S., Martin G., Dubois Y., Devriendt J., Pichon C., Slyz A., 2020, *MNRAS*, 491, 4057

Behroozi P. S., Wechsler R. H., Conroy C., 2013, *ApJ*, 770, 57

Bell E. F., de Jong R. S., 2001, *ApJ*, 550, 212

Bell E. F., McIntosh D. H., Katz N., Weinberg M. D., 2003, *ApJS*, 149, 289

Benítez N., 2000, *ApJ*, 536, 571

Benítez N., et al., 2009, *ApJ*, 691, 241

Blazek J. A., MacCrann N., Troxel M. A., Fang X., 2019, *Phys. Rev. D*, 100, 103506

Bonoli S., et al., 2021, *A&A*, 653, A31

Boquien M., Burgarella, D. Roehlly, Y. Buat, V. Ciesla, L. Corre, D. Inoue, A. K. Salas, H. 2019, *A&A*, 622, A103

Bridle S., King L., 2007, *New Journal of Physics*, 9, 444

Brown M. L., Taylor A. N., Hambly N. C., Dye S., 2002, *MNRAS*, 333, 501

Buat V., et al., 2021, *A&A*, 654, A93

Cabayol L., et al., 2023, *A&A*, 671, A153

Carretero J., Castander F. J., Gaztañaga E., Crocce M., Fosalba P., 2014, *MNRAS*, 447, 646

Carretero J., et al., 2017, in Proceedings of the European Physical Society Conference on High Energy Physics. 5-12 July. p. 488

Castander F. J., et al., 2024, *MNRAS*, 531, 5067

Catelan P., Kamionkowski M., Blandford R. D., 2001, *MNRAS*, 320, L7

Chisari N., et al., 2015, *MNRAS*, 454, 2736

Chisari N. E., et al., 2019, *ApJS*, 242, 2

Codis S., et al., 2015, *MNRAS*, 448, 3391

Cole S., 2011, *MNRAS*, 416, 739

Conroy C., Wechsler R. H., Kravtsov A. V., 2006, *ApJ*, 647, 201

Conselice C. J., 2014, *ARA&A*, 52, 291

Crocce M., Castander F. J., Gaztañaga E., Fosalba P., Carretero J., 2015, *MNRAS*, 453, 1513

Csizi B., et al., 2024, *A&A*, 689, A37

Cuillandre J.-C. J., et al., 2012, in Peck A. B., Seaman R. L., Comeron F., eds, Society of Photo-Optical Instrumentation Engineers (SPIE) Conference Series Vol. 8448, Observatory Operations: Strategies, Processes, and Systems IV. p. 84480M, doi:10.1117/12.925584

Dark Energy Survey Collaboration et al., 2016, *MNRAS*, 460, 1270

Davidzon I., et al., 2016, *A&A*, 586, A23

Davis M., et al., 2003, in Guhathakurta P., ed., Vol. 4834, Discoveries and Research Prospects from 6- to 10-Meter-Class Telescopes II. SPIE, pp 161 – 172, doi:10.1117/12.457897, <https://doi.org/10.1117/12.457897>

Daza-Perilla I. V., et al., 2025, *A&A*, 693, A102

Dekel A., Lahav O., 1999, *ApJ*, 520, 24

Erben T., et al., 2013, *MNRAS*, 433, 2545

Eriksen M., et al., 2019, *MNRAS*, 484, 4200

Eriksen M., et al., 2020, *MNRAS*, 497, 4565

Euclid Collaboration: Castander et al., 2024, Euclid. V. The Flagship galaxy mock catalogue: a comprehensive simulation for the Euclid mission (arXiv:2405.13495)

Euclid Collaboration: Mellier et al., 2024, arXiv e-prints, p. arXiv:2405.13491

Fang X., Blazek J. A., McEwen J. E., Hirata C. M., 2017, *JCAP*, 2017, 030

Farrow D. J., Cole S., Norberg P., Metcalfe N., Baldry I., et al., 2015, *MNRAS*, 454, 2120

Foreman-Mackey D., Hogg D. W., Lang D., Goodman J., 2013, *PASP*, 125, 306

Fortuna M. C., Hoekstra H., Joachimi B., Johnston H., Chisari N. E., Georgiou C., Mahony C., 2021a, *MNRAS*, 501, 2983

Fortuna M. C., Hoekstra, Henk Johnston, Harry Vakili, Mohammadjavad Kannawadi, Arun et al., 2021b, *Astronomy and Astrophysics*, 654, A76

Fortuna M. C., et al., 2025, *A&A*, 694, A322

Fosalba P., Gaztañaga E., Castander F. J., Crocce M., 2014, *MNRAS*, 447, 1319

Fosalba P., Crocce M., Gaztañaga E., Castander F. J., 2015, *MNRAS*, 448, 2987

Gaztañaga E., Scoccimarro R., 2005, *MNRAS*, 361, 824

Georgiou C., Johnston H., Hoekstra H., Viola M., Kuijken K., et al., 2019, *Astronomy and Astrophysics*, 622, A90

Georgiou C., Chisari N. E., Bilicki M., La Barbera F., Napolitano N. R., Roy N., Tortora C., 2025, arXiv e-prints, p. arXiv:2502.09452

Gonzalez E. J., et al., 2023, *MNRAS*, 522, 5655

Goodman J., Weare J., 2010, *Communications in Applied Mathematics and Computational Science*, 5, 65

Griffith R. L., et al., 2012, *ApJS*, 200, 9

Hambly N., Irwin M., MacGillivray H., 2001, *MNRAS*, 326, 1295

Hervas Peters F., et al., 2024, arXiv e-prints, p. arXiv:2412.01790

Heymans C., et al., 2006, *MNRAS*, 368, 1323

Heymans C., et al., 2012, *MNRAS*, 427, 146

Hilbert S., Xu D., Schneider P., Springel V., Vogelsberger M., Hernquist L., 2017, *MNRAS*, 468, 790

Hildebrandt H., et al., 2012, *MNRAS*, 421, 2355

Hildebrandt H., et al., 2021, *A&A*, 647, A124

Hirata C. M., Seljak U. c. v., 2004, *Phys. Rev. D*, 70, 063526

Hirata C. M., Mandelbaum R., Ishak M., Seljak U., Nichol R., et al., 2007, *MNRAS*, 381, 1197

Hoekstra H., Franx M., Kuijken K., Squires G., 1998, *ApJ*, 504, 636

Hoekstra H., Franx M., Kuijken K., 2000, *ApJ*, 532, 88

Hoekstra H., Herbonnet R., Muzzin A., Babul A., Mahdavi A., Viola M., Cacciato M., 2015, *MNRAS*, 449, 685

Hoffmann K., Bel J., Gaztañaga E., Crocce M., Fosalba P., Castander F. J., 2014, *MNRAS*, 447, 1724

Hoffmann K., et al., 2022, *Phys. Rev. D*, 106, 123510

Hopkins A. M., et al., 2013, *MNRAS*, 430, 2047

Ivezić Ž., et al., 2019, *ApJ*, 873, 111

Jarvis M., Bernstein G., Jain B., 2004, *MNRAS*, 352, 338

Jing Y. P., Mo H. J., Börner G., 1998, *ApJ*, 494, 1

Joachimi B., Bridle S. L., 2010, *Astronomy and Astrophysics*, 523, A1

Joachimi B., Mandelbaum R., Abdalla F. B., Bridle S. L., 2011, *Astronomy and Astrophysics*, **527**, A26

Joachimi B., Semboloni E., Hilbert S., Bett P. E., Hartlap J., et al., 2013, *MNRAS*, **436**, 819

Joachimi B., et al., 2015, *Space Sci. Rev.*, **193**, 1

Johnston H., Georgiou C., Joachimi B., Hoekstra H., Chisari N. E., et al., 2019, *Astronomy and Astrophysics*, **624**, A30

Johnston H., et al., 2021a, *A&A*, **646**, A147

Johnston H., et al., 2021b, *A&A*, **648**, A98

Kaiser N., 1984, *ApJ*, **284**, L9

Kaiser N., Squires G., Broadhurst T., 1995, *ApJ*, **449**, 460

Kauffmann G., et al., 2003, *MNRAS*, **341**, 33

Kilbinger M., 2015, *Reports on Progress in Physics*, **78**, 086901

Krause E., et al., 2021, *arXiv e-prints*, p. arXiv:2105.13548

Kuijken K., et al., 2019, *A&A*, **625**, A2

Laigle C., et al., 2016, *ApJS*, **224**, 24

Lamman C., Tsaprazi E., Shi J., Šarčević N. N., Pyne S., Legnani E., Ferreira T., 2024, *The Open Journal of Astrophysics*, **7**, 14

Landy S. D., Szalay A. S., 1993, *ApJ*, **412**, 64

Lange J. U., 2023, *MNRAS*, **525**, 3181

Lewis A., Challinor A., Lasenby A., 2000, *ApJ*, **538**, 473

Limber D. N., 1953, *ApJ*, **117**, 134

Luppino G. A., Kaiser N., 1997, *ApJ*, **475**, 20

Maion F., Angulo R. E., Bakx T., Chisari N. E., Kurita T., Pellejero-Ibáñez M., 2024, *MNRAS*, **531**, 2684

Mandelbaum R., 2018, *ARA&A*, **56**, 393

Mandelbaum R., Hirata C. M., Ishak M., Seljak U., Brinkmann J., 2006, *MNRAS*, **367**, 611

Mandelbaum R., et al., 2010, *MNRAS*, **410**, 844

Masoura V. A., Mountrichas G., Georgantopoulos I., Ruiz A., Magdis G., Plionis M., 2018, *A&A*, **618**, A31

McDonald P., 2006, *Phys. Rev. D*, **74**, 103512

McEwen J. E., Fang X., Hirata C. M., Blazek J. A., 2016, *JCAP*, **2016**, 015

Moles M., et al., 2008, *AJ*, **136**, 1325

Moster B. P., Naab T., White S. D. M., 2013, *MNRAS*, **428**, 3121

Navarro-Gironés D., et al., 2024, *MNRAS*, **534**, 1504

Norberg P., Baugh C. M., Gaztañaga E., Croton D. J., 2009, *MNRAS*, **396**, 19

Okumura T., Jing Y. P., Li C., 2009, *The Astrophysical Journal*, **694**, 214

Padilla C., et al., 2019, *AJ*, **157**, 246

Pandey S., et al., 2020, *Phys. Rev. D*, **102**, 123522

Park C., Choi Y.-Y., 2005, *ApJ*, **635**, L29

Piras D., Joachimi B., Schäfer B. M., Bonamigo M., Hilbert S., van Uitert E., 2017, *MNRAS*, **474**, 1165

Poggianti B. M., 1997, *A&AS*, **122**, 399

Reid B., et al., 2016, *MNRAS*, **455**, 1553

Renard P., et al., 2020, *MNRAS*, **501**, 3883

Renard P., et al., 2022, *MNRAS*, **515**, 146

Rozo E., et al., 2016, *MNRAS*, **461**, 1431

Saito S., Baldau T., Vlah Z., Seljak U. c. v., Okumura T., McDonald P., 2014, *Phys. Rev. D*, **90**, 123522

Salim S., et al., 2005, *The Astrophysical Journal*, **619**, L39

Samuroff S., Mandelbaum R., Blazek J., 2021, *MNRAS*, **508**, 637

Samuroff S., et al., 2023, *MNRAS*, **524**, 2195

Schneider M. D., Bridle S., 2010, *MNRAS*, **402**, 2127

Scoccimarro R., Sheth R. K., Hui L., Jain B., 2001, *ApJ*, **546**, 20

Scodellato M., et al., 2018, *Astronomy and Astrophysics*, **609**

Scoville N., et al., 2007, *ApJS*, **172**, 38

Seljak U., 2000, *MNRAS*, **318**, 203

Serrano S., et al., 2023, *MNRAS*, **523**, 3287

Shi J., Kurita T., Takada M., Osato K., Kobayashi Y., Nishimichi T., 2021, *JCAP*, **2021**, 030

Singh S., Mandelbaum R., 2016, *MNRAS*, **457**, 2301

Singh S., Mandelbaum R., More S., 2015, *MNRAS*, **450**, 2195

Siudek M., et al., 2022, *A&A*, **666**, A131

Smit M., Kuijken K., 2018, *A&A*, **609**, A103

Soo J. Y. H., et al., 2021, *MNRAS*, **503**, 4118

Spergel D., et al., 2015, *arXiv e-prints*, p. arXiv:1503.03757

Springel V., 2005, *MNRAS*, **364**, 1105

Strateva I., et al., 2001, *AJ*, **122**, 1861

Takahashi R., Sato M., Nishimichi T., Taruya A., Oguri M., 2012, *ApJ*, **761**, 152

Tallada P., et al., 2020, *Astronomy and Computing*, **32**, 100391

Tonello N., et al., 2019, *Astronomy and Computing*, **27**, 171

Tortorelli L., et al., 2021, *JCAP*, **2021**, 013

Trujillo-Gomez S., Klypin A., Primack J., Romanowsky A. J., 2011, *ApJ*, **742**, 16

Vale A., Ostriker J. P., 2004, *MNRAS*, **353**, 189

Vlah Z., Chisari N. E., Schmidt F., 2020, *JCAP*, **2020**, 025

Vlah Z., Chisari N. E., Schmidt F., 2021, *JCAP*, **2021**, 061

Williams R. J., Quadri R. F., Franx M., van Dokkum P., Labb   I., 2009, *ApJ*, **691**, 1879

Wright A. H., et al., 2024, *A&A*, **686**, A170

Xia Q., Kang X., Wang P., Luo Y., Yang X., Jing Y., Wang H., Mo H., 2017, *ApJ*, **848**, 22

York D. G., et al., 2000, *AJ*, **120**, 1579

Zheng Z.-Y., et al., 2017, *ApJ*, **842**, L22

Zhou C., Tong A., Troxel M. A., Blazek J., Lin C., et al., 2023, *MNRAS*, **526**, 323

de Jong J. T., Kleijn G. A. V., Kuijken K. H., Valentijn E. A., 2013, *Experimental Astronomy*, **35**, 25

van Uitert E., Joachimi B., 2017, *MNRAS*, **468**, 4502

## APPENDIX A: COMPARISON OF THE $A_1$ FITS FOR THE BRIGHTER AND FAINTER SAMPLES

Here, we include a comparison of the  $A_1$  amplitudes obtained for both the brighter (W1+G09+W3 fields with  $i_{AB} < 22$ , squares) and the fainter (W1+W3 fields with  $i_{AB} < 22.5$ , diamonds) samples analysed in this paper. This can be seen in Fig. A1 for the division in galaxy colour (top left), galaxy colour and redshift (top right), galaxy colour and luminosity (bottom left) and galaxy colour and stellar mass (bottom right). We note that the mean redshift, luminosity and stellar mass values for the brighter and fainter samples are virtually the same, since the brighter sample is the one that we divide in equipopulated bins to define the range limits. Thus, to avoid overlapping, we apply a small shift in the mean redshift, luminosity or stellar mass values when plotting the  $A_1$  values.

For the case of the separation by galaxy colour, the IA amplitudes for both brighter and fainter samples are consistent with one another, with a slight decrease of the amplitude for the fainter sample. This is an indication that the IA is quite stable when going from  $i_{AB} < 22$  to  $i_{AB} < 22.5$  when only splitting by colour. It also implies that the combination of fields is done in a robust way since, if we exclude the G09 field from the analysis, as it is the case for the fainter sample, the results remain almost unaltered. Thus, the alignment in all the three fields is equivalent, as expected for similar galaxy populations.

For the case of the separation by galaxy colour and redshift, the  $A_1$  amplitudes for the brighter and fainter samples are consistent with one another for red galaxies, where we observe that, although the mean of the fit is higher for the brighter samples, the constraints are between errors. For the case of blue galaxies, this is also the case, with the  $A_1$  amplitude consistent between brighter and fainter samples and with 0 in all cases.

The evolution of  $A_1$  as a function of galaxy colour and luminosity indicates that, in all cases, the amplitudes from both brighter and fainter samples are consistent with one another, although their central values do not agree. We note that the decrease in the  $A_1$  amplitude for the intermediate luminosity bin in the red brighter sample, seen in Section 5.2, is not observed for the fainter sample, which shows a more clear evolution with luminosity. For the case of the  $A_1$  evolution

with galaxy colour and stellar mass, we also find consistent values for the brighter and fainter samples.

## APPENDIX B: ALTERNATIVE COLOUR CLASSIFICATIONS

Here, we compare the red and blue galaxy classification used in this work with alternative approaches from the literature. Fig. B1 shows the red and blue populations, defined by the  $NUVrK$  colour split and the  $T_{BPZ}$  parameter employed in this work (see Section 2.4), displayed in the colour-magnitude diagrams  $g - r$  vs.  $r$  (left) and  $u - i$  vs.  $i$  (right), where  $g, r$  and  $i$  correspond to rest-frame absolute magnitudes  $k$ -corrected to  $z = 0$ . In the left plot, we show as a dashed line the separation employed by the GAMA+SDSS (Johnston et al. 2019) analysis, where red galaxies are defined as those with  $g - r > 0.66$ . A dotted line shows the separation used in KiDS-1000 (Georgiou et al. 2019), with  $g - r > 0.14 - 0.026r$ . In the right plot, we show the cut adopted in the previous PAUS IA analysis, where they defined a cut of  $u - i > 1.138 - 0.038i$ .

Visual inspection reveals that most galaxies defined as red in this work are also classified as red by the literature. However, there is a larger mismatch for the classification of blue galaxies, with a substantial fraction of galaxies classified as blue by our colour split but considered red by the literature, especially for the previous PAUS analysis. As a result, our colour classification returns a higher percentage of blue galaxies ( $\sim 79\%$ ), compared to the cuts employed in the literature, which yield  $\sim 61\%$  (GAMA+SDSS),  $\sim 64\%$  (KiDS-1000) and  $\sim 34\%$  (previous PAUS analysis) of blue galaxies. The fact that we still observe a null IA signal in our blue sample suggests that some galaxies classified as red by the literature may belong to the blue population, potentially lowering the observed IA signal in their red samples.

Table B1 quantifies the agreement between the classification used in this work and the colour-magnitude classifications from GAMA+SDSS (left table, named J2019), KiDS-1000 (centre table, named G2025) and by the previous PAUS IA analysis (right, named J2021). We note that the sum of rows and columns, which corresponds to the number of red or blue galaxies obtained from the colour split from a given survey, does not coincide across tables. This discrepancy arises because some galaxies lack flux measurement in certain bands and are therefore discarded when performing the colour cut.

## APPENDIX C: RANDOMS

When measuring GC and IA from eq. 14 and 15, we need a set of random catalogues to help us define the mean density of galaxies. Building these random catalogues is not a trivial exercise, since we want to obtain catalogues where the GC is null but that, at the same time, follow the number count distribution as a function of redshift.

Since in this paper we study projected correlation functions, we want random catalogues both in the angular and the radial directions. To obtain randoms in the angular direction is not a difficult task if we assume that our data has a homogeneous distribution in RA and Dec. This can be done in this analysis, since we are cutting at an  $i_{AB}$  magnitude much lower than the limiting magnitudes of the reference catalogue surveys. If that was not the case, we should develop more advanced techniques, such as the ones described in Johnston et al. (2021b), where they develop randoms in the angular direction using Self Organising Maps (SOMs). However, in this paper, the

challenging task comes from developing a set of random catalogues in the radial direction. Previous attempts to do this, such as Cole (2011); Farrow et al. (2015); Johnston et al. (2021a), have applied an algorithm that estimates the radial distribution of the randoms by computing a maximum volume for each galaxy, centred on its current position, around which random points can be distributed. This method is designed to fit the luminosity and overdensity functions as a function of redshift for magnitude-limited samples.

Here, we choose to develop a new technique that relies on the MICE simulation (see Section 2.5). It consists of comparing the GC and IA signals for two different sets of random catalogues. In the first case, the radial distribution of the random catalogue is generated by sampling over the radial distribution of the full octant of MICE. This corresponds to the average distribution of matter without the effect of local clustering, as a result of the large size of the MICE area. This way, we obtain a representation of a random catalogue that does not carry a GC signal. In the second case, the radial distribution of the random catalogue is obtained by smoothing the radial distribution of the triplets of MICE PAUS-like patches (see Section 2.5) with a tophat filter of a given number of Mpc. This case is the one we can reproduce when measuring the observables with the PAUS data, since the first case is only accessible with the MICE simulation.

Once the two sets of random catalogues are defined, the GC and the IA signals are measured using both of them and the difference between the signals is analysed. An indication that both sets of random catalogues are similar is that the signals are consistent between one another. We test different levels of radial smoothing for the second case, going from a smoothing of 20 Mpc until 420 Mpc (which corresponds to the radial distance at redshift 0.1, that is, the minimum redshift we consider when measuring our correlation functions), finding the best match with a smoothing of 420 Mpc.

Fig. C1 shows the comparison of the normalised radial distribution of three cases: the combination of three randomly selected PAUS-like patches in MICE, the randoms generated when smoothing these three PAUS-like patches with a tophat filter of 420Mpc and the randoms generated from sampling over the MICE full octant. Note how similar the radial distributions are for the two random generation approaches, indicating that a smoothing of 420Mpc yields random catalogues analogous to those when sampling the MICE full octant radial distribution.

The comparison of the projected GC and IA signals for the different versions of randoms is depicted in Fig. C2. On the one hand, the top plots of the figure show the comparison of the mean  $w_{gg}$  (left) and  $w_{gp}$  (right) signals, obtained from the combination of the 60 triplets of MICE PAUS-like patches. On the other hand, the bottom plots show the difference of the signals divided by the error, which has been computed as the square root of the diagonal of the ensemble covariance of the 60 triplets (see Appendix E for more details about the ensemble covariance). It can be seen that the GC and IA signals obtained for both random catalogues are consistent with a difference below  $1\sigma$ . Two important remarks can be extracted from this figure. First, the GC signal is more affected than the IA signal when using different random catalogues. This is expected, since the estimator of  $\xi_{gp}$  (eq. 15) correlates shapes with positions, while the estimator of  $\xi_{gg}$  (eq. 14) correlates positions with positions, which is more sensitive to the random catalogue used. Second, although the signals are consistent, the case of the smoothed randoms with a tophat filter yields slightly less signal than the randoms from the MICE full octant. The reason for this is that the smoothed randoms may still carry some clustering, which reduces the total signal from GC and IA. However, we do not expect this to affect our constraints, as shown in Fig. C3.

The importance of constructing suitable random catalogues comes

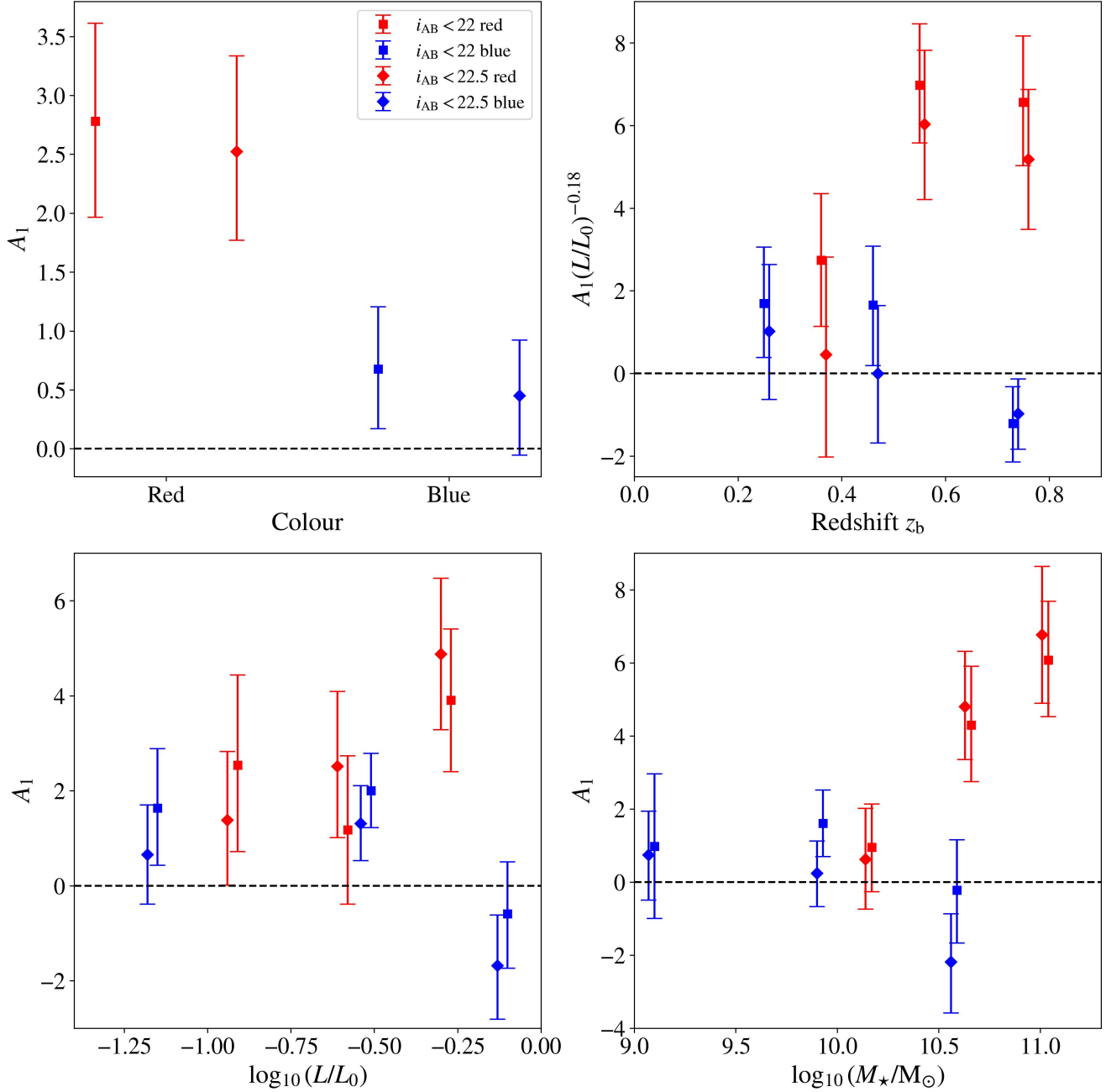


**Figure A1.** Comparison of the  $A_1$  values for the brighter (W1+G09+W3 fields with  $i_{AB} < 22$ , squares) and fainter (W1+W3 fields with  $i_{AB} < 22.5$ , diamonds) samples. The four splits analysed in this work are depicted: galaxy colour (top left), galaxy colour and redshift (top right), galaxy colour and luminosity (bottom left), and galaxy colour and stellar mass (bottom right).

**Table B1.** Number of galaxies classified as red and blue in this work in combination with the classification obtained from different colour splits: GAMA+SDSS (J2019, left table), KiDS-1000 (G2025, centre table) and the previous PAUS IA analysis (J2021, right table).

	Red J2019	Blue J2019		Red G2025	Blue G2025		Red J2021	Blue J2021
Red (this work)	106765	15127	Red (this work)	104913	16979	Red (this work)	96689	358
Blue (this work)	106251	366194	Blue (this work)	87261	385184	Blue (this work)	244626	223395

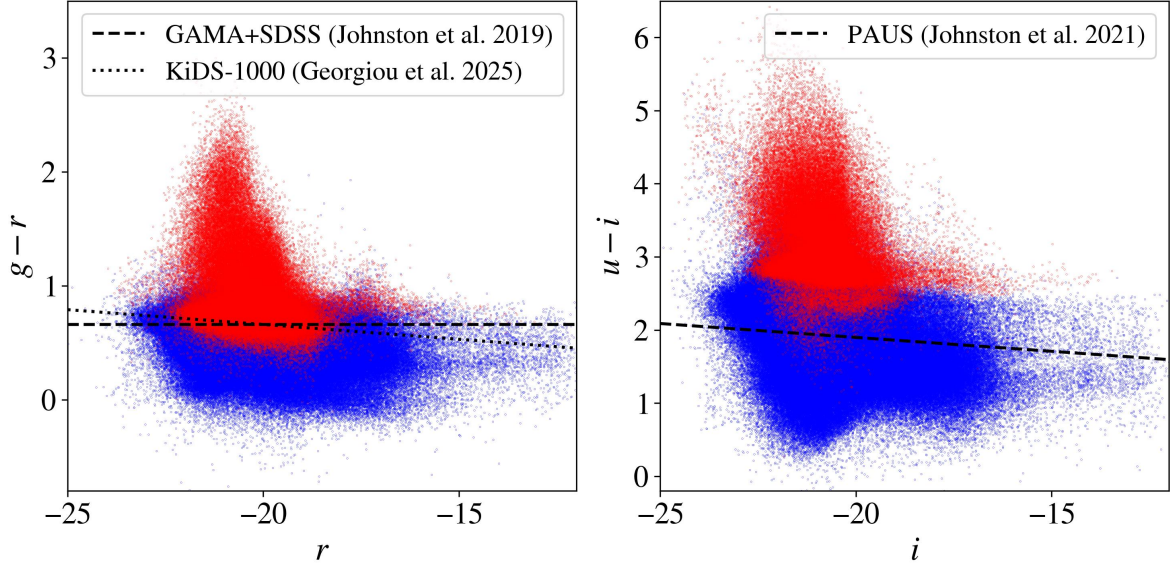


**Figure B1.**  $g - r$  vs.  $r$  (left) and  $u - i$  vs.  $i$  (right) colour-magnitude diagrams showing the red and blue objects obtained from the  $NUVrK$  colour split and the  $T_{BPZ}$  parameter (Section 2.4). The splits performed by GAMA+SDSS (Johnston et al. 2019, dashed line) and KiDS-1000 (Georgiou et al. 2025, dotted line) are depicted on the left plot, while the split performed by the previous PAUS IA analysis (Johnston et al. 2021a, dashed line) is depicted on the right plot.

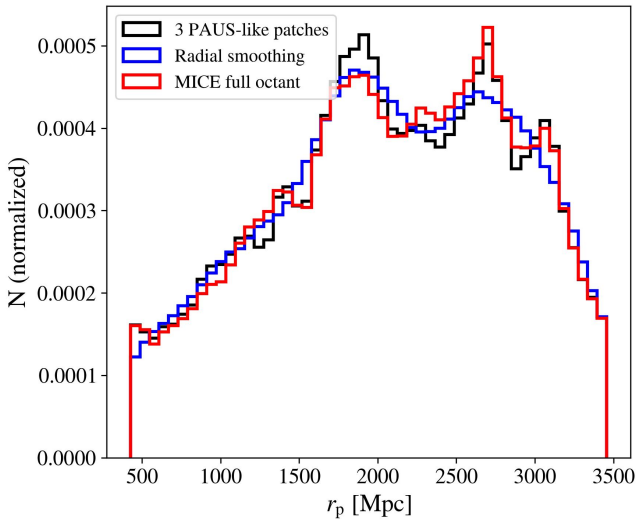


**Figure C1.** Normalised radial distribution of 3 PAUS-like patches in MICE (black), the random catalogues following the radial distribution of the 3 patches with a smoothing of 420 Mpc (blue) and the radial distribution of the full octant of MICE (red).

from the fact that we want to recover the true galaxy bias parameters, since they are fundamental in order to obtain the true IA parameters (see eq. 24 and eq. 34). Following with the discussion on the difference between the GC and IA signals, in Fig. C3 we show the constraints on the galaxy bias and the IA parameters for different sets of random catalogues. Blue contours show the case when using the randoms sampled from the MICE full octant distribution, while red contours show the case for the randoms obtained when smoothing the radial distribution with a tophat filter. The recovered parameters are consistent with each other, specially for the IA amplitude,  $A_1$ .

The SVD introduced in Section 4.6 has also been applied to this case, as well as in Appendix D and E.

#### APPENDIX D: COMPARISON OF THE PHOTO-Z AND SPEC-Z SIGNALS IN MICE

In this section, we compare the correlation functions in MICE when using photo- $z$ s or spec- $z$ s and test if the constrained GC and IA parameters are consistent for both cases.

It is expected that both the GC and the IA signals are smeared out along the radial direction when using photo- $z$ s instead of spec- $z$ s. This is explained by the fact that the positions of the objects are quantified with a lower precision when using photo- $z$ , and so the correlation between the objects decreases. One way to correct for that is to increase the LOS integration in eq. 18, in order to recover the pairs of correlated objects that have been spread over this radial direction. However, it is important not to define an excessively wide radial range, since this might turn into an increase of the noise due to the inclusion of uncorrelated pairs of objects.

We define two radial binnings, one for the spectroscopic and one for the photometric case. On the one hand, we take the spectroscopic radial binning from previous works, such as Georgiou et al. (2019) and Johnston et al. (2019), where they define it in the range  $-60 h^{-1}$  Mpc to  $60 h^{-1}$  Mpc in steps of  $4 h^{-1}$  Mpc. On the other hand, we define the photometric radial binning as in eq. 19, following Johnston et al. (2021a). In order to test if the spectroscopic and photometric radial binnings recover the same signal, we measure and compare the GC and the IA signals in the MICE simulation for both options, following a similar procedure as in previous Section C.

The top plots of Fig. D1 show the comparison of the GC (left) and IA (right) signals obtained when using spec- $z$ s and photo- $z$ s in the MICE simulation. In turn, the bottom plots of the figure show the difference between the signals divided by the error from the ensemble covariance (bottom). On the one hand, for the GC signal, the difference that results between both redshift estimates is of  $\sim 1\sigma$  at small scales, while it approaches  $\sim 0.4\sigma$  at larger scales. Note

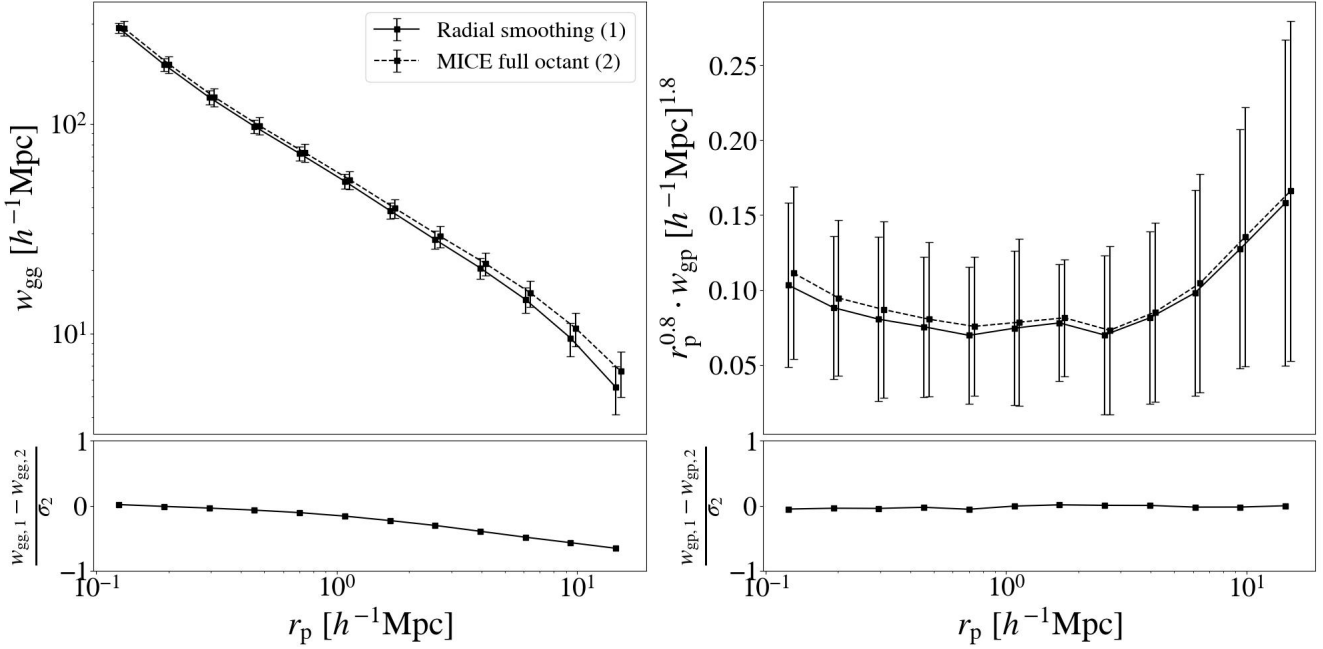


**Figure C2.** Comparison of the GC (left) and IA (right) measurements in MICE with the two versions of random catalogues. The measurements are consistent for both types of randoms, with a difference of less than 1  $\sigma$  in the GC case and negligible for IA, as seen in the bottom panel, which shows the difference between the measurements divided by the error in the full octant case.

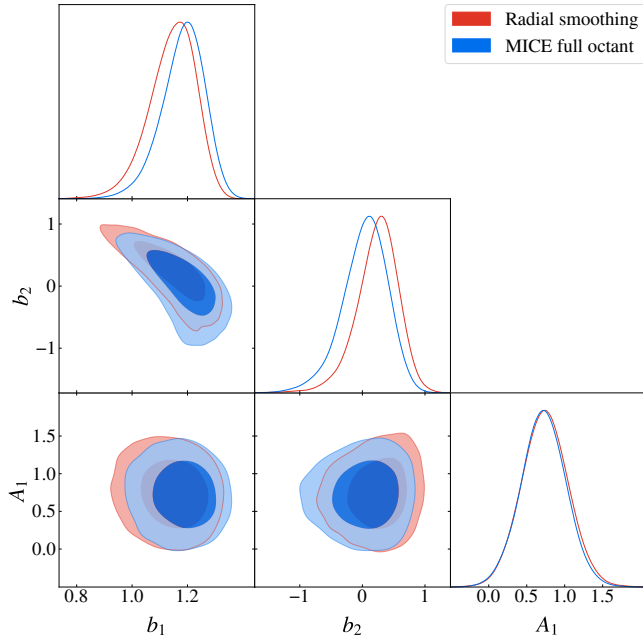


**Figure C3.** Galaxy bias and IA parameters contour plots obtained from fitting the GC and the IA signals in MICE, using the smoothed version of the randoms (red) and the randoms from the MICE full octant (blue).

how the signal measured using spec- $z$ s is slightly larger, as expected because of the smearing out caused by photo- $z$ . However, both results can be considered consistent. On the other hand, for the case of IA, the difference in terms of  $\sigma$  is almost negligible. This seems to indicate, at least in the MICE simulation, that IA are less affected than GC when using less precise redshift estimates.

Fig. D2 shows the GC bias and IA parameters obtained when fitting both the spectroscopic and the photometric cases. Note that the constraining power in the case of employing spec- $z$ s is higher, given that the errors associated to spectroscopic correlation functions are lower. Still, the recovered values are consistent. This consistency test also serves as an indication that the pipeline we designed to model photometric correlation functions is correct.

Since the measurements in the data are also split in redshift bins, we repeated the tests in Fig. D1 and Fig. D2, but dividing the redshift space in three bins. Even though we do not explicitly show the results for conciseness, the recovered galaxy bias and IA parameters agree for the three redshift ranges defined. However, we note again that the constraints between the spectroscopic and the photometric scenarios are different in terms of area, with higher redshift bins leading to broader constraints in the case of photo- $z$ s, due to the decrease of photo- $z$  precision with redshift.

## APPENDIX E: ERROR ESTIMATION

As discussed in Section 3, we estimate the errors for our correlation functions using the JK method (eq. 20). However, considering that the number of JK regions is not very large, due to the limited area in PAUS, we also need to validate our errors with the MICE simulation. In order to do that, we compare the errors derived from the JK method with the errors from the ensemble covariance of the MICE simulation (eq. E1), which are a representation of the true errors of the full octant:

$$\text{Cov}_{ab,i,j}^{\text{ens}} = \sum_{k=1}^N \frac{(w_{ab,k,i} - \bar{w}_{ab,i})(w_{ab,k,j} - \bar{w}_{ab,j})}{N}, \quad (\text{E1})$$

where  $k$  corresponds to each combination of 3 PAUS-like patches,  $i$  and  $j$  denote the  $r_p$  projected position of the data vector,  $N$  is the

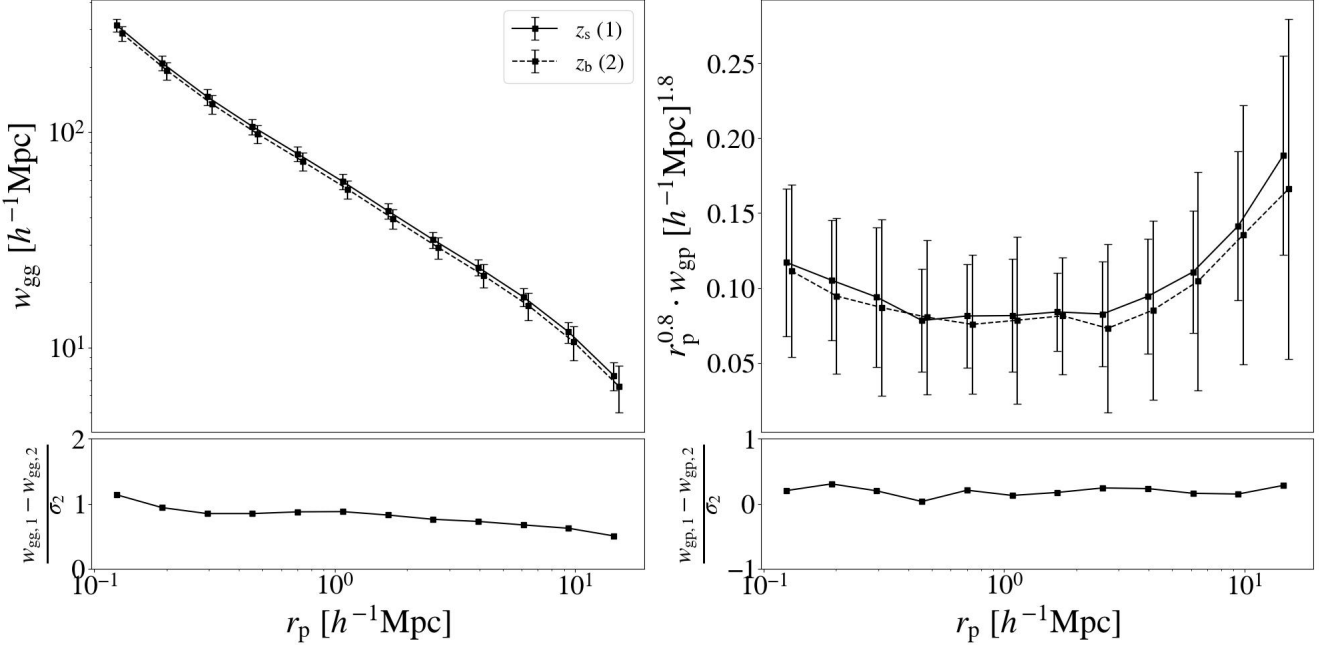


**Figure D1.** Comparison of the GC (left) and IA (right) measurements in MICE for different estimates of the radial positions, spec- $z_s$  and photo- $z_s$ . Both estimates have consistent measurements, with a maximum difference of less than  $1\sigma$  at small projected separations in the GC case and negligible for IA, as seen in the bottom panel, which shows the difference between the measurements divided by the error in the photo- $z$  case.

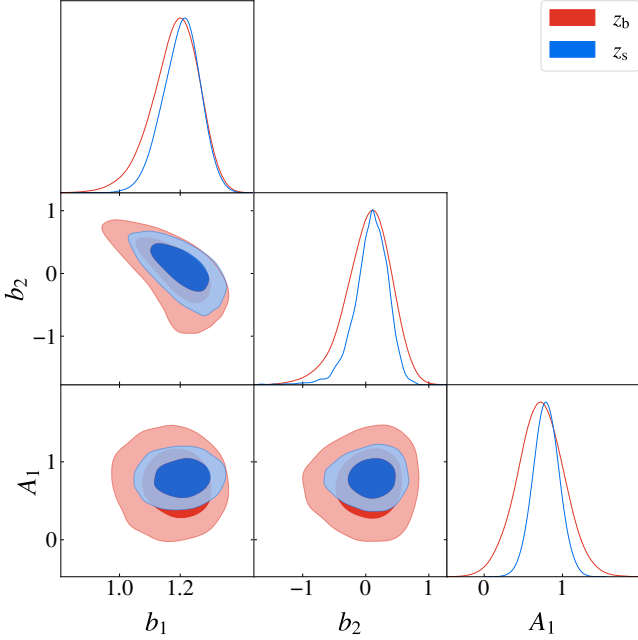


**Figure D2.** Galaxy bias and IA parameters contour plots obtained from fitting the GC and the IA signals in MICE, using photo- $z_s$  (red) and spec- $z_s$  (blue).

number of combinations and  $\bar{w}_{ab,i}$  is the mean of the correlation function at the position  $i$ . We note that we compute the joint covariance of  $w_{gg}$  and  $w_{gp}$ , so that  $w_{ab,k,i}$  and  $\bar{w}_{ab,i}$  are the concatenation of  $w_{gg}$  and  $w_{gp}$ . Given that each of the 3 PAUS-like patches have an associated JK covariance, we compare the ensemble covariance with the mean of the JK covariances of the 60 3 PAUS-like patches, which we name as ‘‘mean JK covariance’’.

Fig. E1 shows a comparison between the errors obtained from the ensemble and the mean JK covariances, for the  $w_{gg}$  (left) and the  $w_{gp}$  (right) estimators. This is shown at 4 different separations in terms of  $r_p$ , so as to capture the evolution as a function of the separation between galaxies. The histograms in the plots show the distribution of the individual JK covariances (in terms of the square root of the diagonal of the covariance) for the 60 triplets of the MICE PAUS-like patches. The vertical red and black lines show the errors of the ensemble and the mean JK covariances, respectively. For the case of  $w_{gg}$ , at small scales ( $r_p < 1 h^{-1} \text{Mpc}$ ), the mean JK errors are overestimated with respect to the ensemble covariance. However, both errors agree at intermediate scales and the mean JK errors are underestimated at large scales. In general, the distribution of the individual JK errors for  $w_{gg}$  is located at values lower than the ensemble covariance, indicating that the mean JK error may be driven by large individual JK errors at small scales. For the case of  $w_{gp}$ , the mean JK errors are usually larger than the ensemble covariance, although with different variations. However, in all the  $w_{gg}$  and  $w_{gp}$  cases, the error estimates agree, since the ensemble covariance is well inside the range of the individual JK errors.

The fact that both error estimates agree well can also be seen in Fig. E2. The top panel shows the errors of the ensemble covariance and the mean JK error as a function of the  $r_p$  separation, for  $w_{gg}$  (left) and  $w_{gp}$  (right). The error bars depicted for the mean JK error correspond to the standard deviation of the individual JK errors with respect to the mean. The bottom panel shows the difference between the errors of the ensemble covariance and the mean JK error, normalised by the standard deviation of the mean JK error. From this figure, the agreement between both error estimates is verified for all  $r_p$  separations, with a maximum of a  $\sim 1\sigma$  difference for the case of the  $w_{gp}$  estimator and below  $\sim 0.5\sigma$  for  $w_{gg}$ . As in Appendix D, we studied the comparison between the ensemble and the mean JK covariances as a function of redshift. In all the cases, the errors of the

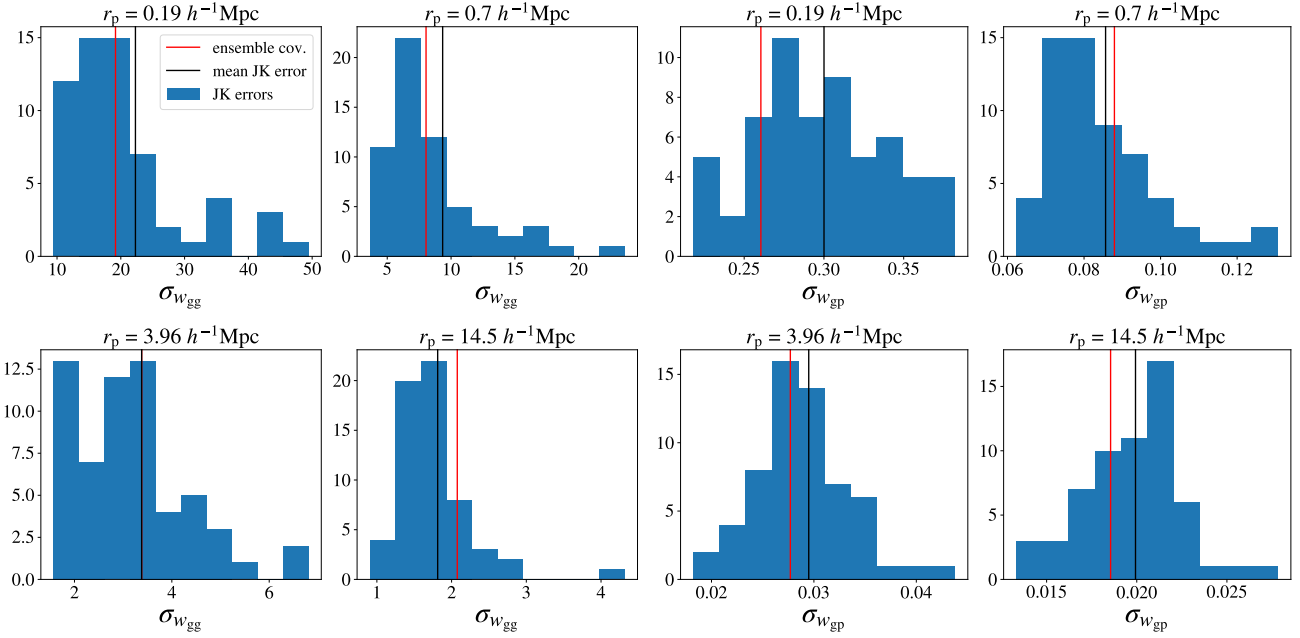


**Figure E1.** Distribution of the individual JK errors of the 60 triplets of MICE PAUS-like patches at different separations, for  $w_{\text{gg}}$  (4 left plots) and  $w_{\text{gp}}$  (4 right plots). Red and black vertical lines show the errors of the ensemble covariance and the mean JK error at that separation, respectively.

mean JK and the ensemble covariances present a similar behaviour as Fig. E2, with differences up to  $\sim 1\sigma$ .

So far, we have shown how the diagonal terms of the mean JK and the ensemble covariances relate to each other. Nevertheless, since the modelling of the PAUS data uses the whole covariance matrix, we are also interested in how the off-diagonal terms affect the modelling of our observables. Besides, even though there is a maximum of  $\sim 1\sigma$  differences between both error estimates, we are interested in how these may affect our constraints. In that sense, Fig. E3 shows the galaxy bias and the IA constraints obtained when fitting the mean  $w_{\text{gg}} \cup w_{\text{gp}}$  data vector obtained from the triplets of MICE PAUS-like patches, using the mean JK and the ensemble covariances, where a SVD is performed to both covariance estimates. In the case of the mean JK covariance, it is computed after individually performing the SVD to each 3 PAUS-like patch JK covariance. The galaxy bias constraints agree quite well for the  $b_1$  parameter, while there are some discrepancies in  $b_2$ , although the constraints still overlap and this bias only represents a second-order effect on the GC. As for the IA parameter, the agreement between both covariance estimates is total. It is important to note that, in the PAUS data, we only have one realisation of the results, while in the MICE simulation we have 60 triplets of PAUS-like patches, from which we compute the mean JK covariance. Thus, even though the mean JK and the ensemble covariances yield very similar constraints, it might happen that the PAUS data covariance differs more from the ensemble covariance, as is the case for some of the individual combinations seen in the histograms of Fig. E1. Nevertheless, in that same figure, the majority of the individual JK errors agree quite well with the mean of the covariances, so the probability of significantly different errors in the data is expected to be low.

## APPENDIX F: CONTAMINANTS CONTRIBUTION TO WGP

Fig. F1 shows how the contaminants affect the  $w_{\text{gp}}$  measurements, indicated as the ratio of each contaminant over the total  $w_{\text{gp}}$  signal. We consider the different terms that affect the position-shape correlation function, which are, as indicated in eq. 42, gI, gG, mI and mG. Note that these terms do not need to have the same sign, which makes it possible for the ratio of one of the terms to be negative or positive and to be greater or less than 1. In fact, in general, the galaxy-shear term has opposite sign from the galaxy-intrinsic term, which leads to a decrease in the total value of  $w_{\text{gp}}$ . This is a strong reason on why it is important to include contaminants in our modelling. The contaminants on  $w_{\text{gg}}$  are also included in the fitting of the data but are not shown here, since they contribute to the position-position correlation function at a sub-percent level. For both red and blue galaxies, the contaminant terms depending on magnification, mI (dotted line) and mG (dash-dotted line), are negligible, given that  $\alpha(i_{AB})$  for this case is close to 1, as seen in Table 2. The galaxy-intrinsic term, gI (solid line), is the most important one for both galaxy colours, as it is expected for measurements that are designed to focus on the IA effect, since these consider objects close in redshift. The galaxy-shear term, gG (dashed line), is the main contaminant to the IA measurements. In the case of red objects, the ratio of gG over  $w_{\text{gp}}$  is -0.2 (while the ratio of gI is 1.2), which accounts for a  $\sim 10\%$  of the signal. In the case of blue galaxies, the contribution from the galaxy-shear term is even higher, arriving to a  $\sim 35\%$ , since the IA signal is very low. Note that the percentages we described correspond to the ratio taken over all the  $r_p$  range. Nevertheless, the contribution from the gI and gG terms vary over that range, as seen in Fig. F1. The contribution of the contaminants to the other configurations studied in this paper was also assessed, although not shown here for conciseness. As in the separation by colour, the terms including the magnification contributions are almost negligible, while the main contaminant is the gG term which ranges between  $\sim 5\% - 20\%$  for red objects and

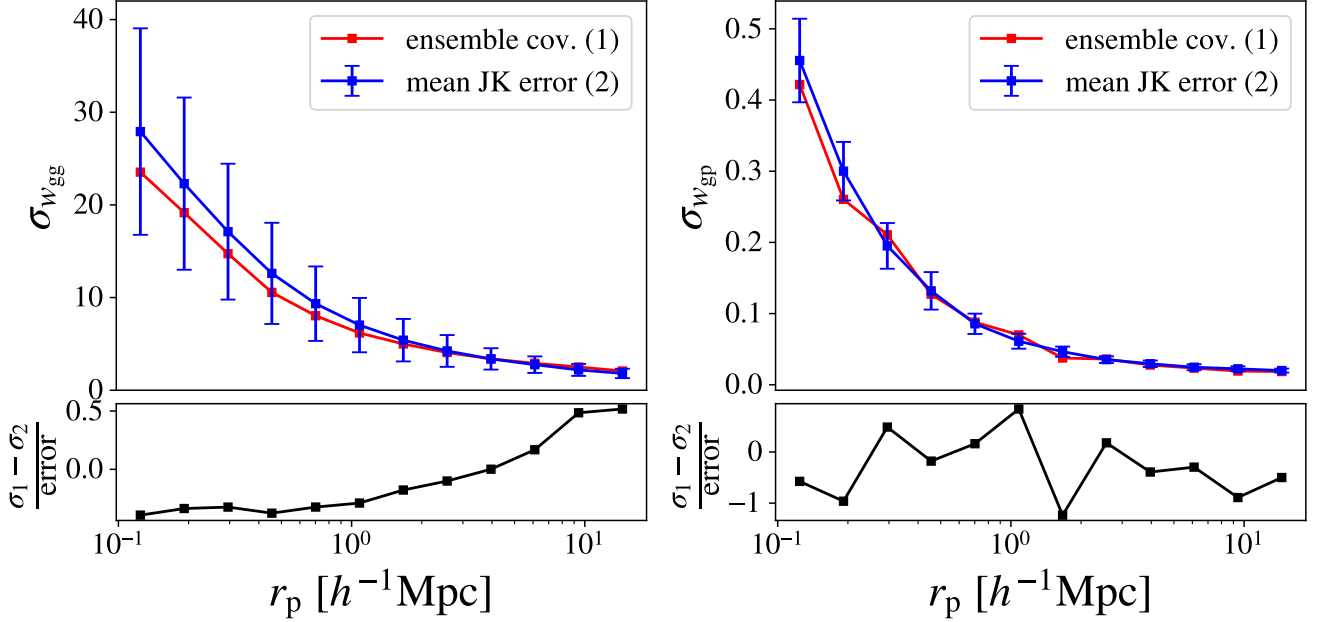


**Figure E2.** (Top): Errors of the ensemble covariance (red) and the mean JK error (blue) as a function of the  $r_p$  separation. The error bars of the mean JK error correspond to the standard deviation of the individual JK errors with respect to the mean. (Bottom): Difference between the errors of the ensemble covariance and the mean JK error, normalised by the standard deviation of the mean JK error.

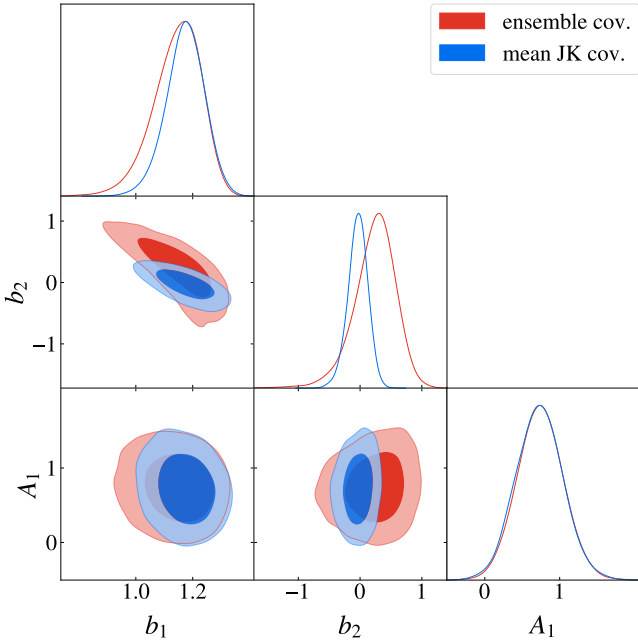


**Figure E3.** Galaxy bias and IA parameters contours obtained when fitting the mean  $w_{\text{gg}} \cup w_{\text{gp}}$  data vector with the ensemble covariance (red) and the mean JK covariance (blue). The galaxy bias and IA parameters obtained from both methods are very similar, specially for  $A_1$ .

$\sim 15\% - 65\%$  for blue objects, where the larger contribution comes again from the fact that the IA signal for blue galaxies is low.

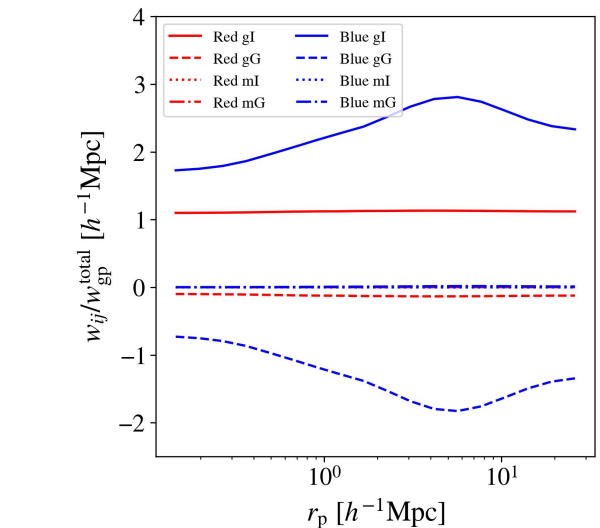


**Figure F1.** Fraction of contamination to  $w_{\text{gp}}$  for red and blue galaxies for the different terms that contribute to eq. 42: gI (solid line), gG (dashed line), mI (dotted line) and mG (dash-dotted line).

#### APPENDIX G: SCALE CUT ANALYSIS

Here, we study the dependence on the scale cuts when fitting the  $w_{\text{gg}} \cup w_{\text{gp}}$  data vector with the non-linear galaxy bias, for GC, and the NLA model, for IA. As indicated in Section 4.6, we set  $r_{p,\text{min}} = 2.0 h^{-1}\text{Mpc}$  for both  $w_{\text{gg}}$  and  $w_{\text{gp}}$ . However, in this appendix, we explore the scale cuts further by setting different values of  $r_{p,\text{min}}$  in the case of  $w_{\text{gp}}$ , while fixing  $r_{p,\text{min}} = 2.0 h^{-1}\text{Mpc}$  for  $w_{\text{gg}}$ . The justification of this approach is that the non-linear galaxy bias breaks down below  $r_{p,\text{min}} = 2.0 h^{-1}\text{Mpc}$ . Nevertheless, in the case of the NLA model, previous studies set  $r_{p,\text{min}} = 6.0 h^{-1}\text{Mpc}$  based on

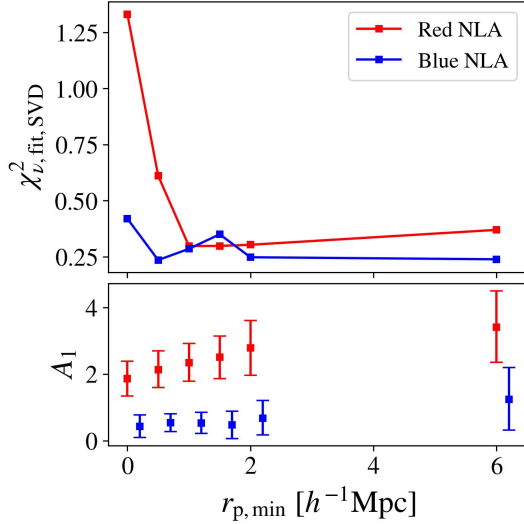


**Figure G1.**  $\chi^2_{v,\text{fit},\text{SVD}}$  (top) and  $A_1$  (bottom) as a function of the minimum  $r_p$  separation considered in the modelling of  $w_{\text{gp}}$  for red and blue galaxies.

observations, while Paviot et al. (in prep.) shows that this mainly depends on the fact that linear galaxy bias is used. Given the high number density of PAUS, which allows correlations to be measured down to smaller scales than with other spectroscopic surveys, we want to explore the range of validity of the NLA model by exploring different scale cuts. The scale cuts we test for  $w_{\text{gp}}$  range from the common  $r_{p,\text{min}} = 6.0 h^{-1} \text{Mpc}$  down to the uncommon  $r_{p,\text{min}} = 0.0 h^{-1} \text{Mpc}$ , which means that there is no scale cut. We analyse the variations in  $\chi^2_{v,\text{fit},\text{SVD}}$  (eq. 51), together with the change in the  $A_1$  constraints, as a function of  $r_{p,\text{min}}$ .

Fig. G1 shows the dependence on the scale cuts when splitting the PAUS samples in red and blue galaxies. Both types of galaxies are evaluated at the same  $r_{p,\text{min}}$  values, but the  $A_1$  amplitudes for blue galaxies are plotted at slightly larger values, to avoid overlapping. We highlight that we focus on the evolution of the  $\chi^2_{v,\text{fit},\text{SVD}}$  value, rather than on its absolute value, given the remark made at the end of Section 5.3 about the values below and above 1 in the  $\chi^2_{v,\text{fit},\text{SVD}}$ . For the case of red objects, the  $\chi^2_{v,\text{fit},\text{SVD}}$  starts increasing at  $r_{p,\text{min}} < 1.0 h^{-1} \text{Mpc}$ , from a stable value of  $\chi^2_{v,\text{fit},\text{SVD}} \sim 0.35$  up to  $\sim 1.4$ . The values of  $A_1$  continuously decrease as we include smaller  $r_{p,\text{min}}$  values, while its error bars are also reduced, given the larger number of available data points. In the case of blue objects, the  $\chi^2_{v,\text{fit},\text{SVD}}$  is quite stable, but this is most likely due to the lack of signal for these types of galaxies.

We have also analysed the evolution of  $\chi^2_{v,\text{fit},\text{SVD}}$  for the other cases included in this paper, although not shown here for conciseness. In general, we find that it is not possible to reach values of  $r_{p,\text{min}} < 1.0 h^{-1} \text{Mpc}$  without the  $\chi^2_{v,\text{fit},\text{SVD}}$  increasing. Nevertheless, in some cases, the fact of reducing  $r_{p,\text{min}}$  allows some points with high noise to enter in the  $\chi^2_{v,\text{fit},\text{SVD}}$ , increasing its value for that particular  $r_{p,\text{min}}$  and then reducing it when further decreasing  $r_{p,\text{min}}$ , since a point with less noise enters the computation. Thus, it is not straightforward to validate the use of low  $r_{p,\text{min}}$  values with this approach.